NAG3-2359

Analysis of Factors Affecting the Performance of RLV Thrust Cell Liners

Daniel T. Butler, Jr. and Marek-Jerzy Pindera
University of Virginia
Charlottesville, Virginia 22904

Abstract

The reusable launch vehicle (RLV) thrust cell liner, or thrust chamber, is a critical component of the Space Shuttle Main Engine (SSME). It is designed to operate in some of the most severe conditions seen in engineering practice. This requirement, in conjunction with experimentally observed "dog-house" failure modes characterized by bulging and thinning of the cooling channel wall, provides the motivation to study the factors that influence RLV thrust cell liner performance. Factors or parameters believed to be directly related to the observed characteristic deformation modes leading to failure under in-service loading conditions are identified, and subsequently investigated using the cylindrical version of the higher-order theory for functionally graded materials in conjunction with the Robinson's unified viscoplasticity theory and the power-law creep model for modeling the response of the liner's constituents. Configurations are analyzed in which specific modifications in cooling channel wall thickness or constituent materials are made to determine the influence of these parameters on the deformations resulting in the observed failure modes in the outer walls of the cooling channel. The application of thermal barrier coatings and functional grading are also investigated within this context.

Comparison of the higher-order theory results based on the Robinson and power-law creep model predictions has demonstrated that, using the available material parameters, the power-law creep model predicts more precisely the experimentally observed deformation leading to the "dog-house" failure mode for multiple short cycles, while also providing much improved computational efficiency. However, for a single long cycle, both models predict virtually identical deformations. Increasing the power-law creep model coefficients produces appreciable deformations after just one long cycle that would normally be obtained after multiple cycles, thereby enhancing the efficiency of the analysis. This provides a basis for the development of an accelerated modeling procedure to further characterize "dog-house" deformation modes in RLV thrust cell liners. Additionally, the results presented herein have demonstrated that the mechanism responsible for deformation leading to "dog-house" failure modes is driven by pressure, creep/relaxation and geometric effects. Since creep and relaxation are strong functions of temperature, the mechanism is temperature driven as well, and thus thermal barrier coatings have the potential to mitigate this failure mode.

Analyses of RLV thrust cell liners employing thermal barrier coatings have shown that their influence on temperature and deformation fields was dependent on coating thickness. However, grading of metallic substrate and coating materials has not demonstrated improvement in terms of overall thrust cell liner performance. This suggests that the cost of grading the considered constituents likely outweighs the benefits. Furthermore, grading is potentially detrimental due to likely roughening of the thrust cell liner wall in the combustion chamber as a result of local deformations around relatively coarse inclusions. The homogenized approach to analyzing the graded coatings has been shown to be incapable of capturing these localized effects.

1 Introduction

The reusable launch vehicle (RLV) thrust cell liner, or thrust chamber, is a critical component of the Space Shuttle Main Engine (SSME). This liner is just one component of the world's most sophisticated reusable rocket engine and is designed to operate in some of the most severe conditions seen in engineering practice. The space shuttle's three main engines can be seen relative to the entire launch vehicle at the center of Figure 1.1 and in more detail in Figure 1.2. Each engine is 14 feet in length and 7 ½ feet wide, weighs 7480 lbs and is capable of producing 512,950 lbs of thrust or the equivalent to more than 12,000,000 horsepower. The schematic shown in Figure 1.3 highlights the thrust chamber inside the SSME. An actual small-scale version of a thrust liner is shown in Figure 1.4 completing the hierarchy from launch vehicle to thrust liner.

Since the inception of the SSME concept in the 1970s, the severe temperatures and pressures exerted on the thrust cell liner nozzles have shortened their lives, plagued overall engine performance and efficiency, and also contributed to high maintenance costs. Improved performance of RLV thrust liners has long been an aim of scientists and engineers seeking to enhance reusability of the SSME and other advanced aircraft engines to as many as several hundred thermal cycles. Achieving such a goal could significantly reduce maintenance costs and permit more frequent missions. As in most structures, two factors are known to have a direct impact on the performance and/or durability of thrust chambers: material selection and geometry.

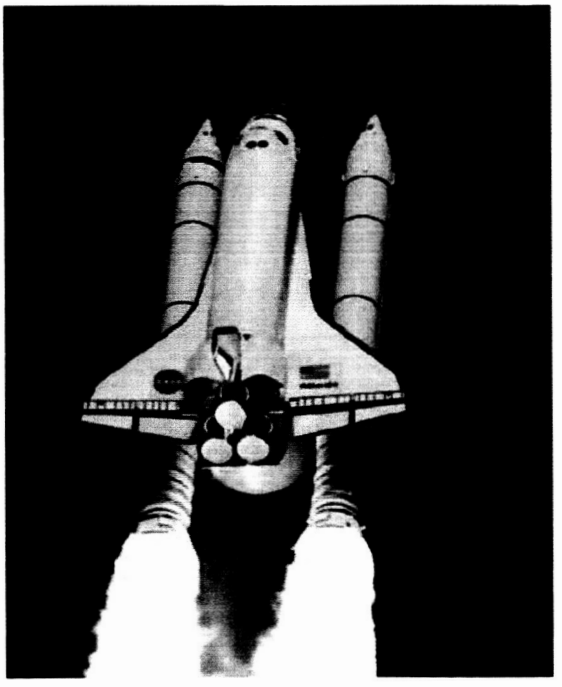

Figure 1.1. Photograph of the space shuttle during liftoff
(source: https://rockettest.ssc.nasa.gov/ssc_ptd/projects_ssme.htm).

Due to the severity of in-service loading conditions (to be discussed in detail in Section 2), materials used in fabrication of thrust cell liners must exhibit high thermal conductivity, high strength and creep resistance. Few materials naturally possess all these characteristics. A number of copper-based alloys have, however, been developed specifically for use in high-performance rocket nozzles. The use of

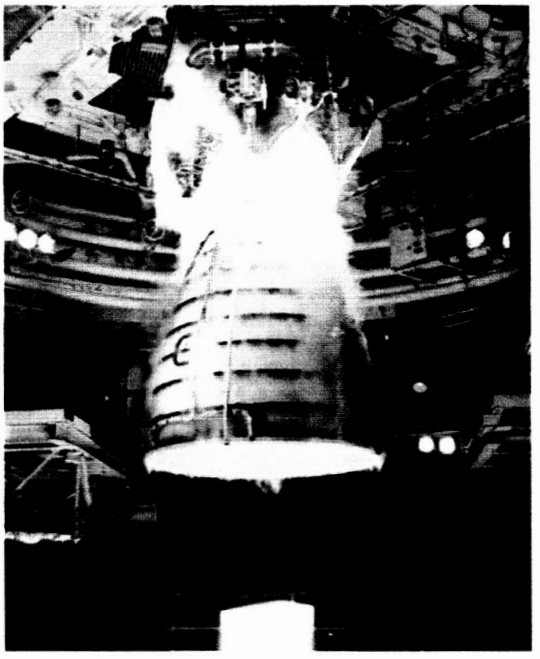

Figure 1.2. Photograph of the space shuttle main engine during a firing test (source: http://grin.hq.nasa.gov/IMAGES/SMALL/GPN-2000-000055.jpg).

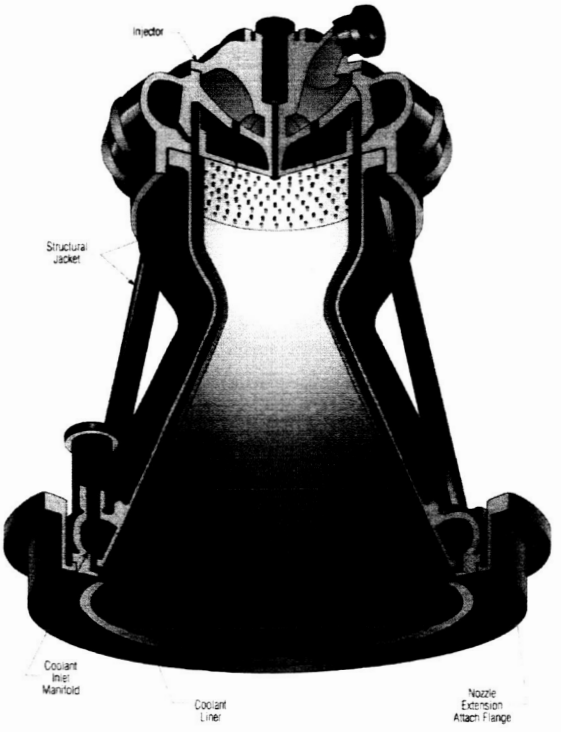

Figure 1.3. A typical, regeneratively cooled combustion chamber (source: http://www.engineeringatboeing.com/articles/heart.jsp).

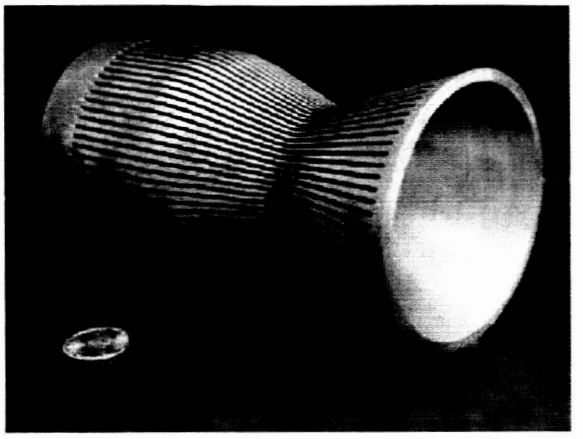

Figure 1.4. A subscale thrust cell liner
(source: http://technology.grc.nasa.gov/tops/TOP3-00139LowRes.pdf).

copper is advantageous due its high conductivity, but its high temperature characteristics, particularly lack of creep resistance, limit its application in pure form. Through alloying, however, the high-temperature performance of copper is improved, resulting in increased strength and creep resistance.

Amzirc, NARloy-Z and more recently GRCop-84 are copper-based alloys which have been employed in experimental thrust cell liner fabrication. Amzirc is the tradename for a zirconium-copper alloy, containing 0.15 percent zirconium, developed by American Metal Climax, Inc. Likewise, NARloy-Z is the tradename of a silver-zirconium-copper alloy developed by Rockwell International Inc. NARloy-Z contains 3 percent silver and 0.5 percent zirconium. GRCop-84 is a copper-chromium-niobium alloy, developed by the NASA Glenn Research Center in collaboration with the Case Western Reserve University, which exhibits enhanced creep resistance, higher operating temperatures and lower thermal expansion. These materials, together with oxygen-free high conductivity copper (OFHC), have played a critical role in the development and mission insertion of RLV thrust cell liners.

Similarly, geometry plays an important role in thrust chamber design and fabrication. The chamber itself must balance the demands of power and cooling, thus designers are faced with the challenge of achieving optimal performance (which tends to demand higher operating temperatures and lower structural weight) while still providing the necessary cooling in order to maintain the structural integrity of the liner. A variety of coolant channel designs can be used, but the most common approach employs a series of square channels machined into a layer of material plated over a mandrel before a closeout material is electroformed to complete the coolant channel. This will be discussed in the following section which summarizes experimental and numerical investigations of the thrust cell liner response/performance during experiments intended to simulate in-service conditions.

1.1 RLV Thrust Cell Liner Response: A Literature Review

Beginning in the 1970s, NASA commissioned a number of studies to analyze thrust chambers and characterize their constituents in an attempt to further understand thrust cell liner thermal and mechanical behavior under in-service loading conditions and ultimately to make life predictions as well as improve performance. This work began with an investigation of the mechanical and physical properties of Amzirc, NARloy-Z and OFHC copper conducted by Esposito and Zabora (1975). As a continuation of the work to characterize these materials, Armstrong and Brogren (1975) investigated cyclic thermomechanical behavior and fatigue life of thrust chambers composed of each material. A plane-

strain, finite-element analysis was performed using a structural analysis computer code known as BOPACE 2-D (Boeing Plastic Analysis Capability for Engines). The computer program was capable of accounting for elastic, plastic, creep and thermal strains. The representative liner cross-section shown in Figure 1.5 was analyzed over a 3.5 second cyclic history, also included in Figure 1.5, using 281 elements and a relatively coarse mesh in the region where little to no inelastic deformation was expected. The authors concluded that cyclic life strongly depended on the operating conditions and material selection by examining computed thermal profiles as well as by identifying critical regions for low-cycle fatigue based on effective total strains. The relatively coarse mesh employed with the short loading history also illustrated the computational demands associated with realistic thrust cell liner analysis.

In a follow-up investigation, Armstrong and Brogren (1976) considered three-dimensional effects on the thermomechanical behavior and fatigue life of thrust chambers using first the Boeing Engineering Thermal Analyzer (BETA) program to compute steady-state heat flow and then BOPACE 2-D and BOPACE 3-D to perform structural analysis. These authors employed the same material properties and cyclic loading history as those employed in their earlier study. A chief objective of this study was to determine the accuracy of a 2-D analysis, or rather the necessity of a 3-D analysis. By comparing 2-D and 3-D thermal analyses, the investigators demonstrated that the 2-D analysis was capable of accurately predicting thermal response under the prescribed boundary conditions, but not the thermomechanical strains for which 3-D analysis was necessary.

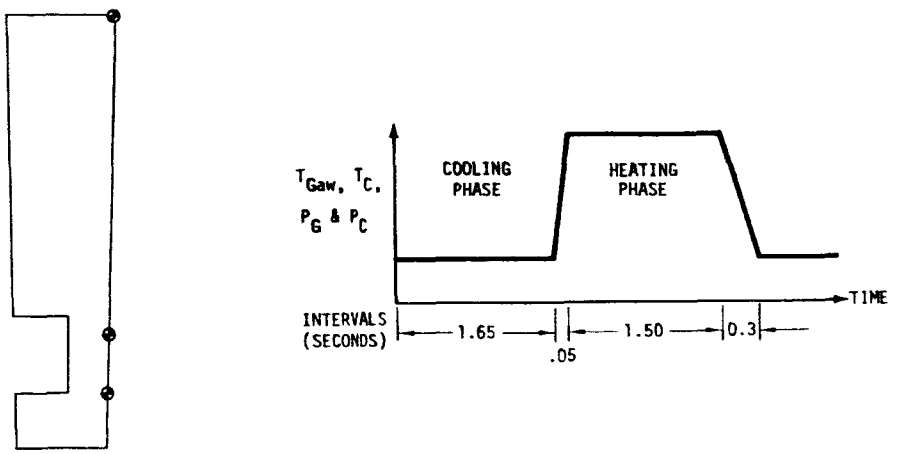

Figure 1.5. Generic cross-section showing thermocouple locations (left) and cyclic temperature and pressure history (right) used in analysis by Armstrong and Brogren (1975) and others.

Quentmeyer (1977) subsequently conducted an experimental investigation of fatigue life of thrust chambers fabricated from OFHC copper, NARloy-Z and Amzirc. Noting a very limited collection of experimental data at the time, Quentmeyer designed the experiments to identify the primary failure mechanism of these thrust chambers under cyclic loading. Each cycle in these tests was 3.5 seconds in duration and similar in magnitude to that employed earlier by Armstrong and Brogren. A number of key results and conclusions were attained through this study. First, Quentmeyer identified a correlation between experimentally determined number of cycles to failure and temperatures predicted through the application of the computer program called Systems Improved Numerical Differencing Analyzer or SINDA. The SINDA program used experimental temperature data collected by thermocouples at the locations shown in Figure 1.5 along with the appropriate boundary conditions to predict an entire cross-

sectional wall temperature profile via a finite-differencing approach. Quentmeyer found that his experimental cycles to failure data correlated equally well with the predicted temperature at the thrust chamber inner radius and the predicted temperature difference across the wall separating the thrust chamber and the coolant channel. At this point, Quentmeyer had analyzed temperature fields only and *had not* attempted to correlate failure data to a mechanical analysis of the deformations in the thrust chambers. Second, experimental results showed that liners fabricated from NARloy-Z and aged Amzirc exhibited the most desirable cyclic life characteristics. Third, Quentmeyer concluded that "every failure was characterized by a *thinning* of the cooling passage wall, *bulging* of the wall toward the thrust chamber centerline, and a severely deformed cooling channel cross-sectional geometry". This type of failure has become known as the "dog-house" failure mode and has been the subject of much investigation over the past 25 years. Figure 1.6 shows the type of failure Quentmeyer so vividly described. Quentmeyer's work also showed the prohibitive expense of conducting experimental studies in order to better understand the factors influencing thrust cell liner deformation, giving rise to the need for accurate and computationally efficient analysis tools.

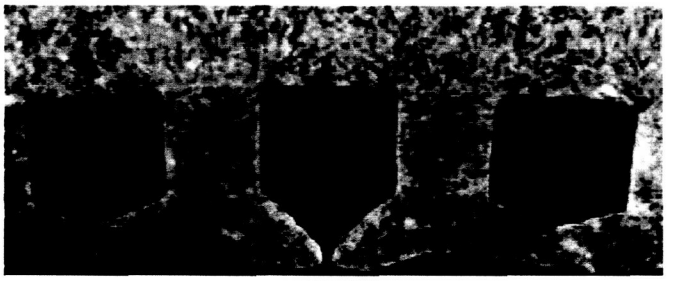

Figure 1.6. Detailed cross-section at the inner radius of the thrust cell liner showing the failure site in the center coolant channel (source: Ellis (1999)).

Motivated by Quentmeyer's experimental data, Armstrong (1979) subsequently employed the BOPACE finite-element computer program in conjunction with a 3.5 second cyclic loading history to analyze the deformations of OFHC and Amzirc thrust chambers. Armstrong believed these "dog-house" type deformations to be "good predications of long-term engine response to the specified load cycle". The most notable result to come from this study, however, was Armstrong's suggestion for future investigations into curved coolant channel designs. Though not explicitly stated, one could infer that Armstrong was the first to recognize the impact that the previously investigated square coolant channels had on stress and deformation fields.

Hannum and Price (1981) also carried out experimental investigations on OFHC copper, NARloy-Z and Amzirc thrust chambers. These authors noted the same cyclic-induced bulging and thinning that Quentmeyer had previously observed. In particular, they categorized the experimentally observed deformation into three modes and considered the effect of each deformation mode on the temperatures at the liner's inner radius as predicted by the computer code SINDA. The types of deformation considered were (1) bulging of the coolant channel, (2) thinning of the coolant channel wall and (3) roughening of the hot-gas-side wall surface which the authors described as having an orange peel appearance. Using the experimentally observed bulging and thinning of the coolant channel wall to construct geometric models as inputs to the computer code, the authors determined that these deformation modes of the coolant channel wall had only a small effect on the temperatures at the thrust cell liner's inner radius. Taken independently, however, bulging of the coolant channel wall was predicted to increase temperatures across the wall, while thinning of the coolant channel was predicted to have the opposite effect. Thus, combining the two deformation modes negated the individual effects of each on

temperature but presumably not stability. Their experimental results, however, also demonstrated that the heat transfer coefficient at the inner radius of the thrust cell liner was increased by 24 percent due to the surface roughening that occurred during cyclic testing. Including the effects of surface roughening in the computer code was shown to increase temperatures in the coolant channel wall, likely promoting deformations. Polishing the thrust chamber wall to achieve a smooth surface reversed the effect of roughening. The authors then predicted that such polishing would extend the life of the thrust chamber due to the reduction in temperatures at this surface. This, however, was not the case as the polished liner failed at approximately the same number of cycles as the unpolished liners. Though the effects of roughening were documented by Hannum and Price, the root causes of this phenomenon were not studied or well understood, again demonstrating the limits of experimental investigations.

Studies by Murphy et al. (1986) and Morgan et al. (1988) further addressed the roughening observed by Hannum and Price. These authors demonstrated that copper alloy thrust cell liners deteriorated when exposed to a cyclic reducing-oxidizing (redox) environment, which is a result of the combustion process. This type of deterioration, which they characterized by roughening and burn-through sites caused by local hot spots in the thrust chamber wall, is often referred to as blanching. In Section 1.2, we discuss a means by which blanching can be avoided.

In an effort to predict the "dog-house" deformation mode identified by Quentmeyer, Arya and Arnold (1991) employed Robinson's inelastic constitutive model, Robinson (1982), to analyze the response of an experimental cylindrical thrust chamber liner composed solely of NARloy-Z using the finite-element method. Unlike previous work, this study employed a unified viscoplasticity theory, which was capable of accounting for time-dependent inelastic and plastic behavior simultaneously, thought to be important for the considered material system. Although their results did not demonstrate simultaneous bulging and thinning of the cooling channel wall, these authors concluded that the "dog-house" effect was caused by the biasing pressure differential across the cooling channel wall, in conjunction with time-dependent inelastic flow, producing an outward bowing of the cooling channel wall. The pressure differential was a result of the relatively low pressure in the combustion chamber with respect to the pressure exerted by the coolant forced through the cooling channel. Additionally, the very coarse grid employed in this study demonstrated the computational expense associated with such an analysis when a computationally demanding constitutive model is employed.

Addressing the suggestion set forth by Armstrong (1979), Jankovsky et al. (1995) employed a viscoplastic analysis of modified thrust chamber geometry in an effort to reduce large strains previously shown to exist in the analysis of square cooling channel designs. This work demonstrated that a curved or tubular coolant channel design could reduce compressive strain, thus reducing total strain and extending life. Though this result offered a potential means by which improved cyclic life of such thrust cell liners could be achieved, engineers throughout the aerospace and propulsion industry have been reluctant to further investigate or adopt and certify such a dramatic overhaul. An alternative approach to achieve extended life of thrust cell liners makes use of existing technology and involves the application of what is known as a thermal barrier coating (TBC). In recent years, a great deal of effort has been concentrated on the development of these coatings.

1.2 Thermal Barrier Coatings (TBCs)

TBCs are commonly used in automotive, aerospace, power generation and other specialty industries. In the aerospace industry in particular, TBCs have drawn considerable interest over the years for their inherent capability to protect critical structural components from severe temperatures. Within the thrust chamber of the SSME these materials permit higher operating temperatures and thus higher efficiencies as well. A photomicrograph of a typical plasma-sprayed ceramic TBC system with bond coat as used in industrial gas turbines, aircraft engines and large diesels engines is shown in Figure 1.7.

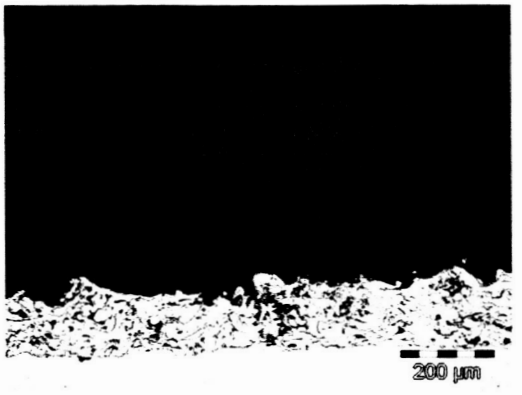

Figure 1.7. Micrograph of a ceramic plasma-sprayed TBC (source: http://www.sulzermetco.com/eprise/SulzerMetco/Sites/News/OTS/ots06f.html).

In a follow-up investigation of fatigue life in uncoated thrust chambers, Quentmeyer et al. (1978) initiated the first study to investigate the effect of ceramic coatings on rocket thrust chamber life. These researchers discovered that the presence of ceramic coatings had a significant effect on mitigating the characteristic failures previously observed in the tests on uncoated thrust cell liners. This work also demonstrated the effectiveness of ceramics as thermal barriers. However, the ceramic coatings were observed to erode throughout the cyclic history. Despite the erosion of the coatings, the authors concluded that "due to the profound reduction in effective strain and the accompanying large potential increase in life that can be achieved by use of ceramic coatings, the further development of reliable coating systems for rocket thrust chamber application appears to be a worthwhile endeavor". Although these authors successfully illustrated the effects of ceramic thermal barrier coatings, their experimental results gave little direction to influence design.

In addition to erosion problems, ceramic plasma-sprayed TBCs have been shown to be susceptible to delamination from substrate and/or bond coat materials and ultimately failure by spallation (Miller and Lowell, 1982). The work of Miller and Lowell suggested that this failure mechanism was a result of severe thermal expansion mismatch between the coating and the substrate material promoting large residual stresses in the coating during the cooldown portion of the thermal cycle. Interfacial roughness between top and bond coat layers was also shown to promote significant peel stresses further contributing to failure mechanism. Despite such problems, Miller (1997) stated in a comprehensive review of TBCs in aircraft engines that "these coatings applied to advanced, air-cooled, superalloy components will be the materials systems of choice in advanced engines for the foreseeable future".

Nesbitt and Brindley (1989) employed finite-difference thermal models to study various thermal barrier coatings in a high heat flux rocket engine. Their results showed that the use of traditional ceramic TBCs such as $ZrO_2Y_2O_3$ (zirconia) produced considerable reductions in metal temperature during testing. Air plasma sprayed and low-pressure plasma sprayed cermet coatings had much less effect on temperature than the traditional TBC system consisting of a $ZrO_2Y_2O_3$ top coat and a NiCrAlY bond coat under the same test conditions. Thermal response during testing was successfully modeled and good agreement was observed between measured and predicted temperatures at inner thrust chamber wall and also the metal/coating interface. This work was a clear demonstration that the thermal response of TBC systems could be predicted through modeling.

As an alternative to potential detriments of interfacial roughness and oxide growth experienced in conjunction with ceramic coatings, researchers have also investigated metallic TBCs as a means to

prevent coating spallation/delamination. Metallic coatings such Cu-Cr and M-Cr alloys, where M can be Ni, Co or Fe, have also been shown to be oxidation and blanching resistant, Chiang et al. (1995).

As an alternative to layered coating systems used in the studies by Miller as well as Brindley and Nesbitt, investigators recently began to consider coating systems with gradual transitions from top coat to bond coat and likewise bond coat to substrate material. These coating systems avoid the sharp interfaces, not only in geometry but also more importantly in thermal and mechanical properties, that were present in previously investigated TBCs. These gradually changing systems are known as functionally graded materials. By employing the concept of functional grading in conjunction with TBCs, investigators hoped to mitigate the detrimental effects noted by Miller while preserving the benefits of the TBC. An overview of functionally graded materials, their applications and analysis is presented next.

1.3 Functionally Graded Materials (FGMs)

Functionally graded materials (FGMs) are a relatively new class of engineered materials with spatially varied properties that optimize the overall performance of the structural component. Such materials find applications in the automotive, electronics, telecommunications, and the aerospace and defense industries. The most common type of FGM for aerospace applications consists of ceramics and metallics with a continuously graded microstructure as shown in Figure 1.8. This type of FGM, employed in the context of a thermal barrier coating, can result in reduced internal stresses and prolonged life of the coating.

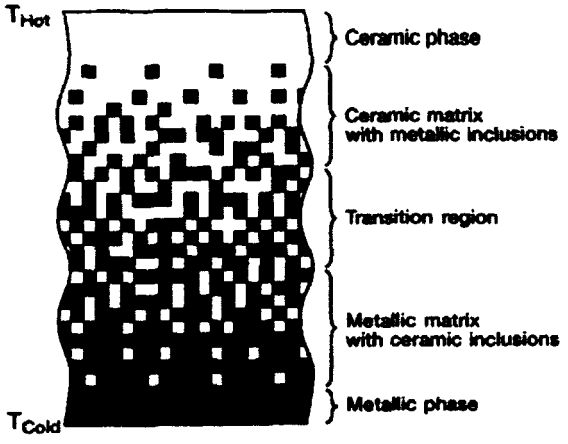

Figure 1.8. Continuously graded microstructure (source: Aboudi et al. (1999)).

The study of FGMs continues to be a very active research area as these materials have been tested under a variety of loading conditions and in numerous applications. New techniques have also been devised specifically for the analysis of FGMs. Pindera et al. (1994, 1995, 1997), Needleman and Suresh (1996), Illschner and Cherradi (1994), Shiota and Miyamoto (1996), and Suresh and Mortensen (1998) offer a broad spectrum of research in this area. To set the stage for the present work, an overview is provided below of the different approaches employed to model the thermomechanical response of FGMs.

The analysis of FGMs can be divided into two distinct categories. The first is the uncoupled micro-macrostructural approach which is limited by its accuracy to materials with very fine microstructures. In this approach, FGMs are analyzed at the macroscopic level, which reduces a given boundary value problem to a system of differential equations with variable coefficients. These variable

coefficients represent macroscopic material property variations expressed as functions of position that are obtained by local homogenization of the microstructure or taken to have specific functional forms. Sometimes, the material properties are assumed to be piecewise uniform through appropriate microstructural discretization, and the governing differential equations are solved for each layer subject to interfacial continuity and boundary conditions. Using the uncoupled approach, various researchers have developed different analytical techniques for studying particular types of FGM problems. These include thermal barrier coating and joint problems, crack problems, and design and optimization problems, as discussed extensively by Bansal and Pindera (2002) and Zhong and Pindera (2002).

The second approach employed in the analysis of functionally graded materials is the coupled approach. In this approach, the effects of microstructural variation and interaction between nonuniformly distributed inclusions are explicitly taken into account in the course of solving the governing differential equations, Pindera et al. (1995). This, in turn, facilitates more realistic (and accurate) analysis of heterogeneous materials with different microstructural scales, in contrast to the uncoupled approach which is limited to materials with very fine microstructures.

The higher-order theory for functionally graded materials (HOTFGM) is an approximate coupled approach based on a particular two-step volume discretization of the material's microstructure (into generic cells and subcells) and an averaging approach in the solution of the governing field equations in each subvolume. This theory has been developed by Aboudi, Pindera and Arnold in a sequence of papers dating back to 1993 in order to circumvent the limitations of the uncoupled approach, and summarized recently in a comprehensive article by Aboudi et al. (1999). The theory has been employed to analyze a number of technologically important problems ranging from thermally-induced free-edge interlaminar stresses in cross-ply laminates, optimization of fiber spacing in laminates subjected to thermal gradients, and thermal barrier coatings. The focus of these applications was the demonstration of microstructural coupling effects in FGMs as a function of the microstructural length scale, and when these effects can be neglected, as well as the demonstration of the utility of functionally graded microstructures in enhancing the performance of plate-like structural components subjected to through-thickness thermal gradients. Most recently, Arnold et al. (2001) employed HOTFGM to perform a thermoelastic analysis of internally cooled structures with spatially varying microstructures in two orthogonal directions. The authors demonstrated that the coolant channels could be arranged horizontally and vertically in such a manner as to achieve maximum cooling with minimal detrimental effects.

The recent developments of HOTFGM, originally formulated in the Cartesian coordinate system, include extension to cylindrical coordinates to enable analysis, design, and optimization of cylindrical structural components found in aircraft engine applications, Pindera and Aboudi (1998, 2000). This version is known as HOTCFGM.

1.4 Objectives and Outline of the Investigation

Traditionally, trial and error approaches have been employed to achieve an acceptable level of performance of RLV thrust cell liners. The challenge now is to develop and validate an efficient analysis procedure that can be used to predict failure and life in proposed designs before fabrication takes place. Such a procedure will permit optimization of the thrust cell liner in terms of strength-to-weight ratio, efficiency, durability, cost, etc. As illustrated by the previous studies regarding RLV thrust cell liners (see Section 1.1), experimental investigation is ill-suited for such a design-related purpose, as a large number of potential configurations must be examined. Furthermore, previous attempts to analyze RLV thrust cell liners have demonstrated the computational expense associated with realistic simulations, which has led researchers to employ coarse geometric representations and simplified thermo-mechanical loading cycles. Thus, a clear need exists for a thrust cell liner analysis procedure that blends efficiency with the accuracy necessary to capture the dominant factors affecting thrust cell liner performance.

This investigation employs the cylindrical version of the higher-order theory for functionally graded materials/structural components (HOTCFGM) to analyze an array of RLV thrust cell liner configurations in order to gain a better understanding of the factors affecting the performance of these liners. The cylindrical version of the higher-order theory for functionally graded materials is employed throughout for consistency as the numerical studies also address the effect of grading on local deformation and stress fields, in addition to considering many non-graded configurations.

The prevailing objective of the investigation is to isolate the thermo-inelastic material parameters in addition to the geometric parameters responsible for deformations leading to the failure modes previously observed by Quentmeyer and others. This is accomplished by first achieving an understanding of each constituent material's time-dependent inelastic behavior using an inelastic constitutive model which captures the essential features thought to play a significant role in the observed deformation modes. In turn, a series of parametric studies are conducted with the aim of addressing, for the first time, the impact of various material parameters as well as architectural details on the deformation fields of RLV thrust cell liners under in-service loading conditions. The specific parameters studied include: cooling channel wall thickness; variations in inelastic material model parameters; thermal barrier coating presence as well as its thickness; and functional grading of the coating region. Results are compared to previous work and, particularly, experimental results in an effort to determine the parameters responsible for identified failure modes in high-temperature, high-pressure RLV thrust cell liners. The employed procedure is demonstrated to provide the required efficiency to perform the large number of simulations associated with the parametric studies while preserving the accuracy needed to capture the realistic failure-related effects.

Analyzed RLV thrust cell liner systems, their constituents' material responses and the analytical foundations of HOTCFGM are described in detail in Section 2. Comparisons between HOTCFGM analysis based on two different time-dependent inelastic constitutive models and previous work are made in Section 3. In Section 4, a micromechanics model is described which is employed to determine the effective properties of graded coating regions for use in the homogenized HOTCFGM analysis. Section 5 presents the parametric studies performed as the primary means toward achieving the objectives. Finally, Section 6 summarizes the accomplishments of this work and sets forth suggestions for further studies.

2 Problem Definition and Analysis Approach

This section sets the stage for the analyses and parametric studies that have been employed to achieve the objectives of this investigation. First, the RLV thrust cell liner systems employed in identifying the key parameters responsible for deformations leading to the "dog-house" failure mode, as well as in achieving improved RLV thrust liner durability, are presented. An overview of the analysis approach is then given along with the appropriate boundary conditions and loading histories, followed by the description of the constituents and the two inelastic constitutive theories used to model them. Finally, the material characterization procedure is discussed and the resulting constant strain rate, stress-strain response and time-dependent inelastic creep and relaxation response of the constituents are presented.

2.1 RLV Thrust Cell Liner Systems

The representative cross section of the RLV thrust cell liner used throughout this investigation is identical to the cross sections used in the analyses performed by Arya and Arnold, Quentmeyer and Armstrong and others discussed in Section 1.1. The representative cross section of the cylindrical liner employed in the finite-element analysis of Arya and Arnold is shown in Figure 2.1b. Using the work of previous authors as a baseline or point of reference for the present study, a number of thrust cell liner system

configurations are designed to address the specific effects of geometry and material response on RLV thrust cell liner deformation fields. In particular, configurations are analyzed in which specific modifications in geometry and/or constituent materials are made in an attempt to understand the influence of these parameters on the substantial deformations resulting in the observed "dog-house" failure modes in the outer walls of the cooling channel.

The first such modification involves varying the cooling channel wall thickness of a thrust cell liner composed solely of NARloy-Z in two separate analyses from 35 mils to 10 mils and 50 mils. Varying the cooling channel wall thickness allows a direct comparison to the baseline case and provides an understanding of the effect of this thickness on thermal profiles, stress fields, and ultimately deformations. In each case, the inner and outer radii as well as the cooling channel maintain the same dimensions used in the baseline case. The representative cross-sections for these analyses are shown in Figure 2.1a and Figure 2.1c, respectively, with a comparison to the baseline case in which the wall thickness is 35 mils in Figure 2.1b.

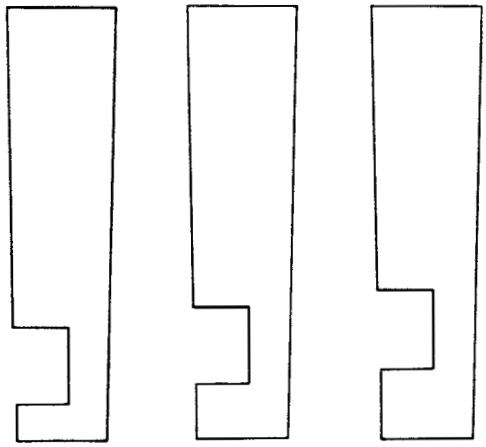

Figure 2.1. Representative cross-sectional segment of NARloy-Z thrust cell liner for varying cooling channel wall thickness: a) 10-mil wall thickness; b) 35-mil wall thickness; c) 50-mil wall thickness.

Additional configurations are also analyzed in which specific modifications in constituent materials of the liner are made. With each modification, overall dimensions of the liner and the cooling channel remain identical to those of the baseline case. In the next set of configurations, OFHC copper replaces the material above the cooling channel (i.e. the closeout material) in each of the cases shown in Figure 2.1. The resultant Cu/NARloy-Z cross-section for the 35-mil wall thickness case is shown Figure 2.2a. This cross section is representative of present-day thrust cell liner fabrication.

A major element of this study, however, involves the modeling of various thrust cell liner configurations that include coatings applied to a cooling channel wall of given thickness. For this study, low-conductivity NiCrAlY coatings are considered in combination with the 35-mil cooling channel wall thickness. Furthermore, the coating thickness parameter is studied as coatings of both 3 mils and 6 mils are analyzed. A representative thrust cell liner cross section with a coating is shown in Figure 2.2b.

The cross section shown in Figure 2.2c is consistent with functionally graded thermal barrier coatings discussed in Section 1.3. In this configuration, the sharp interfaces between NARloy-Z and the NiCrAlY coatings are eliminated through the application of grading. The graded region comprises spatially varying volume fractions of NARloy-Z and NiCrAlY, and thus separates homogenous NiCrAlY

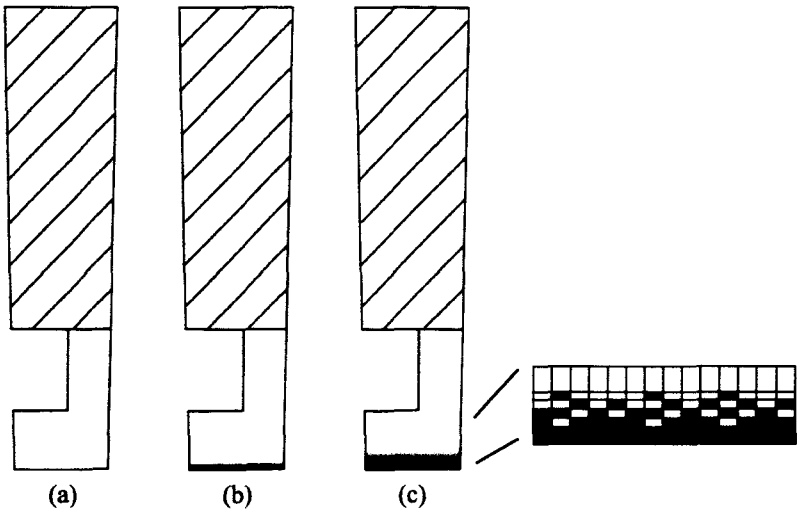

Figure 2.2. Representative cross-sectional segment of thrust cell liner for various configurations analyzed in this study (35-mil wall thickness shown): a) Cu/NARloy-Z thrust cell liner; b) Cu/NARloy-Z/NiCrAlY thrust cell liner (3-mil coating); c) Cu/NARloy-Z/FGM/NiCrAlY thrust cell liner (3-mil coating). Cu is shown by hatches, NARloy-Z is shown in white, and NiCrAlY in black.

Table 2.1. Basic configurations analyzed.

	System Constituents	*Coating Thickness*	*Wall Thickness*
1	NARloy-Z	0 mil	10 mil
2	NARloy-Z	0 mil	35 mil
3	NARloy-Z	0 mil	50 mil
4	Cu/NARloy-Z	0 mil	10 mil
5	Cu/NARloy-Z	0 mil	35 mil
6	Cu/NARloy-Z	0 mil	50 mil
7	Cu/NARloy-Z/ NiCrAlY	3 mil	35 mil
8	Cu/NARloy-Z/ NiCrAlY	6 mil	35 mil
9	Cu/NARloy-Z/grading/ NiCrAlY	1.5 mil	35 mil
10	Cu/NARloy-Z/grading/ NiCrAlY	3 mil	35 mil

from homogenous NARloy-Z. The volume fraction of NiCrAlY is highest (80%) in the layer nearest the pure NiCrAlY region, lowest (20%) in the layer nearest the pure NARloy-Z region and changes in increments of 20% across the entire graded region. Each of the four layers in the graded region is defined to be 1.5 mils in thickness. Details of the graded region are included schematically in Figure 2.2. In Section 4, we discuss a method for determining the effective homogenized properties of these heterogeneous layers and subsequently carry out the RLV analysis in Section 5 using homogenized properties as well as using the actual microstructure of the region. As was the case in the configurations in which NiCrAlY coatings were applied directly to the NARloy-Z substrate, graded NiCrAlY coatings of varying thickness are again employed. Table 2.1 summarizes the basic configurations analyzed in this investigation. Additionally, and independent of geometry and material, the effects of parameters that govern the inelastic material response described in Section 2.4 are investigated.

2.2 Method of Solution

HOTCFGM-2D is an extension of the Cartesian version of the original higher-order theory to polar coordinates to enable analysis of aircraft/aerospace engine structural components such as rotor disks, turbine blades and cylindrical thrust cell liners. The analytical framework is based on a second-order representation of temperature and displacement fields within the subvolumes used to characterize the material's functionally graded microstructure, volumetric averaging of the various field quantities within these subvolumes, and subsequent satisfaction of the field equations within each subvolume in a volumetric sense, together with the imposition of boundary and continuity conditions (both displacements and tractions) in a surface-average sense between adjacent subvolumes. This results in two systems of algebraic equations for the unknown coefficients that govern the temperature and displacement fields in the individual subvolumes of the functionally graded cylinder. When the thermal loading is of the steady-state type, the equations that govern the temperature field in each subvolume are solved first, and the results are subsequently used in the solution of the mechanical problem. When transient effects are included in the thermal loading, the two sets of equations are solved simultaneously at each time increment of the applied thermal loading history. A brief outline of the two-dimensional higher-order theory for cylindrical functionally graded structural components under steady-state or transient thermal, and steady-state mechanical, loading is provided below in order to enable proper interpretation of the results. Detailed derivation of the presented equations can be found in Pindera and Aboudi (1998, 2000).

2.2.1 Analytical Model

The microstructure of the heterogeneous cylindrical structural element shown in Figure 2.3 is discretized into N_p and N_q cells in the r-θ plane. The generic cell (p,q) used to construct the composite consists of eight subcells designated by the triplet $(\alpha\beta\gamma)$, where each index α,β,γ takes on the values 1 or 2 which indicate the relative position of the given subcell along the r, θ and z axis, respectively. The indices p and q, whose ranges are $p = 1, 2, \ldots, N_p$ and $q = 1, 2, \ldots, N_q$, identify the generic cell in the r-θ plane. The dimensions of the generic cell along the periodic z direction, l_1, l_2, are fixed for the given configuration, whereas the dimensions along the r and θ axes or the functionally graded directions, $d_1^{(p)}$, $d_2^{(p)}$, and $h_1^{(q)}$, $h_2^{(q)}$, can vary in an arbitrary fashion.

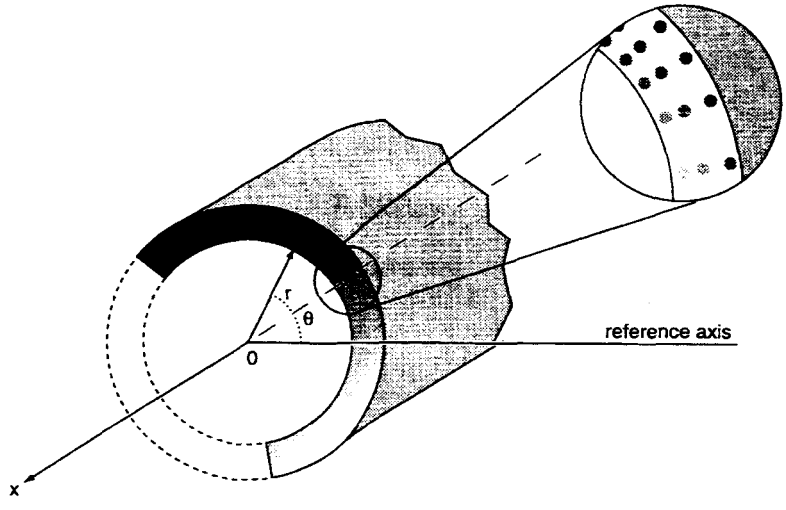

Figure 2.3. A geometric example of a structural engine component that is capable of being modeled by the cylindrical higher-order theory, HOTCFGM, used in this study.

2.2.2 Thermal Analysis

For the specified thermomechanical loading applied in the r-θ plane, an approximate solution for the temperature and displacement fields is constructed by first representing the temperature distribution in each subcell of a generic cell using a quadratic expansion in the local coordinates $\bar{r}^{(\alpha)}$, $\bar{\theta}^{(\beta)}$, $\bar{z}^{(\gamma)}$,

$$T^{(\alpha\beta\gamma)} = T^{(\alpha\beta\gamma)}_{(000)} + \bar{r}^{(\alpha)} T^{(\alpha\beta\gamma)}_{(100)} + \bar{y}^{(\beta)} T^{(\alpha\beta\gamma)}_{(010)} + \frac{1}{2}(3\bar{r}^{(\alpha)2} - \frac{d_\alpha^{(p)2}}{4}) T^{(\alpha\beta\gamma)}_{(200)} + \frac{1}{2}(3\bar{y}^{(\beta)2} - \frac{h_\beta^{(q)2}}{4}) T^{(\alpha\beta\gamma)}_{(020)} + \frac{1}{2}(3\bar{z}^{(\gamma)2} - \frac{l_\gamma^2}{4}) T^{(\alpha\beta\gamma)}_{(002)} \tag{2.1}$$

where $\bar{y}^{(\beta)} = R^{(\alpha\beta\gamma)}\bar{\theta}^{(\beta)}$ and $R^{(\alpha\beta\gamma)}$ is the distance from the origin of the r-θ-z coordinate system to the center of the $(\alpha\beta\gamma)$ subcell. Given the six unknown coefficients (i.e., $T^{(\alpha\beta\gamma)}_{(000)},\ldots,T^{(\alpha\beta\gamma)}_{(002)}$) associated with each subcell, and eight subcells within each generic cell, $48N_pN_q$ unknown quantities must be determined for a geometry with N_p rows and N_q columns of cells containing arbitrarily specified materials. These quantities are determined by first satisfying the heat conduction equation,

$$\frac{\partial q_r^{(\alpha\beta\gamma)}}{\partial \bar{r}^{(\alpha)}} + \frac{q_r^{(\alpha\beta\gamma)}}{R^{(\alpha\beta\gamma)} + \bar{r}^{(\alpha)}} + \frac{\partial q_\theta^{(\alpha\beta\gamma)}}{\partial \bar{y}^{(\beta)}} + \frac{\partial q_z^{(\alpha\beta\gamma)}}{\partial \bar{z}^{(\gamma)}} = -\rho c_p \dot{T}^{(\alpha\beta\gamma)} \tag{2.2}$$

in each subcell in a volumetric sense in view of the employed temperature field approximation. In the above, ρ and c_p are the density and the heat capacity at constant pressure of the material occupying the $(\alpha\beta\gamma)$ subcell, and the rate of change of temperature with respect to time within the subcell is denoted by $\dot{T}^{(\alpha\beta\gamma)}$. The components $q_i^{(\alpha\beta\gamma)}(i = r,\theta,z)$ of the heat flux vector in the subcell $(\alpha\beta\gamma)$ of the (p,q)th cell in Eq. (2.2) are derived from the temperature field according to

$$q_r^{(\alpha\beta\gamma)} = -k_r^{(\alpha\beta\gamma)} \frac{\partial T^{(\alpha\beta\gamma)}}{\partial \bar{r}^{(\alpha)}}, \quad q_\theta^{(\alpha\beta\gamma)} = -k_\theta^{(\alpha\beta\gamma)} \frac{\partial T^{(\alpha\beta\gamma)}}{\partial \bar{y}^{(\beta)}}, \quad q_z^{(\alpha\beta\gamma)} = -k_z^{(\alpha\beta\gamma)} \frac{\partial T^{(\alpha\beta\gamma)}}{\partial \bar{z}^{(\gamma)}} \tag{2.3}$$

where $k_i^{(\alpha\beta\gamma)}$ are the coefficients of heat conductivity of the material in the $(\alpha\beta\gamma)$ subcell.

Subsequently, continuity of heat flux and temperature is imposed in a surface-average sense at the interfaces separating adjacent subcells, as well as neighboring cells. Fulfillment of these field equations and continuity conditions, together with the imposed thermal boundary conditions applied to the bounding surface of the geometry, provides the necessary $48N_pN_q$ equations for the $48N_pN_q$ unknown coefficients in the temperature field expansion of the form:

$$\bar{\boldsymbol{\kappa}}\dot{\mathbf{T}} = \bar{\mathbf{t}}(\mathbf{T},t) = \mathbf{A}\mathbf{T}(t) + \dot{\mathbf{e}}(t) \tag{2.4}$$

where the structural thermal conductivity matrix $\bar{\boldsymbol{\kappa}}$ contains information on the geometry, thermal conductivities, densities and heat capacities of the $(\alpha\beta\gamma)$ subcells in the N_pN_q cells spanning the r and θ directions, the thermal coefficient vector $\dot{\mathbf{T}} = [\dot{\mathbf{T}}_{11}^{(111)},\ldots,\dot{\mathbf{T}}_{N_pN_q}^{(222)}]$, where $\dot{\mathbf{T}}_{pq}^{(\alpha\beta\gamma)} = [\dot{T}_{(000)},\ldots,\dot{T}_{(002)}]_{pq}^{(\alpha\alpha\beta\gamma}$, contains the unknown rates of change of the coefficients that describe the thermal field in each subcell, and the modified thermal force vector $\bar{\mathbf{t}}$ contains information on the current temperature field in the individual subcells (obtained from the previous integration step) and the applied thermal boundary

conditions. Decomposing these effects, the matrix **A** contains information on the geometry and thermal conductivities, while the vector **ė** contains information on the boundary conditions.

The above system of equations is integrated using an implicit integration algorithm to generate the temperature field in the individual subcells at each point in time during the specified thermal loading history. The employed implicit algorithm is based on the discretization of Eq. (2.4) as follows:

$$\overline{\kappa}\frac{\mathbf{T}(t+\Delta t)-\mathbf{T}(t)}{\Delta t}=\mathbf{A}[\theta\mathbf{T}(t+\Delta t)+(1.0-\theta)\mathbf{T}(t)]+\dot{\mathbf{e}}(t) \tag{2.5}$$

Setting $\theta = 0.0$ produces the explicit algorithm which requires a very small Δt increment for convergence. With $\theta = 0.5$ or 1.0, Δt can be as large as 1.0, producing a dramatic execution-time reduction.

In the absence of transient thermal loading (i.e. steady-state case when the diffusion effects can be neglected), the right-hand side of Eq. (2.2) becomes zero, and the final system of equations becomes:

$$\boldsymbol{\kappa}\mathbf{T}=\mathbf{t} \tag{2.6}$$

where the structural thermal conductivity matrix $\boldsymbol{\kappa}$ contains information on the geometry and the thermal conductivities of the subcells $(\alpha\beta\gamma)$ in the N_pN_q cells spanning the r and θ functionally graded directions, the thermal coefficient vector **T** contains the unknown coefficients that describe the thermal field in each subcell, i.e., $\mathbf{T}=[\mathbf{T}_{11}^{(111)},...,\mathbf{T}_{N_pN_q}^{(222)}]$ where $\mathbf{T}_{pq}^{(\alpha\beta\gamma)}=[T_{(000)},...,T_{(002)}]_{pq}^{(\alpha\beta\gamma)}$, and the modified thermal force vector **t** contains information on the thermal boundary conditions.

2.2.3 Mechanical Analysis

Once the temperature field is known, the resulting displacement and stress fields are determined by approximating the displacement field in each subcell of a generic cell using a quadratic expansion in the local coordinates $\bar{r}^{(\alpha)}$, $\bar{\theta}^{(\beta)}$, $\bar{z}^{(\gamma)}$ as follows:

$$\begin{aligned}u_r^{(\alpha\beta\gamma)}=&W_{1(000)}^{(\alpha\beta\gamma)}+\bar{r}^{(\alpha)}W_{1(100)}^{(\alpha\beta\gamma)}+\bar{y}^{(\beta)}W_{1(010)}^{(\alpha\beta\gamma)}+\frac{1}{2}(3\bar{r}^{(\alpha)2}-\frac{d_\alpha^{(p)2}}{4})W_{1(200)}^{(\alpha\beta\gamma)}\\&+\frac{1}{2}(3\bar{y}^{(\beta)2}-\frac{h_\beta^{(q)2}}{4})W_{1(020)}^{(\alpha\beta\gamma)}+\frac{1}{2}(3\bar{z}^{(\gamma)2}-\frac{l_\gamma^2}{4})W_{1(002)}^{(\alpha\beta\gamma)}\end{aligned} \tag{2.7}$$

$$\begin{aligned}u_\theta^{(\alpha\beta\gamma)}=&W_{2(000)}^{(\alpha\beta\gamma)}+\bar{r}^{(\alpha)}W_{2(100)}^{(\alpha\beta\gamma)}+\bar{y}^{(\beta)}W_{2(010)}^{(\alpha\beta\gamma)}+\frac{1}{2}(3\bar{r}^{(\alpha)2}-\frac{d_\alpha^{(p)2}}{4})W_{2(200)}^{(\alpha\beta\gamma)}\\&+\frac{1}{2}(3\bar{y}^{(\beta)2}-\frac{h_\beta^{(q)2}}{4})W_{2(020)}^{(\alpha\beta\gamma)}+\frac{1}{2}(3\bar{z}^{(\gamma)2}-\frac{l_\gamma^2}{4})W_{2(002)}^{(\alpha\beta\gamma)}\end{aligned} \tag{2.8}$$

$$u_z^{(\alpha\beta\gamma)}=W_{3(000)}^{(\alpha\beta\gamma)}+\bar{z}^{(\gamma)}W_{3(001)}^{(\alpha\beta\gamma)} \tag{2.9}$$

where the unknown coefficients $W_{i(lmn)}^{(\alpha\beta\gamma)}$ $(i=1,2,3)$ are determined from conditions similar to those employed in the thermal problem. In this case, there are 104 unknown quantities in a generic cell (p,q). The determination of these quantities parallels that of the thermal problem with the thermal equations and quantities replaced by their mechanical analogues as briefly described below.

First, the heat conduction equation is replaced by the three equilibrium equations,

$$\frac{\partial \sigma_{rr}^{(\alpha\beta\gamma)}}{\partial \bar{r}^{(\alpha)}}+\frac{\partial \sigma_{r\theta}^{(\alpha\beta\gamma)}}{\partial \bar{y}^{(\beta)}}+\frac{\partial \sigma_{rz}^{(\alpha\beta\gamma)}}{\partial \bar{z}^{(\gamma)}}+\frac{\sigma_{rr}^{(\alpha\beta\gamma)}-\sigma_{\theta\theta}^{(\alpha\beta\gamma)}}{R^{(\alpha\beta\gamma)}+\bar{r}^{(\alpha)}}+F_{\bar{r}}^{(\alpha\beta\gamma)}=0 \tag{2.10}$$

$$\frac{\partial \sigma_{r\theta}^{(\alpha\beta\gamma)}}{\partial \bar{r}^{(\alpha)}}+\frac{\partial \sigma_{\theta\theta}^{(\alpha\beta\gamma)}}{\partial \bar{y}^{(\beta)}}+\frac{\partial \sigma_{\theta z}^{(\alpha\beta\gamma)}}{\partial \bar{z}^{(\gamma)}}+\frac{2\sigma_{r\theta}^{(\alpha\beta\gamma)}}{R^{(\alpha\beta\gamma)}+\bar{r}^{(\alpha)}}+F_{\bar{\theta}}^{(\alpha\beta\gamma)}=0 \tag{2.11}$$

$$\frac{\partial \sigma_{rz}^{(\alpha\beta\gamma)}}{\partial \bar{r}^{(\alpha)}}+\frac{\partial \sigma_{\theta z}^{(\alpha\beta\gamma)}}{\partial \bar{y}^{(\beta)}}+\frac{\partial \sigma_{zz}^{(\alpha\beta\gamma)}}{\partial \bar{z}^{(\gamma)}}+\frac{\sigma_{rz}^{(\alpha\beta\gamma)}}{R^{(\alpha\beta\gamma)}+\bar{r}^{(\alpha)}}=0 \tag{2.12}$$

where $F_{\bar{r}}^{(\alpha\beta\gamma)}$ and $F_{\bar{\theta}}^{(\alpha\beta\gamma)}$ are the components of the body force due to the radial and angular acceleration. The components of the stress tensor, assuming that the material occupying the subcell $(\alpha\beta\gamma)$ of the (p,q)th cell is orthotropic, are related to the strain components through the generalized Hooke's law:

$$\sigma_{ij}^{(\alpha\beta\gamma)}=\mathrm{c}_{ijkl}^{(\alpha\beta\gamma)}(\varepsilon_{kl}^{(\alpha\beta\gamma)}-\varepsilon_{kl}^{\mathrm{in}(\alpha\beta\gamma)})-\Gamma_{ij}^{(\alpha\beta\gamma)}T^{(\alpha\beta\gamma)} \tag{2.13}$$

where $c_{ijkl}^{(\alpha\beta\gamma)}$ are the elements of the stiffness tensor, $\varepsilon_{kl}^{in(\alpha\beta\gamma)}$ are the inelastic strain components, and the elements $\Gamma_{ij}^{(\alpha\beta\gamma)}$ of the so-called thermal tensor are the products of the stiffness tensor and the thermal expansion coefficients. In this investigation, we consider transversely isotropic elastic or isotropic inelastic materials. Hence, in the latter case Eq. (2.13) reduces to:

$$\sigma_{ij}^{(\alpha\beta\gamma)}=\lambda_{(\alpha\beta\gamma)}\varepsilon_{kk}^{(\alpha\beta\gamma)}\delta_{ij}+2\mu_{(\alpha\beta\gamma)}\varepsilon_{ij}^{(\alpha\beta\gamma)}\delta_{ij}+2\mu_{(\alpha\beta\gamma)}\varepsilon_{ij}^{in(\alpha\beta\gamma)}-\Gamma_{\mathrm{ij}}^{(\alpha\beta\gamma)}T^{(\alpha\beta\gamma)} \tag{2.14}$$

where $\lambda_{(\alpha\beta\gamma)}$ and $\mu_{(\alpha\beta\gamma)}$ are the Lame's constants of the material filling the given $(\alpha\beta\gamma)$ subcell. The components of the strain tensor in the individual subcells are, in turn, obtained from the strain-displacement relations. Second, the continuity of tractions and displacements at the various interfaces replaces the continuity of heat fluxes and temperature. Finally, the boundary conditions now involve the appropriate mechanical quantities.

Application of the above equations and conditions in a volumetric and surface-average sense, respectively, produces a system of $104N_pN_q$ algebraic equations in the field variables within the cells of the functionally graded geometry of the form:

$$\mathbf{KU}=\mathbf{f}+\mathbf{g} \tag{2.15}$$

where the structural stiffness matrix $\mathbf{K}$ contains information on the geometry and thermomechanical properties of the individual $(\alpha\beta\gamma)$ subcells within the cells comprising the graded composite, the displacement coefficient vector $\mathbf{U}$ contains the unknown coefficients that describe the displacement field in each subcell, i.e., $\mathbf{U}=[\mathbf{U}_{11}^{(111)},...,\mathbf{U}_{\mathrm{N}_p\mathrm{N}_q}^{(222)}]$ where $\mathbf{U}_{qr}^{(\alpha\beta\gamma)}=[W_{1(000)},...,W_{3(001)}]_{qr}^{(\alpha\beta\gamma)}$, and the mechanical force vector $\mathbf{f}$ contains information on the thermal boundary conditions, body forces and thermal loading effects generated by the applied temperature or heat flux. In addition, the inelastic force vector $\mathbf{g}$ on the right-hand side of Eq. (2.15) contains inelastic effects given in terms of the integrals of inelastic strain distributions $\varepsilon_{kl}^{in(\alpha\beta\gamma)}(\bar{r}^{(\alpha)},\bar{y}^{(\beta)},\bar{z}^{(\gamma)})$ that are represented by the coefficients $R_{ij(l,m,n)}^{(\alpha\beta\gamma)}$,

$$R_{ij(l,m,n)}^{(\alpha\beta\gamma)}=\frac{\mu_{(\alpha\beta\gamma)}}{4}\Lambda_{(l,m,n)}\int_{-1}^{1}\int_{-1}^{1}\int_{-1}^{1}\varepsilon_{ij}^{in(\alpha\beta\gamma)}P_l(\zeta_1^{(\alpha)})P_m(\zeta_2^{(\beta)})P_n(\zeta_3^{(\gamma)})d\zeta_1^{(\alpha)}d\zeta_2^{(\beta)}d\zeta_3^{(\gamma)} \tag{2.16}$$

where $\Lambda_{(l,m,n)} = \sqrt{(1+2l)(1+2m)(1+2n)}$, and the non-dimensionalized variables, $\zeta_i^{(\cdot)}$, defined in the interval $1 \leqslant \zeta_i^{(\cdot)} \leqslant 1$, are given in terms of the local subcell coordinates as follows:

$$\zeta_1^{(\alpha)} = \bar{r}^{(\alpha)} / (d_\alpha^{(p)} / 2), \quad \zeta_2^{(\beta)} = \bar{y}^{(\beta)} / (h_\beta^{(q)} / 2) \quad \zeta_3^{(\gamma)} = \bar{z}^{(\gamma)} / (l_\gamma / 2)$$

and where $P_l(\cdot)$, $P_m(\cdot)$, and $P_n(\cdot)$ are Legendre polynomials of order *l*, *m* and *n*. These integrals depend implicitly on the elements of the displacement coefficient vector $\mathbf{U}$, requiring an incremental solution of Eq. (2.15) at each point along the loading path. As mentioned previously, the solution of this system of equations follows that of the thermal problem in the case of steady-state thermal loading, while for the transient thermal loading the two problems (thermal and mechanical) must be solved simultaneously. The outlined formulation is sufficiently general to admit either rate-independent incremental plasticity, rate-dependent creep or unified viscoplasticity constitutive theories.

2.3 Geometry, Mesh Discretization and Boundary Conditions

Figure 2.4 shows the detailed dimensions of each of the basic representative cross sections employed in this study. As in the analysis performed by Arya and Arnold, the inner radius of the thrust chamber is 33.02 mm, while the outer radius is 40.13 mm. Although only half of the cooling channel is included in the representative cross section, the full cooling channel measures 1.27 mm in height and 1.69 mm in width and is consistent with the small-scale thrust cell liners tested by Quentmeyer and others.

The baseline NARloy-Z cross section shown in Figure 2.1b was discretized into 14 subcells in the circumferential direction and 40 subcells in the radial direction for analysis using the cylindrical higher-order theory outlined above. Preliminary studies showed this discretization to produce identical global temperature, stress, strain and deformation fields compared to a more discretized mesh, thus this mesh discretization is considered convergent. In contrast, the finite-element model employed by Arya and Arnold contained only 35 elements and the authors demonstrate no evidence that this small number of elements is adequate to reach convergence.

The analyses in which the cooling channel is relocated to vary the cooling channel wall thickness utilize a similar volume discretization of the cross-sectional element as that employed in the baseline case. However, the 40 subcells in the radial direction are spatially redistributed to account for the differences in geometry. Figure 2.4 shows the details of the mesh discretization, in Cartesian coordinates for the sake of graphical resolution clarity only, for each NARloy-Z cross section considered. Likewise, the analysis of the Cu/NARloy-Z cross section shown in Figure 2.2a also employs a discretization of 14 subcells in the circumferential direction and 40 subcells in the radial direction.

In the cases employing a coating, however, the grid is refined slightly in the region of the coating to allow the use of very thin coatings relative to the cooling channel wall thickness. These changes result in discretizations of 14 subcells in the circumferential direction and 42 subcells in the radial direction for 3-mil coating case and 44 subcells in the radial direction for 6-mil coating case. A mesh of 44 subcells in the radial direction and 14 subcells in the circumferential direction is also employed in the analysis of the graded cross sections. For these cases, however, the mesh is slightly refined in order to form the graded region consisting of four relatively thin layers. The mesh discretizations for the Cu/NARloy-Z case, the two cases employing coatings of 3 and 6 mils, respectively, and the cases employing grading are shown in Figure 2.5.

Identical thermal and mechanical boundary conditions are employed in each analysis herein. The inner radius of the thrust cell liner forms the outer boundary of the combustion chamber and is, therefore,

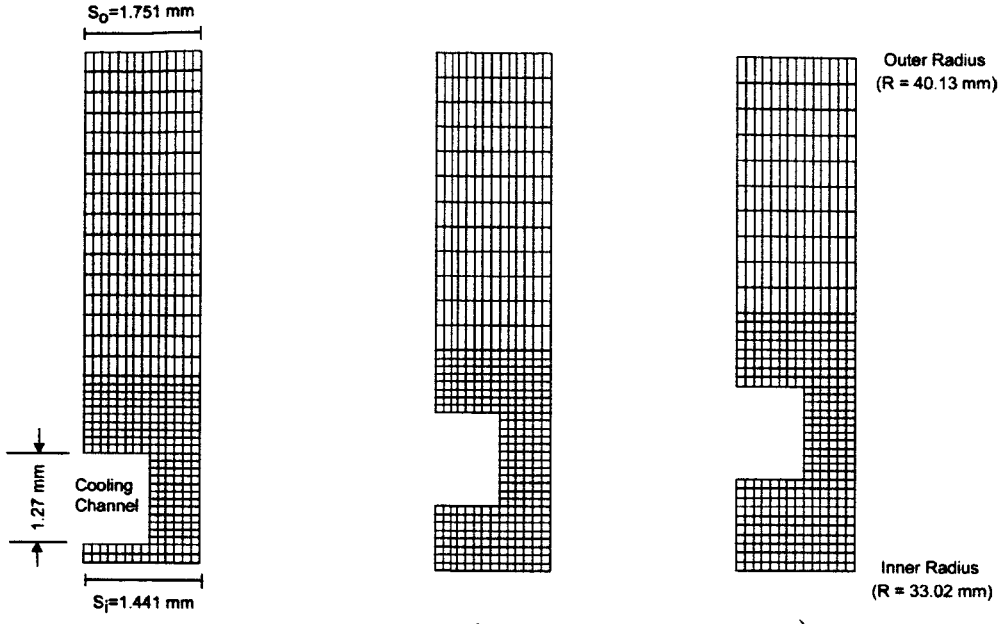

Figure 2.4. Representative mesh discretization of cross-sectional segments of NARloy-Z thrust cell liner for varying cooling channel wall thickness: a) 10-mil wall thickness; b) 35-mil wall thickness; c) 50-mil wall thickness.

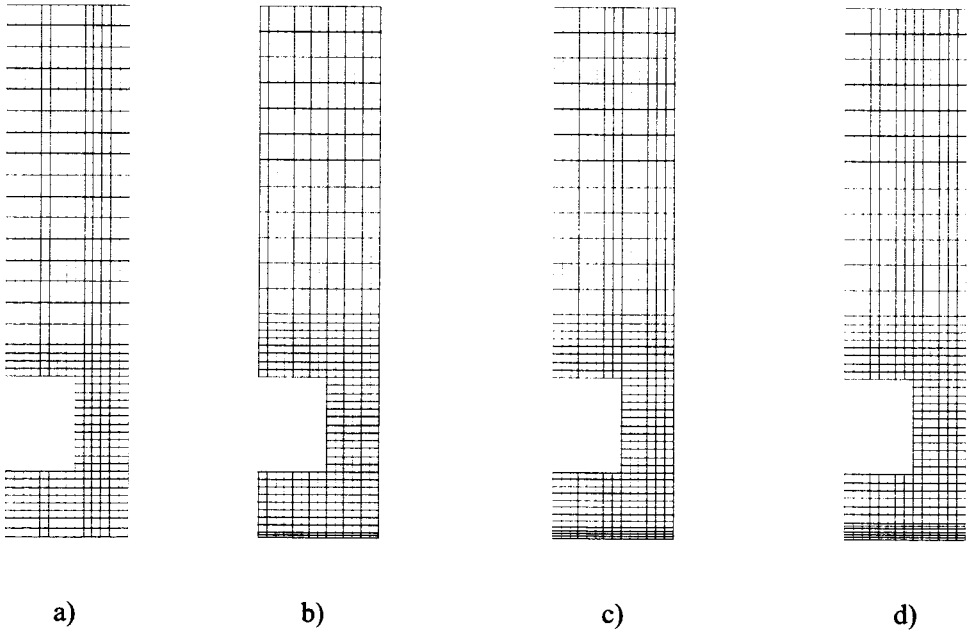

Figure 2.5. Representative mesh discretization of cross-sectional segments of various thrust cell liners a) Cu/NARloy-Z; b) Cu/NARloy-Z/NiCrAlY (3-mil coating); c) Cu/NARloy-Z/grading/NiCrAlY (6-mil coating); d) Cu/NARloy-Z/grading/NiCrAlY.

free to expand or contract with temperature and pressure. Heat from the combustion chamber is transmitted to the thrust cell liner through a convective boundary condition given by

$$q = h_s(T_\infty - T_s) \tag{2.17}$$

where h_s is the convective coefficient for a given boundary, and T_∞, T_s are the environmental and surface temperatures. Likewise, heat is removed from the liner primarily via the convective cooling channels. A convective boundary condition is also employed at the outside radius of the thrust cell liner, allowing heat to escape at this surface. The environmental temperature, T_∞, at the outer radius is defined to be 25 °C. The convective coefficients employed at the inner and outer radii as well as in the cooling channel are presented in Table 2.2 and mirror those employed by Arya and Arnold (1991). The left and right sides of the representative cross section employ zero flux boundary conditions, ensuring symmetric temperature fields across these lines of symmetry. The isotropic thermal conductivities for each constituent material appearing in the Fourier's heat conduction equation, Eq. (2.3), are given in Table 2.3, where the thermal conductivities of NARloy-Z, OFHC copper and NiCrAlY are taken from Arya and Arnold (1991), Esposito and Zabora (1975) and Brandt et al. (1986), respectively. Tables 2.4 and 2.5 show the density and specific heat, respectively, given by these authors for each material.

Table 2.2. Employed convection coefficients, h_s

Inner radius $(W/m^2 \cdot K)$	Outer Radius $(W/m^2 \cdot K)$	Cooling Channel $(W/m^2 \cdot K)$
2.02E+04	6.10E+00	4.83E+04

Table 2.3. Employed thermal conductivities, κ

NARloy-Z $(W/m \cdot K)$	OFHC copper $(W/m \cdot K)$	NiCrAlY $(W/m \cdot K)$
341.0	390.0	12.5

Table 2.4. Employed densities, ρ

NARloy-Z (kg/m^3)	OFHC copper (kg/m^3)	NiCrAlY (kg/m^3)
8900.0	8913.0	6900.0

Table 2.5. Employed specific heats, c_p

NARloy-Z $(J/kg \cdot K)$	OFHC copper $(J/kg \cdot K)$	NiCrAlY $(J/kg \cdot K)$
380.0	385.0	525.0

Pressure is applied in the combustion chamber at the inner radius of the thrust cell liner and within the cooling channel in the manner described below, otherwise these surfaces are unconstrained. The outer radius of the thrust cell liner is constrained in the radial direction and a zero shear stress condition is imposed. This is consistent with the physical application in which the thrust cell liner is enclosed by a steel jacket, thereby preventing radial expansion. The boundary conditions imposed on the radial boundaries are consistent with the deformation of the entire cylindrical liner having 72 cooling channels. Again, the left and right sides of the representative cross section are modeled using the appropriate symmetry boundary conditions, thus these edges are constrained circumferentially and the rotations are set to zero according to

$$\frac{\partial u_r}{\partial \theta} = 0 \tag{2.18}$$

In the radial direction these edges are free from constraint and allowed to translate according to the boundary conditions employed at the inner and outer radii of the cross section.

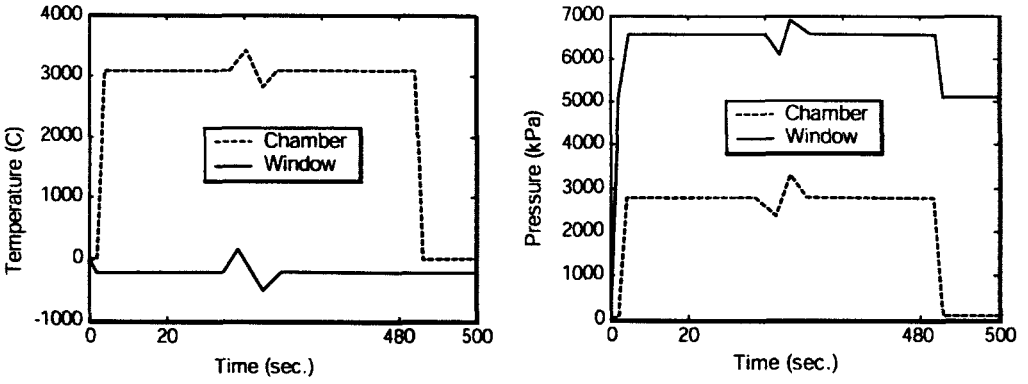

Figure 2.6. Temperature (left) and pressure (right) profiles for the thermal and pressure cycles within the combustion chamber and the cooling channel.

The thermal cycle history employed for each of the investigated configurations is similar to the extended duration cycle used by Arya and Arnold, except that the hot phase of the cycle was lengthened to 480 seconds to be more consistent with the typical SSME cycle. Temperature and pressure variations with time at the inner radius of the cross section and the internal cooling channel walls are shown in Figure 2.6. In the combustion chamber, the temperature and pressure are initially kept at 0°C and 96.5 kPa, respectively, for 1.0 second while the coolant, maintained at -228°C and pressurized to 5,100 kPa, circulates through the cooling channel. At t = 1.0 second, the chamber temperature is increased (or ramped) from 0°C to 3,086°C in 1.0 second, kept at this level for 480 seconds, and subsequently decreased back to 0°C in 1.0 second. Meanwhile, the temperature of the coolant in the channel is held constant, while the pressure is increased at t = 1.0 second from 5,100 kPa to 6,550 kPa in 1.0 second, kept at this level for 480 seconds, and subsequently decreased back to 5,100 kPa in 1.0 second. The temperature and pressure in both the chamber and channel are then maintained at constant levels for the duration of the cycle, which takes a total of 500 seconds to complete.

2.4 Constituents' Material Response

As discussed in Section 1.1, Arya and Arnold (1991) concluded that the characteristic deformation of thrust cell liners under extreme loading conditions is driven not only by biasing pressure differential, but

also by time-dependent inelastic material response. The aims of this section are to discuss the manner of characterizing the inelastic material response of the different constituents employed in this investigation, and to gain an understanding how different parameters influence this response. This is necessary in order to correlate the numerical results presented in Section 5 to the response of the different constituents.

Two types of approaches are commonly utilized to model inelastic material response: uncoupled theories and coupled theories. Uncoupled theories treat elastic, thermal and inelastic strains as distinct and uncoupled. By linear strain rate superposition, the general form for such a model is based on the equation

$$\dot{\varepsilon} = \dot{\varepsilon}^{el} + \dot{\varepsilon}^{th} + \dot{\varepsilon}^{in} \tag{2.19}$$

where the inelastic component is further decomposed into time-independent (plastic) and time-dependent (creep) contributions:

$$\dot{\varepsilon}^{in} = \dot{\varepsilon}^{pl} + \dot{\varepsilon}^{cr} \tag{2.20}$$

The respective inelastic components are modeled independently using incremental plasticity theory and various creep models. Coupled theories account for elastic, thermal and inelastic strains in the same general form as uncoupled theories as shown in Eq. (2.19). In contrast, however, coupled theories treat the inelastic component within a unified framework in which time-dependent and time-independent contributions are not distinctly separated. Although such coupled approaches are capable of accounting for possible creep and plasticity interactions, they typically involve stiff differential equations which are difficult to integrate.

At the outset of this study, the unified viscoplasticity theory developed by Robinson (1982) was incorporated into the cylindrical version of higher-order theory for functionally graded materials and validated. Robinson's model was employed to establish baseline results and compare the predictions to Arya and Arnold's results in order to determine whether the deformation was correctly captured. The analytical framework of Robinson's model is briefly outlined in Section 2.4.1. This model, however, proved to be computationally demanding due to its intrinsic stiff differential equations, thus limiting the number of analyses which could be performed. Assuming that creep effects dominate and creep/plasticity interactions are relatively small for the employed loading history, the uncoupled power-law creep model discussed in Section 2.4.2 was employed in place of Robinson's model. This, in turn, facilitated the incorporation of an implicit integration algorithm into the cylindrical version of the higher-order theory, thereby enabling efficient generation of numerical results. This modification reduced computation times by a factor of approximately 5, which becomes particularly important when considering any significant mesh refinement in order to accommodate a specific coating system. It is the power-law creep constitutive model and the modified version of the higher-order theory, with the efficient implicit integration scheme, which were employed in the parametric studies of the cylindrical thrust chamber liner systems described in Section 2.1. We point out, however, that the efficiency gained through the use of the power-law creep model may potentially have some adverse impact on the quality of generated results as the plasticity effects present in the Robinson model are absent in the power-law creep model.

The time-dependent inelastic response of engineering materials can be characterized through a series of tests in order to determine the various parameters in the constitutive models. Three types of tests are typically employed: constant strain-rate tests, creep tests and relaxation tests. The constant strain-rate test establishes the strain-rate sensitivity of a given material and is conducted by straining a specimen at a constant rate while continuously monitoring strain and stress. The stress and strain data in turn are used to construct a constant strain-rate, stress-strain curve as shown in Figure 2.7. The effects of temperature and loading rate are also noted in Figure 2.7, as increasing the temperature tends to force the curve lower, while increasing the strain rate drives the curve higher.

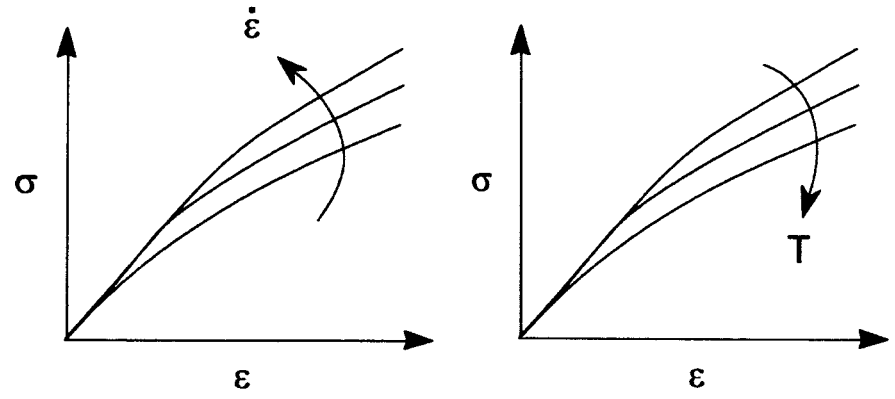

Figure 2.7. Representative constant strain rate stress-strain curves as a function of strain-rate (left) and temperature (right).

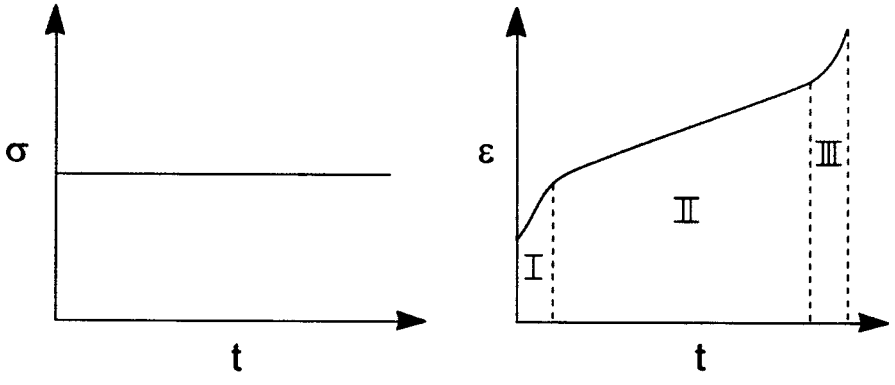

Figure 2.8. Applied loading (left) and resultant creep curve (right) for typical creep test.

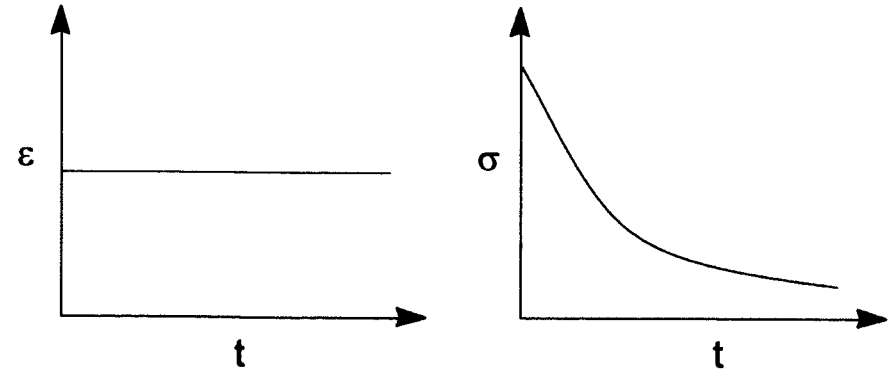

Figure 2.9. Applied loading (left) and resultant stress relaxation (right) for typical relaxation test.

Creep is defined as time-dependent inelastic deformation under a constant load. Deformation by creep is of particular concern for structural materials used in high temperature applications such as turbine blades or thrust chambers of high-performance engines. A creep test provides a means for determining the time-dependent inelastic properties of metals and alloys to be used in such high-temperature

applications. In a typical creep test, a specimen is subjected to a constant tensile load or stress for a period of time under constant temperature while elongation is recorded as a function of time. Plotting elongation versus time results in the creep curve shown schematically in Figure 2.8. The typical creep curve can be divided into three distinct regions: primary creep, secondary creep and tertiary creep. Primary or transient creep is characterized by a continuously decreasing creep rate resulting from strain hardening of the material under load. The linear region of the typical creep curve is identified as secondary or steady-state creep. The creep rate remains constant throughout the secondary creep stage as the effects of strain hardening and recovery balance each other. The power-law creep model is intended to model steady-state creep only. During the tertiary creep stage, the creep rate no longer remains constant but rather increases with time ultimately resulting in failure.

Over time, stresses in a material subjected to a constant strain tend to decrease. This phenomenon is appropriately known as stress relaxation. A stress relaxation test is another tool used to quantify the time-dependent inelastic behavior of materials. In this test, an instantaneous strain of a given magnitude is imposed on a specimen and maintained over time while the stresses (forces) necessary to maintain the initial strain are recorded. Plotting stress versus time gives the stress relaxation curve as shown schematically in Figure 2.9. As in the creep test, results differ with strain level and temperature.

2.4.1 Robinson's Unified Viscoplasticity Theory

Arnold (1987) provides the full derivation of Robinson's potential-based unified viscoplastic theory. Only the basic framework is presented herein.

According to Robinson's theory, the flow law for the inelastic strain rates is given by

$$\dot{\varepsilon}_{ij}^{p} = \frac{AF^{n}\Sigma_{ij}}{\sqrt{J_2'}} \text{ when } s_{ij}\Sigma_{ij} > 0 \text{ and } F > 0 \tag{2.21}$$

$$\dot{\varepsilon}_{ij}^{p} = 0 \text{ when } s_{ij}\Sigma_{ij} \le 0 \text{ and } F \le 0 \text{ or } F > 0 \tag{2.22}$$

where $\boldsymbol{\Sigma} = \boldsymbol{s} - \boldsymbol{a}$, $\boldsymbol{s}$ and $\boldsymbol{a}$ are the deviatoric stress components and deviatoric back stress components, respectively, J_2' is the second invariant of $\boldsymbol{\Sigma}$, that is $J_2' = \boldsymbol{\Sigma} \cdot \boldsymbol{\Sigma}/2$, and the function $F = J_2'/K^2 - 1$ may be thought of as a Bingham-Prager threshold function since the parameter K may be identified as a Bingham-Prager threshold shear stress.

The evolution law for the back stress is given by

$$\dot{a}_{ij} = \frac{H}{G^{\beta}}\dot{\varepsilon}_{ij}^{p} - \frac{RG^{m-\beta}}{\sqrt{I_2}}a_{ij} \text{ when } s_{ij}a_{ij} > 0 \text{ and } G > G_0 \tag{2.23}$$

$$\dot{a}_{ij} = \frac{H}{G^{\beta}}\dot{\varepsilon}_{ij}^{p} - \frac{RG_0^{m-\beta}}{\sqrt{I_2}}a_{ij} \text{ when } s_{ij}a_{ij} \le 0 \text{ and } G \le G_0 \text{ or } G > G_0 \tag{2.24}$$

where I_2 is the second invariant of a_{ij}, that is $I_2 = \boldsymbol{a} \cdot \boldsymbol{a}/2$, the function G is $G = I_2/K_0^2$, and the recovery term R is given by

$$R = R_0 \exp[Q_0(\frac{1}{T_0} - \frac{1}{T})] \tag{2.25}$$

where the parameter Q_0 is the activation energy for the material and T_0 is a reference temperature.

There are eight material properties that characterize the response of a material: A, n, m, β, H, R, G_0 and K. The parameters A and n are constant and influence the hardening behavior of the inelastic strain rates. The parameters m, R, and G_0 are related to the thermal recovery mechanism in the back stress while β and H influence the hardening behavior of the back stress. Of these terms, m and G_0 are constant, while H depends on temperature. The value of K at the reference temperature T_0 is K_0.

The constituents' material parameters for Robinson's model on the basis of the three test methods described above, namely constant strain rate stress-strain response, creep response and relaxation response, provide complete elastic and inelastic characterization of the isotropic constituents. Of the three constituents employed in this study, NARloy-Z is the only material for which Robinson model characterization has been conducted, thus Robinson model parameters for OFHC copper and NiCrAlY are unavailable. The Robinson model elastic and inelastic parameters for NARloy-Z given by Williams and Pindera (1994) are shown in Table 2.6 and Table 2.7, respectively. Given these material parameters, the Multiple Concentric Cylinder Model (MCCM) developed by Williams and Pindera (1994) was employed to generate the constant strain rate, stress-strain response of NARloy-Z based on the Robinson's model and shown in the right side of Figure 2.10. The predicted curves compare favorably with the experimental data generated by Esposito and Zabora (1975) and shown on the left of Figure 2.10.

Table 2.6. Robinson model elastic parameters for NARloy-Z

E (*GPa*)	ν	α (10^{-6}/°C)
147	0.34	17.85

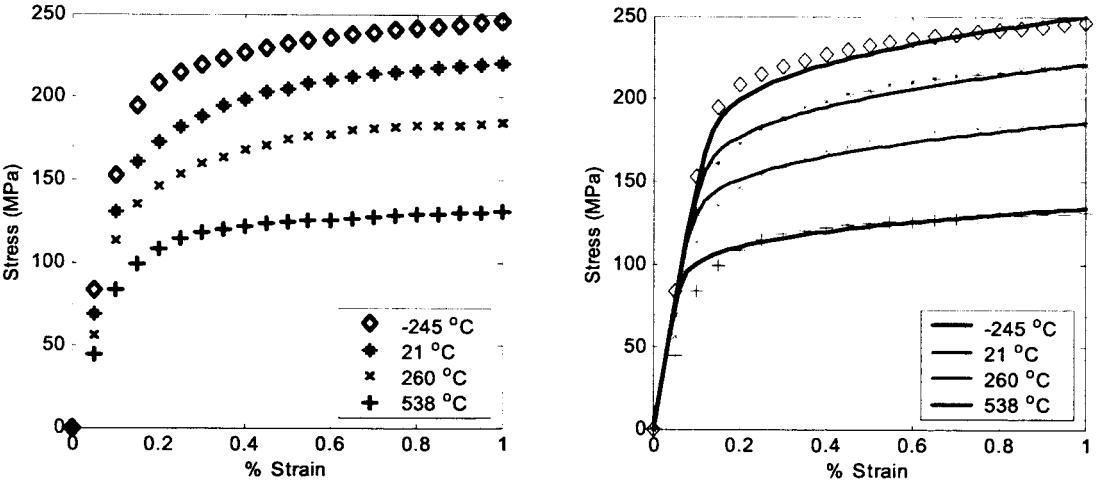

Experimental results

Robinson model predictions

Figure 2.10. Temperature-dependent NARloy-Z stress-strain data of Esposito and Zabora (1975) and predicted NARloy-Z stress-strain response using the Robinson parameters shown in Tables 2.6-2.7.

MCCM was also employed to generate creep and relaxation responses of NARloy-Z according to the Robinson model parameters. Figure 2.11 shows the predicted creep and relaxation curves of this alloy

Table 2.7. Robinson model inelastic parameters for NARloy-Z

Temp (K)	β	H (GPa)	R_0 (MPa/hr)	Q_0 (K)	T_0 (K)	K_0^2 (MPa)	K^2 (MPa)
28	0.8004	24.945	0.000E+00	40,000	811	15.543	68.004
294	0.8461	22.851	5.663E-30	40,000	811	15.543	50.182
533	0.9514	18.683	1.400E-03	40,000	811	15.543	34.169
811	1.1506	12.779	1.472E+08	40,000	811	15.543	15.543

A (10^{-6}/hr)	m	n	G_0
138.5	4.365	4.0	0.04

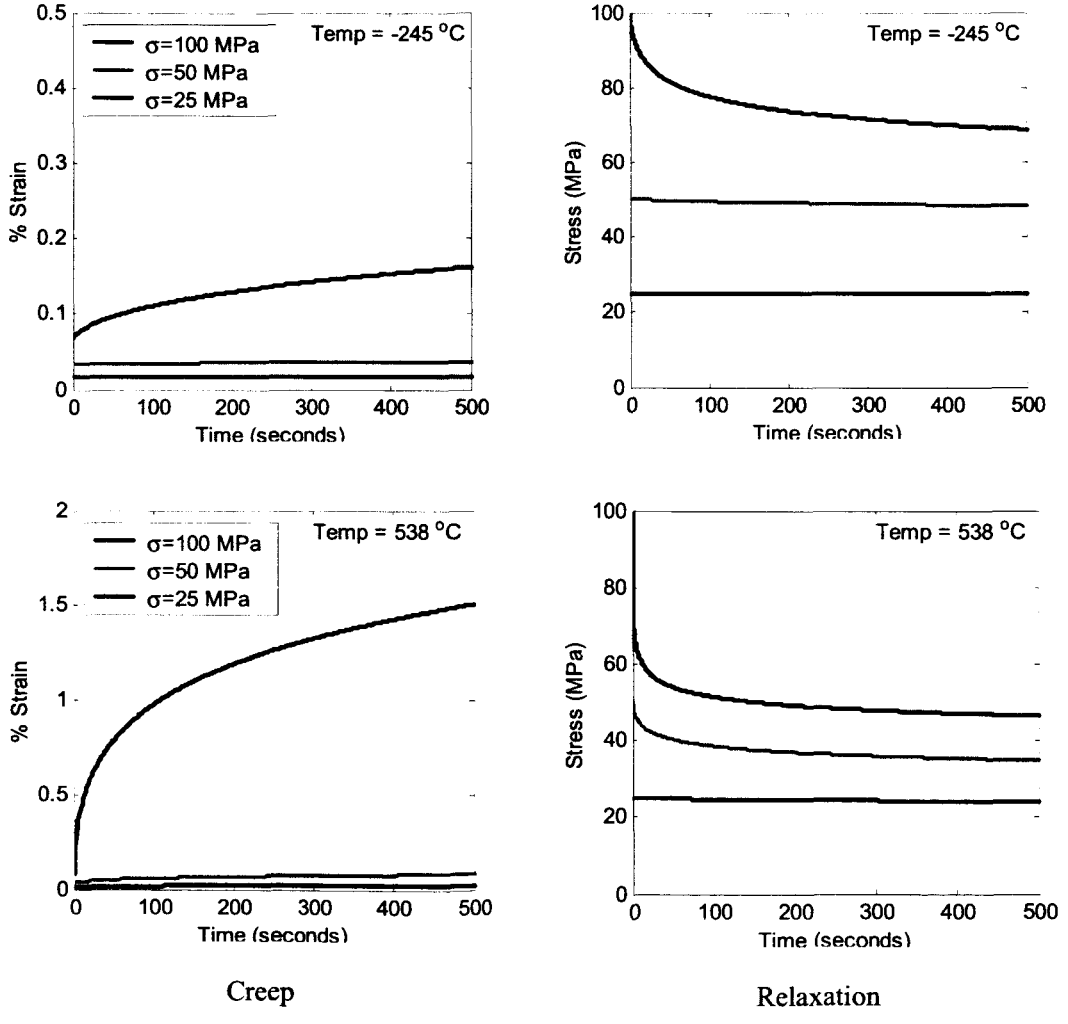

Figure 2.11. Creep and stress relaxation for NARloy-Z at -245 °C and 538 °C as predicted by Robinson's model.

at the extreme temperatures of –245 °C and 538 °C, respectively. Each result is presented over a 500-second time period matching the cycle history shown in Figure 2.6. Creep tests are simulated at constant stresses of 25, 50 and 100 MPa. Similarly, relaxation tests are simulated by imposing constant strains corresponding to these initial stress values. The results presented in Figure 2.11 demonstrate that creep and stress relaxation behavior is both temperature and stress dependent.

2.4.2 Power-Law Creep Model

The power-law creep model is intended to capture the linear portion of the typical creep curve or secondary creep only. This model is commonly employed to simulate high-temperature behavior of metals and alloys under the assumptions that primary creep is negligible and the material does not reach the tertiary creep stage, thus it is forced to stay in steady state. In this investigation, the power-law creep equation used to model the time-dependent response of different constituents under multi-axial loading situations is taken in the form,

$$\dot{\varepsilon}_{ij}^{c} = \frac{3F(\sigma_e, T)}{2\sigma_e}\sigma_{ij}' \tag{2.26}$$

where σ_{ij}' are the components of the stress deviator, $\sigma_e = \sqrt{3/2\sigma_{ij}'\sigma_{ij}'}$, and

$$F(\sigma_e, T) = A(T)\sigma_e^{n(T)} \tag{2.27}$$

The parameters A and n represent the creep coefficient and creep exponent, respectively. In this study, variations in these parameters for each constituent material are employed to further understand their effect on the material response as well as on the overall structural response in the context of the modeled RLV thrust cell liner.

Power-law creep model coefficients for the NARloy-Z and OFHC copper were determined by curve fitting the stress–strain data of Esposito and Zabora (1975) to a number of predetermined creep exponents over an applicable range of temperatures. This curve fitting was accomplished through the application MCCM. Given a specific strain rate and a sequence of creep exponents, the model was employed to determine a set of creep coefficients and exponents that produced stress-strain data matching the above constant strain-rate experimental stress-strain data. Similarly, matched pairs of creep coefficients and exponents were determined for NiCrAlY using ultimate tensile strength and yield strength data obtained from Deevi and Sikka (1996). The material thermoelastic and creep parameters that govern the response of the individual liner constituents are presented in Tables 2.8 – 2.10.

NARloy-Z Characterization

Table 2.8 presents the thermoelastic parameters as well as the power-law creep coefficients and exponents as functions of temperature for NARloy-Z. The data are arranged according to small, intermediate and large creep exponents to be employed in the HOTCFGM analysis. Figure 2.12 presents comparison of the experimental stress-strain data with the predicted constant strain-rate, stress-strain response for this alloy based on the small, intermediate and large power-law creep exponents. Several interesting results can be observed in this figure. First, the limiting power-law stress-strain response does not admit strain hardening and thus does not match the experimental data as precisely as Robinson's model (see Figure 2.10). Second, increasing the creep exponent and subsequently decreasing the creep coefficient, while maintaining a constant strain-rate of 1% per minute, to produce approximately equivalent stress-strain response in the limit, results in a sharper elastic-to-inelastic regime transition.

Table 2.8. Thermo-elastic and creep material parameters for NARloy-Z

E (GPa)	υ	α (10^{-6}/°C)	n (small)	n (intermediate)	n (large)
147	0.34	17.85	1.2	2.75	4.0

Temp (°C)	A (small) (MPa^{-n}/s)	A (intermediate) (MPa^{-n}/s)	A (large) (MPa^{-n}/s)
-245	2.236E-07	4.444E-11	4.500E-14
21	2.589E-07	6.111E-11	7.222E-14
260	3.194E-07	9.722E-11	1.444E-13
538	4.792E-07	2.500E-10	5.625E-13

Table 2.9. Thermoelastic and creep material parameters for OFHC copper

E (GPa)	υ	α (10^{-6}/°C)	n (small)	n (intermediate)	n (large)
114	0.33	17.20	1.2	3.0	4.5

Temp (°C)	A (small) (MPa^{-n}/s)	A (intermediate) (MPa^{-n}/s)	A (large) (MPa^{-n}/s)
-245	1.014E-06	4.861E-10	8.333E-13
21	1.146E-06	6.528E-10	1.278E-12
260	1.347E-06	9.861E-10	2.389E-12
538	1.944E-06	2.431E-09	9.167E-12

Table 2.10. Thermoelastic and creep material parameters for NiCrAlY

E (GPa)	ν	α (10^{-6}/°C)	n (small)	n (intermediate and large)
156	0.27	13.4	1.2	2.25

Temp (°C)	A (small) (MPa^{-n}/s)	A (intermediate and large) (MPa^{-n}/s)
-245	7.778E-08	9.306E-11
21	9.444E-08	1.375E-10
260	2.139E-07	6.250E-10
538	1.389E-06	2.083E-08

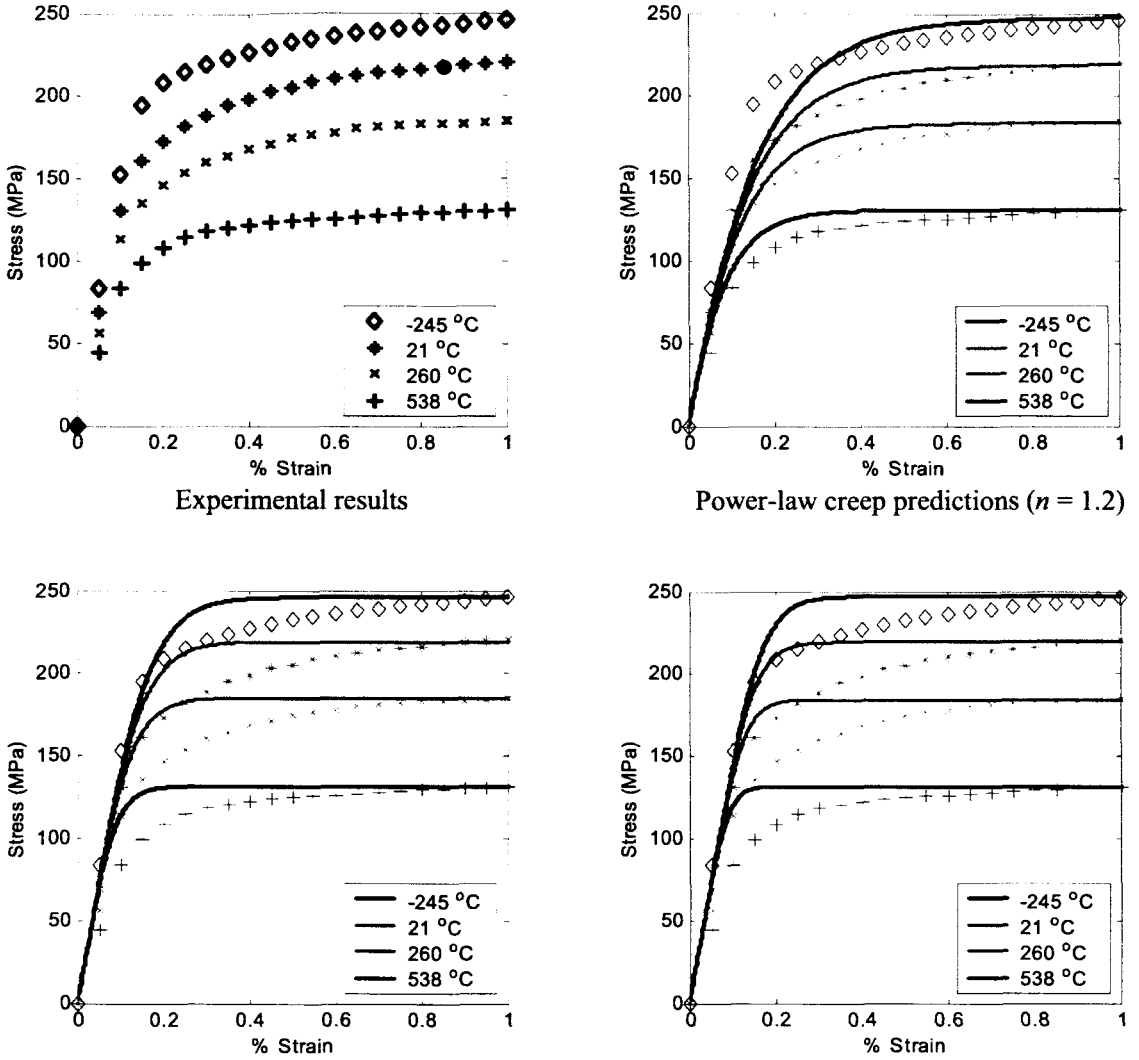

Figure 2.12. NARloy-Z stress-strain data at different temperatures after Esposito and Zabora (1975) (top left) and predicted stress-strain response of NARloy-Z by temperature using creep parameters for $n = 1.2$ (top right), $n = 2.75$ (bottom left) and $n = 4.0$ (bottom right).

Figures 2.13 and 2.14 demonstrate the dramatic influence that the power-law creep parameters A and n have on creep and stress relaxation responses at the two extreme temperatures. As in the case of the Robinson model results presented earlier, all results are shown over a 500-second time interval with the constant applied stress of 25, 50 and 100 MPa for the creep tests and the same initial stress levels for the relaxation tests. In contrast to the Robinson model, the creep response predicted by the employed power-law creep model, Eq. (2.26), is linear with time for all stress levels, as also observed in the plots. Additionally, decreasing the creep exponent and increasing the creep coefficient in the manner described in the foregoing results in more creep strain accumulation during the simulated 500-second test at a given temperature for the employed range of stresses. This outcome is an artifact of the curve fitting process.

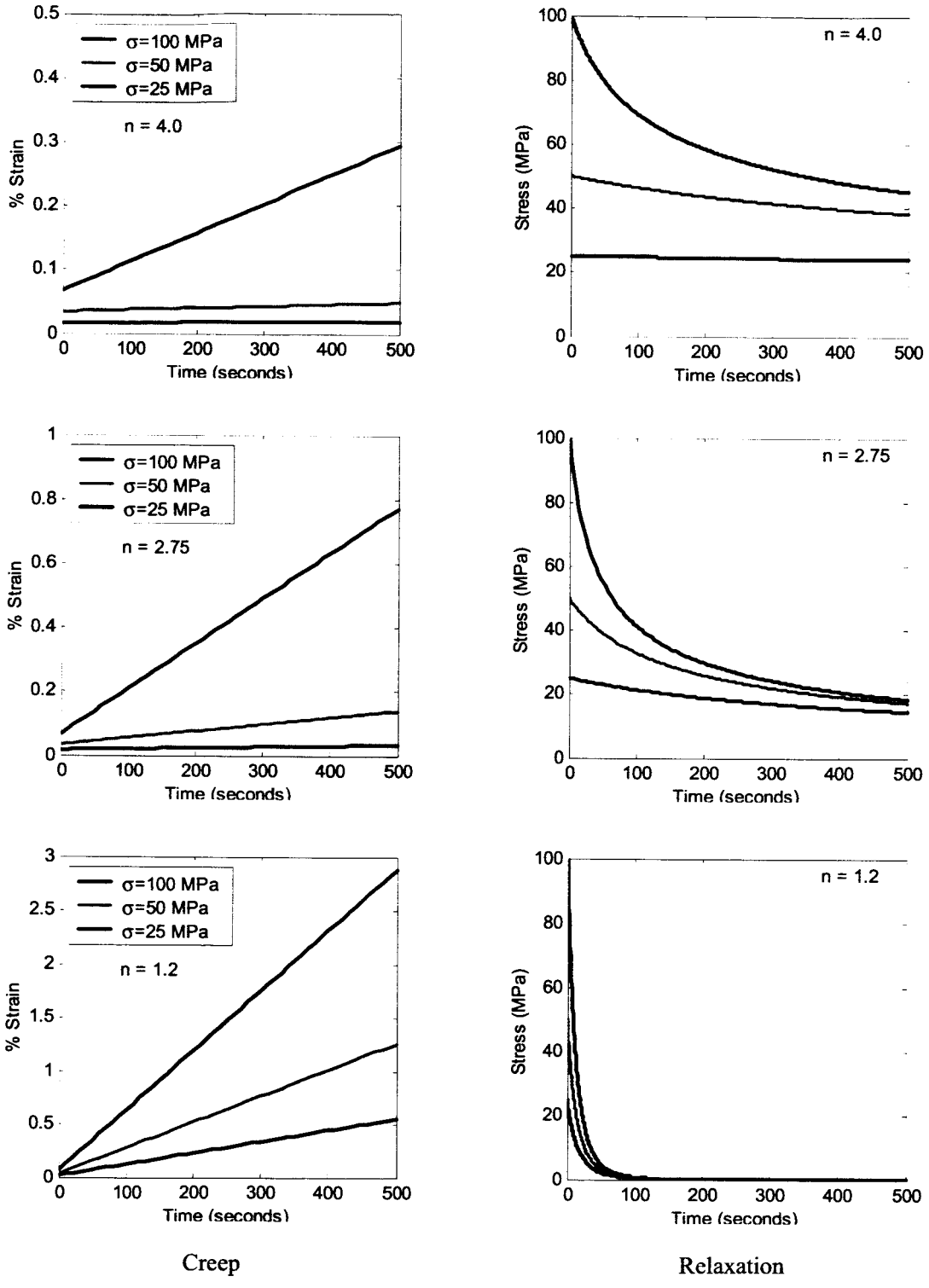

Figure 2.13. The effect of the power-law creep exponent on creep and relaxation response of NARloy-Z at -245 °C (note the different scales for the creep curves).

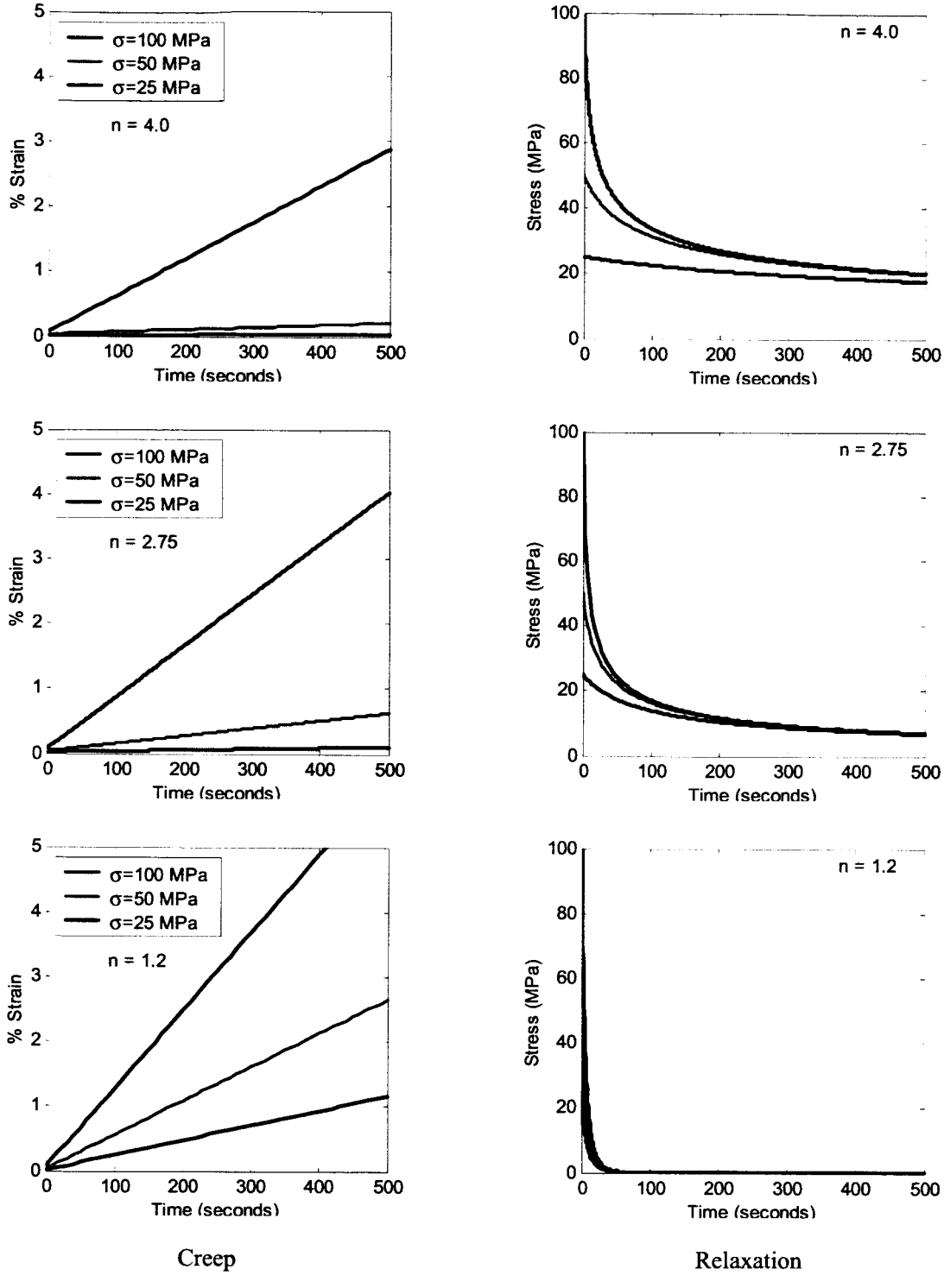

Figure 2.14. The effect of the power-law creep exponent on creep and relaxation response of NARloy-Z at 538 °C.

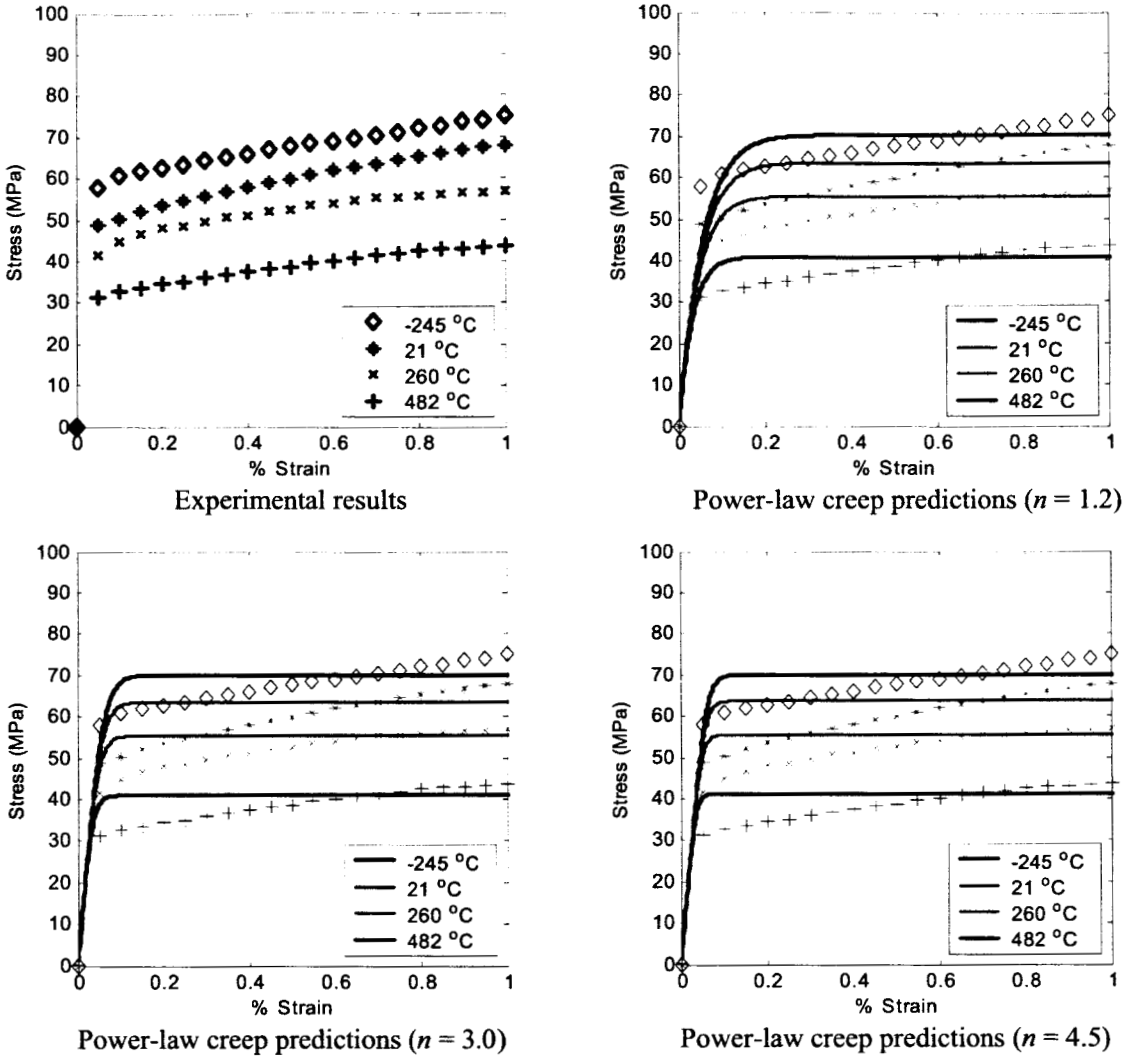

Figure 2.15. OFHC copper stress-strain data at different temperatures after Esposito and Zabora (1975) (top left) and predicted stress-strain response of OFHC copper by temperature using creep parameters for $n = 1.2$ (top right), $n = 3.0$ (bottom left) and $n = 4.5$ (bottom right).

The relaxation results can be observed to approach a zero stress state more rapidly as the creep exponent approaches 1.0. This result follows the general form of the characteristic relaxation equation given by

$$\text{for } n>1: \ \sigma(t)=[\sigma_0^{(1-n)}+(n-1)EAt]^{\frac{1}{1-n}} \tag{2.28}$$

$$\text{for } n=1: \ \sigma(t)=\sigma_0 e^{-EAt} \tag{2.29}$$

Comparison of the predicted power-law model creep and relaxation results of Figures 2.13 and 2.14 with the corresponding Robinson model results shown in Figure 2.11 reveals that the closest match between the two sets of model predictions occurs for the large creep exponent. This comes as no surprise given

that experimental creep tests conducted by Lewis (1970) revealed the slope of the steady-state creep curve to be 4.0 for NARloy-Z. This does show, however, that experimental characterization of Robinson model parameters and power-law creep model parameters produce similar but not identical results under creep and relaxation loading. Alternatively, the best fit between the two model predictions under constant strain-rate loading occurs when the creep exponent is small. Comparison of results in the context of the full structural analysis of the NARloy-Z trust cell liner is presented in Section 3.

OFHC Copper Characterization

Power-law creep coefficients and exponents as well as thermoelastic parameters for OFHC copper are shown in Table 2.9 as functions of temperature. Figure 2.15 presents comparison of the experimental stress-strain data from Esposito and Zabora with the predicted power-law constant strain rate, stress-strain response for OFHC copper based on the small, intermediate and large creep exponents. The same trends observed in the NARloy-Z figures are also seen in the OFHC copper results although in this case it is not possible to compare these results to the Robinson model. In the creep and relaxation tests shown in Figures 2.16 and 2.17, much smaller stresses are employed than were previously employed in the NARloy-Z tests due to the differences in load-bearing capability of the two materials.

NiCrAlY Characterization

Power-law creep coefficients and exponents as well as thermoelastic parameters for NiCrAlY are shown in Table 2.10 as functions of temperature. Once again, the data are arranged according to small and intermediate creep exponents. Figure 2.18 presents comparison of the experimental stress-strain data derived from yield and ultimate tensile strengths provided by Deevi and Sikka (1996) with the predicted power-law constant strain rate stress-strain response for NiCrAlY based on the small and intermediate creep exponents. The same trends observed in the NARloy-Z and OFHC copper figures can also be seen in the NiCrAlY results. Unlike the NARloy-Z and OFHC copper creep and relaxation tests, larger stresses are employed as a result of the relatively high strength of NiCrAlY, particularly as compared to OFHC copper, Figures 19 and 20. In the case when the creep exponent of NiCrAlY is 2.25, comparison can be made with the experimental data of Brindley and Whittenberger (1992). Figure 2.21 shows the predicted power-law creep model relaxation in comparison to the experimental results produced by Brindley and Whittenberger at 900 °C. Since the "intermediate" exponent is the best fit to the data available, the "large" exponent is eliminated in this case.

2.4.3 Summary of Model Responses

The Robinson and power-law creep models are shown to predict similar constant strain-rate stress-strain response for a variety of power-law creep parameters fitted to experimental data. The power-law creep model employed in this study, however, does not admit strain-hardening in contrast to the Robinson model. Short-term creep response of the two models is shown to differ substantially at large stress levels. By its nature the power-law creep model produces a linear creep curve with time for all stress levels, while the Robinson model produces a very nonlinear creep curve for large stresses in a short time frame (< 100 seconds). At the end of the employed 500 second loading history, however, the Robinson model predicts approximately the same magnitude of creep strain as the power-law creep model when the experimentally characterized material parameters are used for each model. Additionally, the Robinson model produces much more rapid stress relaxation than the power-law creep model in a short time frame. In the long-term, however, the two models again predict approximately the same stress relaxation in the considered time interval of 500 seconds when the experimentally characterized material parameters are used for each model.

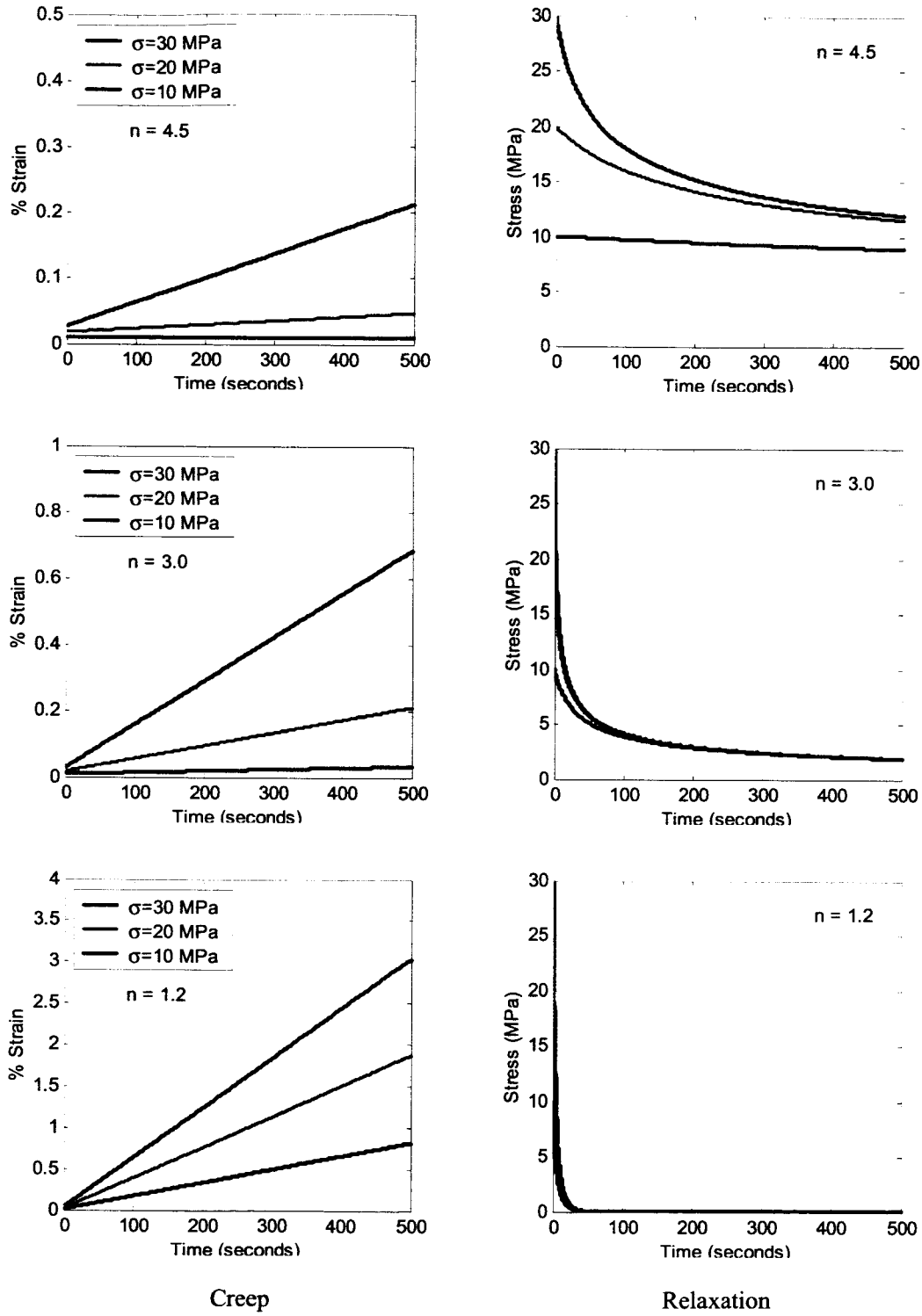

Figure 2.16. The effect of the power-law creep exponent on creep and relaxation response of OFHC copper at -245 °C.

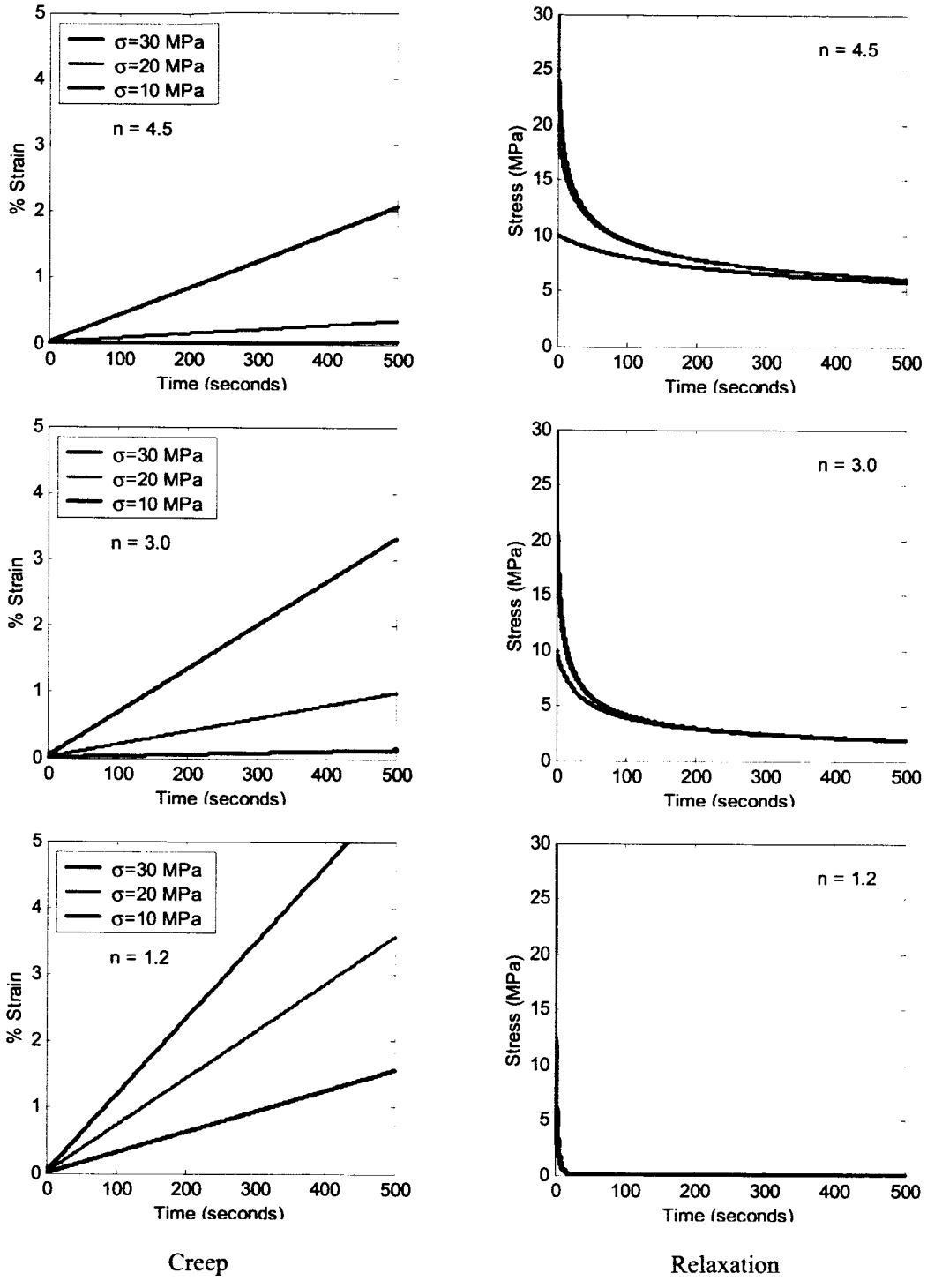

Figure 2.17. The effect of the power-law creep exponent on creep and relaxation response of OFHC copper at 538 °C.

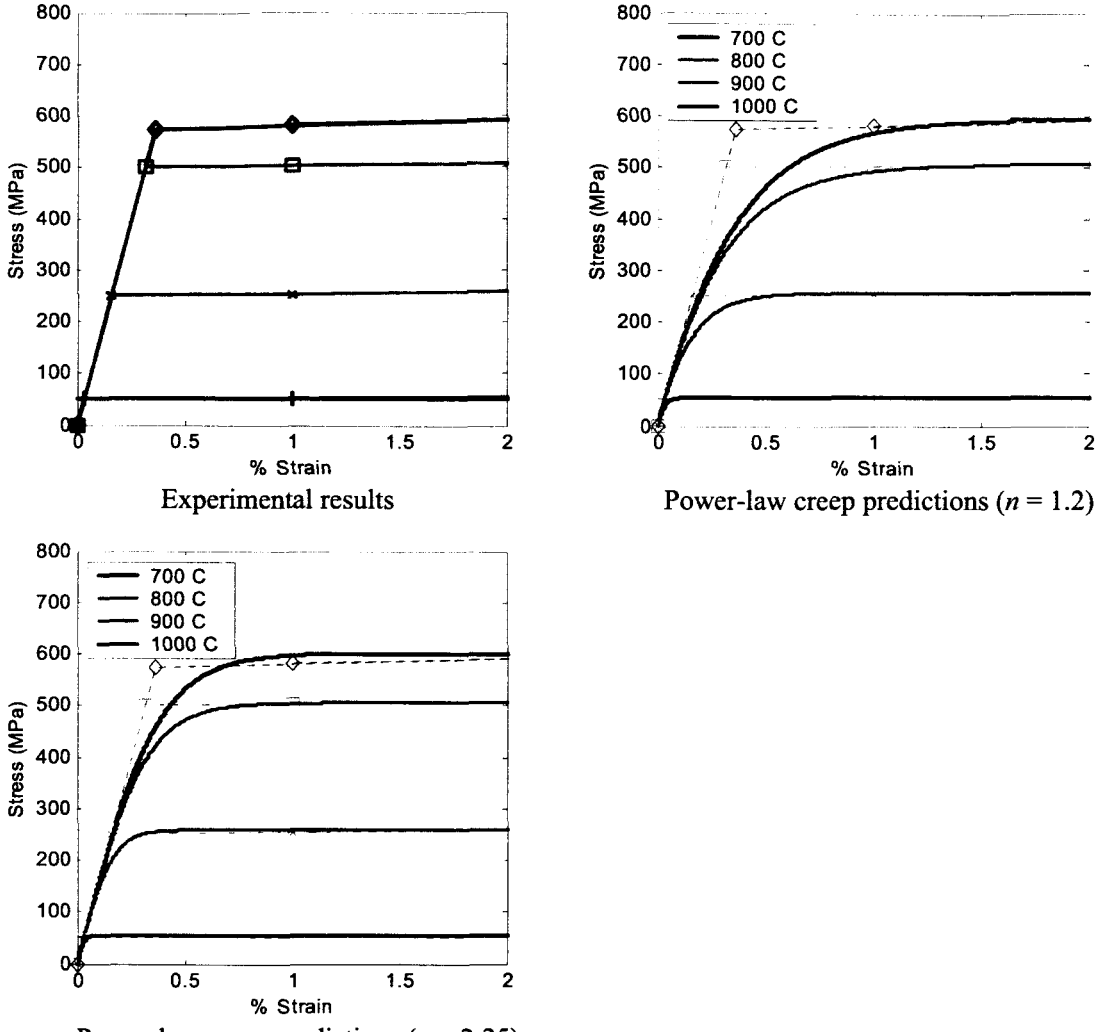

Experimental results

Power-law creep predictions ($n = 1.2$)

Power-law creep predictions ($n = 2.25$)

Figure 2.18. NiCrAlY stress-strain data at different temperatures, as interpolated from Deevi and Sikka (1996) (top left) and predicted stress-strain response of NiCrAlY by temperature using creep parameters for $n = 1.2$ (top right) and $n = 2.25$ (bottom left).

3 Modeling the Dog-House Effect: Relation to Previous Work

Four specific goals motivate the work of this section. First, we investigate the predictive capabilities of HOTCFGM by comparing deformations predicted by an analysis employing Robinson's model to the deformation results presented by Arya and Arnold for the same NARloy-Z thrust cell liner and loading history. Second, the deformations predicted by the more efficient power-law creep model are compared to the results of Arya and Arnold as well as the HOTCFGM analysis based on the more computationally demanding Robinson model. Third, the assertion of Arya and Arnold that "dog-house" type deformation is driven, in part, by a biasing pressure differential across the cooling channel wall is also examined by performing an analysis of a NARloy-Z thrust cell liner in the absence of applied pressures in the cooling channel and the combustion chamber. Fourth, the Robinson and power-law creep models are compared

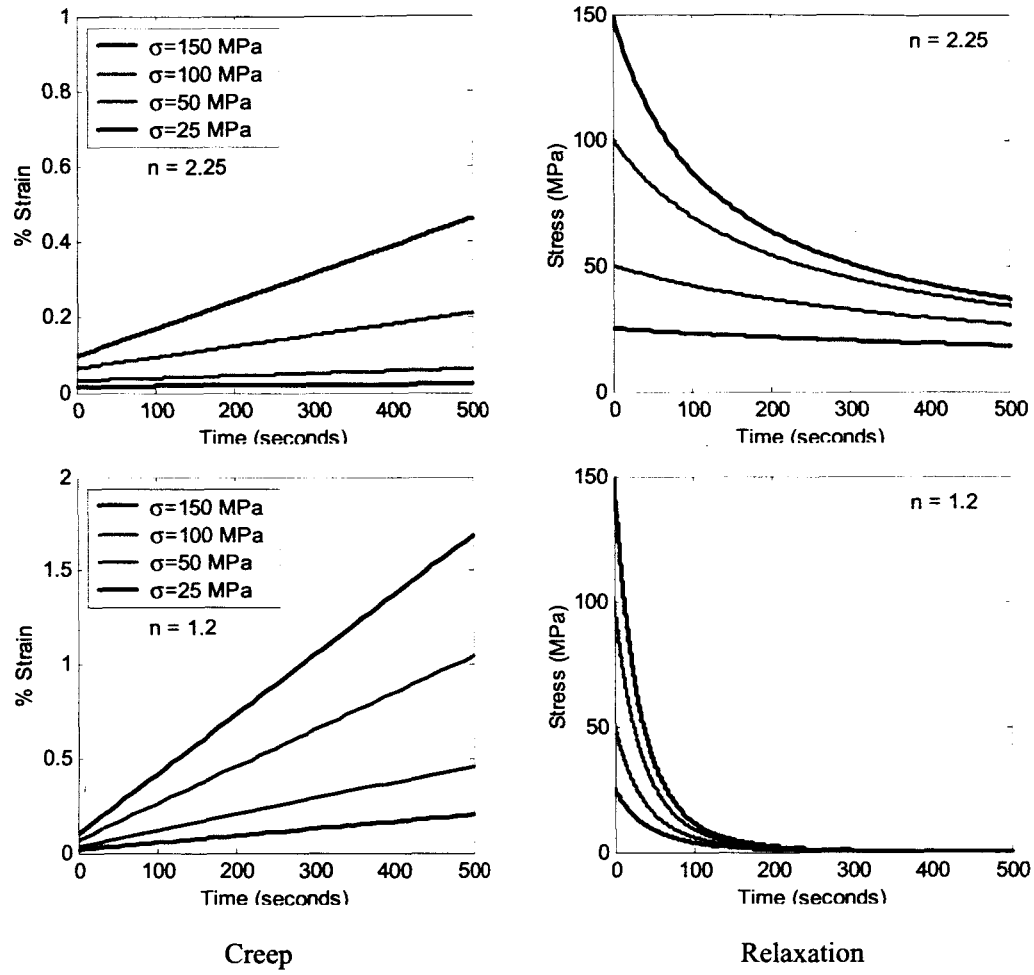

Figure 2.19. The effect of the power-law creep exponent on creep and relaxation of NiCrAlY at 700 °C.

on the basis of a single 500-second cycle that is more consistent with the actual space shuttle main engine cycle. Together these four comparisons establish the connection between the Robinson and power-law creep models and the experimental data, and set the stage for the parametric studies of Section 5.

3.1 Investigating the Predictive Capabilities of HOTCFGM-2D

First, we compare the HOTCFGM-predicted deformations to those of Arya and Arnold generated using the finite element code MARC based on the Robinson model for the NARloy-Z response in the context of multiple 3.5-second cycles. The predicted deformed shapes reported by Arya and Arnold show minimal quantitative detail, thus a closer analysis of the presented plots of radial displacements and change in radial thickness at key points around the cooling channel wall is needed.

In their work, Arya and Arnold (1991, Figure 15) present a time history of radial displacements for the point at which the left boundary and innermost radius of the thrust cell liner intersect as well as for the point at which the left boundary and innermost radius of the cooling channel intersect. The two points correspond to each side of the cooling channel wall at the circumferential centerline of the actual cooling

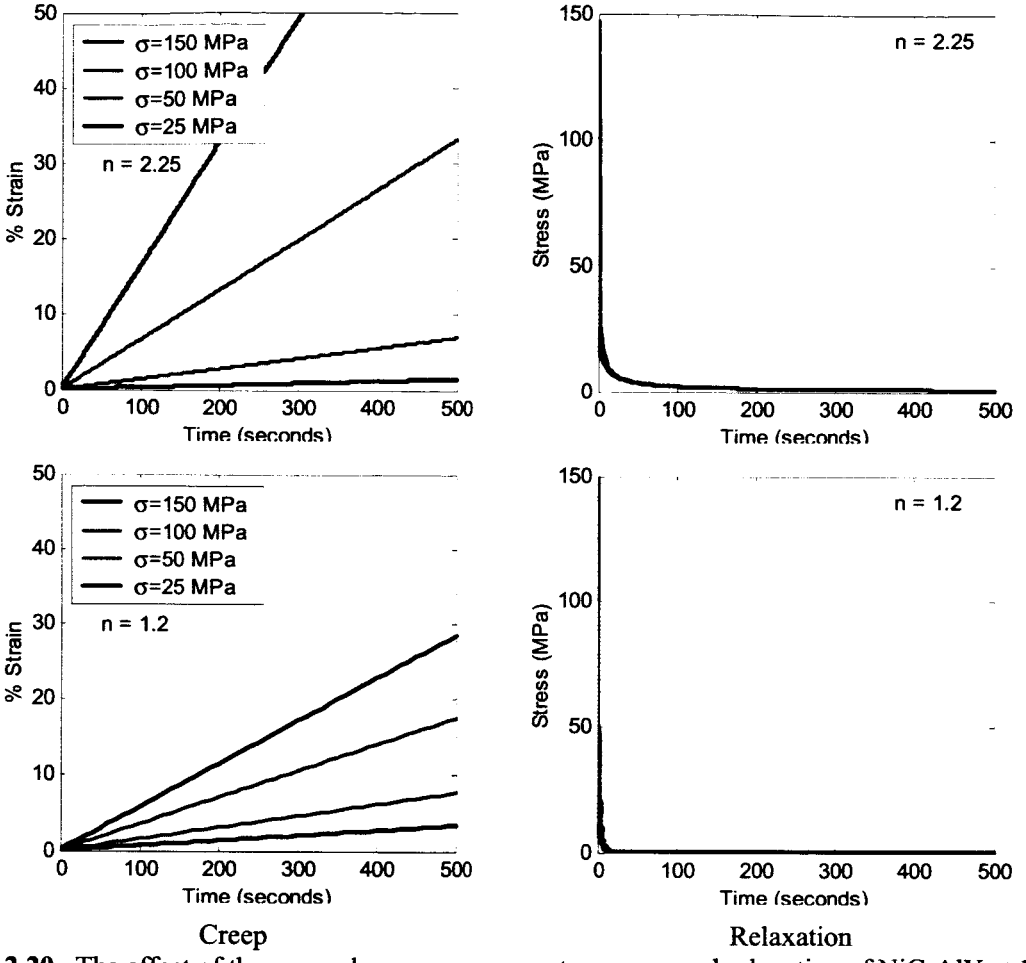

Figure 2.20. The effect of the power-law creep exponent on creep and relaxation of NiCrAlY at 1000 °C.

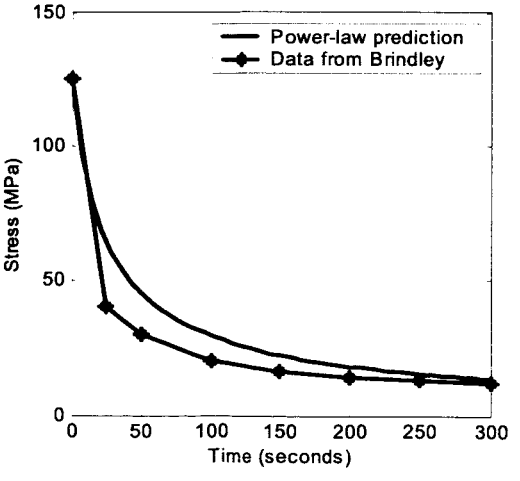

Figure 2.21. Comparison of power-law predicted relaxation (n = 2.25) and experimental data for NiCrAlY at 900 °C.

channel or the radial line of symmetry in the case of the cross sectional model. Arya and Arnold have denoted these points A and B, respectively (see Figure 3.1). Their results demonstrate that the radial displacement, or bulging in the direction of the combustion chamber, at points A and B continually increases with the number of cycles or time. Furthermore, the authors show that the inward radial displacement of point A is greater than that of point B, signifying a corresponding change in cooling channel wall thickness as cycles are accumulated. The authors, however, ignore the direction of this change in wall thickness and mistakenly label cooling *channel wall thickening* as cooling channel wall *thinning*, since in fact, after a number of cycles, point A is actually at a greater distance from point B than in the original state. In contrast to the predicted bulging, such thickening of the cooling channel wall along this radial line of symmetry is not characteristic of the experimentally observed "dog-house" type of failure. This is the first issue addressed in the following section using HOTCFGM.

3.2 HOTCFGM Short Cycle Results

Robinson Model Results with Applied Pressures

Deformed shapes predicted by HOTCFGM analysis based on Robinson's model and multiple 3.5-second cycles are shown in Figure 3.1. The predicted contraction of the thrust cell liner's cross section contrasts with the results presented by Arya and Arnold which predict a bulging out of the overall cross section. Despite the overall contraction of the cross section, relative bulging of the cooling channel wall is, however, predicted by the HOTCFGM analysis, as the lower left edge of the cross section has not contracted to the same extent as the lower right edge of the cross section, thereby producing a general rotation of the bottom surface.

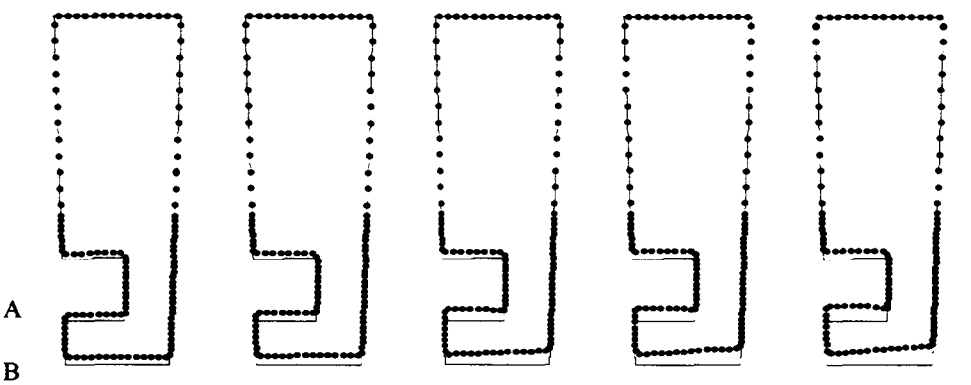

Figure 3.1. Predicted deformed shapes of NARloy-Z thrust cell liner cross sections after 1, 10, 20, 25 and 30 3.5-second cycles using Robinson's model. Solid lines show undeformed shapes. Dotted lines show deformed shapes with all deformations magnified 5 times.

The trends with regard to the cooling channel wall thickness agree with those presented in Figure 15 of the work by Arya and Arnold as the cooling channel wall thickens with increasing cycles at the leftmost boundary of the cross sectional liner. Figure 3.2 shows the predicted cooling channel wall thickness as a function of circumferential position as well as number of cycles and serves to further demonstrate the trend of wall thickening as might be deduced from inverting Figure 16 in Arya and Arnold's report. Subsequently, Figure 3.3 illustrates the change in the cooling channel wall thickness as a function of the number of cycles, at both the left and right edges of the cooling channel cross section. The

model predicts that the thickness of the cooling channel wall at the left edge of the cross section increases radially along the line of symmetry (denoted by a positive change in wall thickness), while at the right edge it decreases in the radial direction (denoted by a negative change in wall thickness). *As in the results of Arya and Arnold, the Robinson model fails to simultaneously replicate the experimentally observed bulging and thinning of the cooling channel wall in the region of the failure site shown earlier in Figure 1.6.*

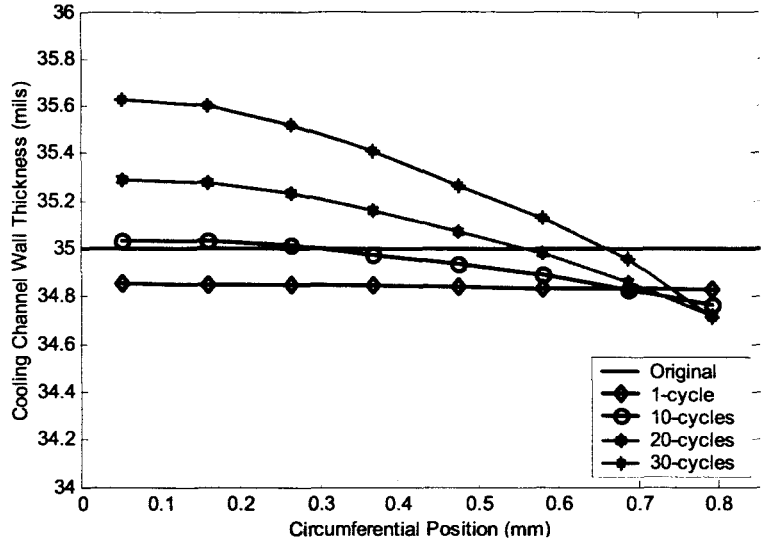

Figure 3.2. Predicted cooling channel wall thickness as a function of circumferential position and number of cycles for multiple 3.5-second cycle analysis of NARloy-Z liner using Robinson's model.

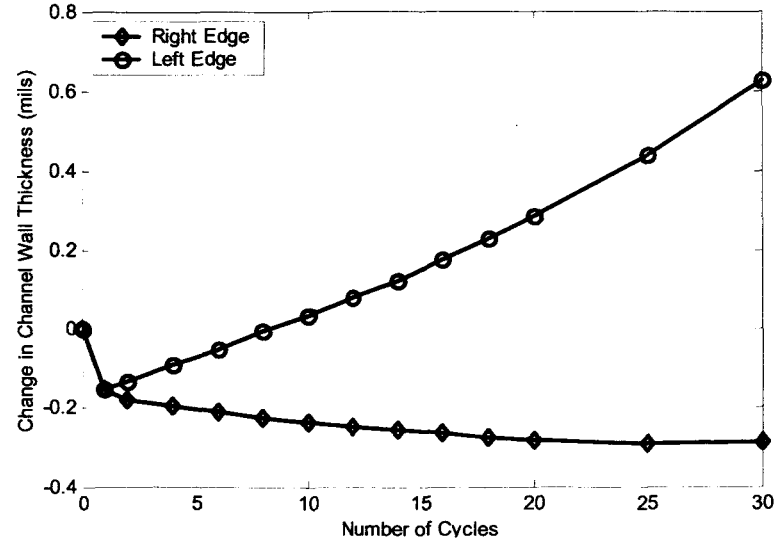

Figure 3.3. Predicted changes in cooling channel wall thickness at the left and right edges of the cooling channel for multiple 3.5-second cycle analysis of NARloy-Z liner using Robinson's model.

Power-Law Creep Model Results with Applied Pressures

Figure 3.4 presents the deformed shapes predicted by HOTCFGM analysis based on the power-law creep model and the multiple 3.5-second cycles employed by Arya and Arnold. The power-law coefficients and exponents of NARloy-Z shown in Section 2 to produce the creep and relaxation response closest to the response characterized by the Robinson parameters are employed in this analysis. Specifically, the large creep exponent ($n = 4.0$) and the corresponding creep coefficients are employed. In this case, bulging and thinning of the cooling channel wall is readily apparent as *the power-law creep model appears to more closely match the experimentally observed deformations of such thrust cell liners.* In support, Figure 3.5 shows the predicted cooling channel wall thinning across the entire circumference of the cooling channel wall as cycles are accumulated. This is in contrast to the Robinson model result shown in Figure 3.2 in which only a portion of the cooling channel wall near the right edge of the cooling channel was shown to thin as cycles are accumulated. In Figure 3.6, the change of the cooling channel wall thickness is plotted versus the number of cycles to show that despite continued bulging of the left edge of the cooling channel

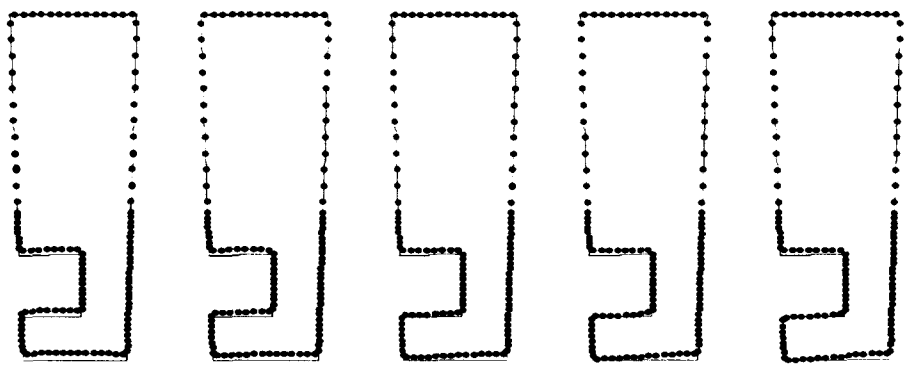

Figure 3.4. Predicted deformed shapes of NARloy-Z thrust cell liner cross sections after 1, 10, 20, 25 and 30 3.5-second cycles using the power-law creep model. Solid lines show undeformed shapes. Dotted lines show deformed shapes with all deformations magnified 5 times.

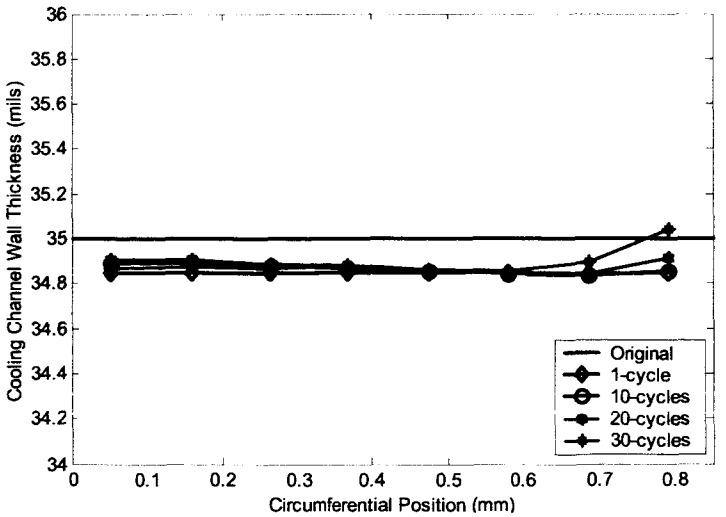

Figure 3.5. Predicted cooling channel wall thickness as a function of circumferential position and cycle number for multiple 3.5-second cycle analysis of NARloy-Z liner using the power-law creep model.

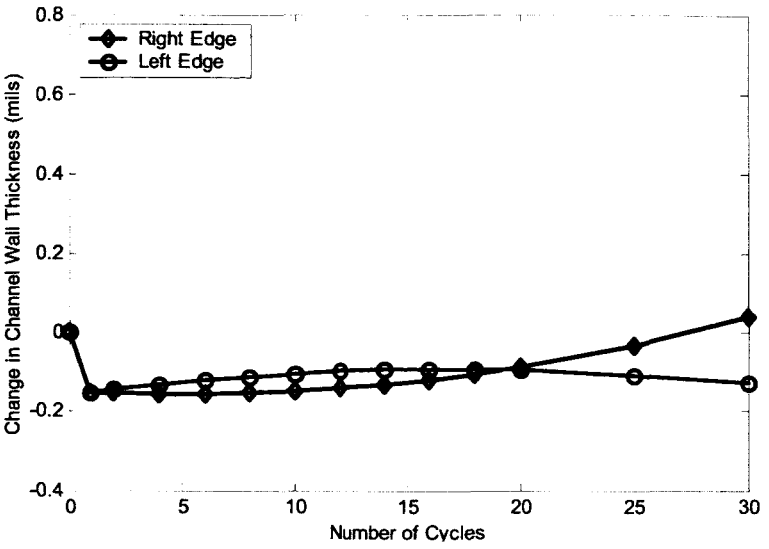

Figure 3.6. Predicted changes in cooling channel wall thickness at the left and right edges of the cooling channel for multiple 3.5-second cycle analysis of NARloy-Z liner the power-law creep model.

wall with additional cycles the cooling channel wall thickness at the left edge actually increases slightly until approximately 15 cycles are accumulated. At this point, the left edge of cooling channel wall again begins to exhibit progressive thinning. On the other hand, the right edge of the cooling channel wall thins initially and remains relatively constant before progressive thickening of the wall in this region occurs, thereby reversing the effect of the initial thinning by the time 30 cycles have accumulated. In addition to capturing the experimentally observed behavior of the thrust cell liner more accurately than the Robinson model, the power-law creep model execution time is approximately ¼ that of the Robinson model.

Power-Law Creep Model Results without Applied Pressures

A further investigation of the argument by Arya and Arnold that the "dog-house" effect was caused, at least in part, by the biasing pressure differential across the cooling channel wall was conducted by analyzing the previous case in the absence of applied pressures in the cooling channel and the combustion chamber. Figure 3.7 presents the deformed shapes predicted by HOTCFGM analysis based on the power-law creep model and the multiple 3.5-second cycles employed by Arya and Arnold in the absence of applied pressures. Comparing the results of Figure 3.4 and Figure 3.7, the effects of pressure are distinctly clear. In contrast to Figure 3.4, which demonstrates both bulging and thinning of the cooling channel wall, Figure 3.7 shows only bulging much like the Robinson analysis results in Figure 3.1. This result indicates that the pressure differential from the cooling channel to the combustion chamber does promote thinning of the cooling channel wall.

Figures 3.8 and 3.9 further demonstrate how closely the power-law creep results in the absence of pressure mirror the results of the Robinson analysis, as predicted cooling channel wall thicknesses are very similar in the two analyses (see also Figures 3.1 and 3.2). These similarities are explained, in part, by recalling the relaxation response predicted by the Robinson and power-law creep models based on the NARloy-Z characterization. Figures 2.11 and 2.14, for example, illustrate that in a very short time range the Robinson model predicts much more rapid stress relaxation than the power-law creep model for the same temperature and initial stress level. Due to this rapid stress relaxation exhibited by the Robinson

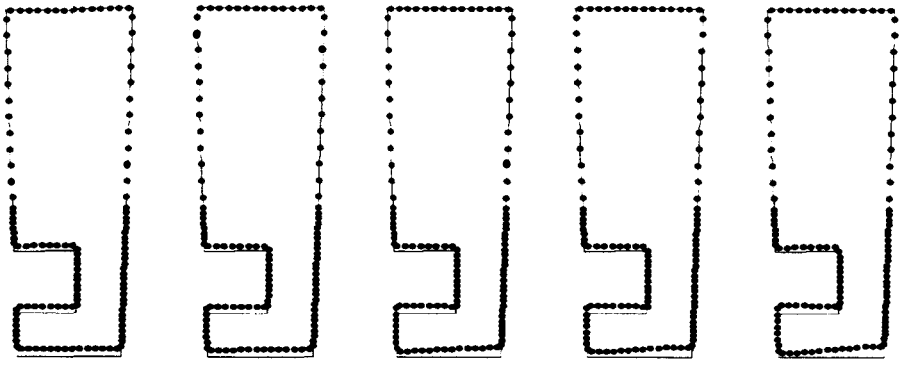

Figure 3.7. Predicted deformed shapes of NARloy-Z thrust cell liner cross sections after 1, 10, 20, 25 and 30 3.5-second cycles using the power-law creep model in the absence of applied pressures. Solid lines show undeformed shapes. Dotted lines show deformed shapes with deformations magnified 5 times.

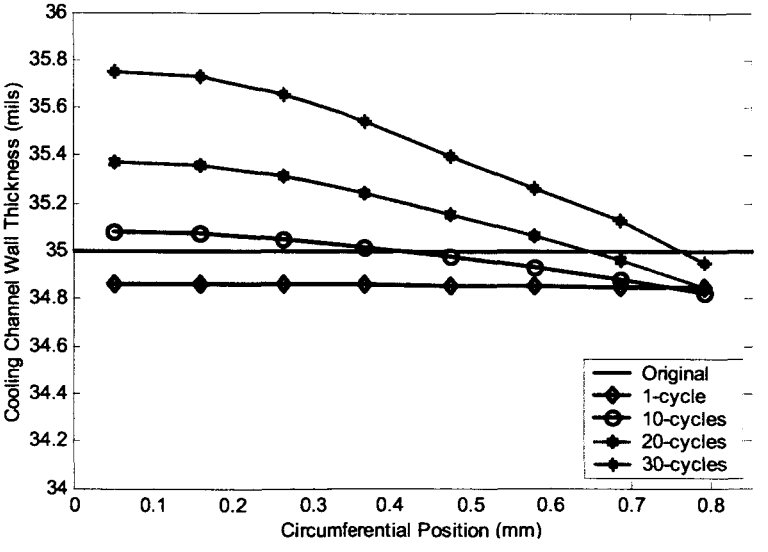

Figure 3.8. Predicted cooling channel wall thickness as a function of circumferential position and number of cycles for multiple 3.5-second cycle analysis of NARloy-Z liner using the power-law creep model in the absence of applied pressures.

model, the two models *do not* predict the same effective stresses or creep strains in the context of the full structural analyses. Thus the rapid relaxation predicted by the Robinson model reduces stresses to such an extent that the creep-induced deformations are substantially reduced.

The multiple short-cycle cases have been shown to be an effective means to gain some understanding of the material parameters that influence thrust cell liner durability. The goal of simulating as closely as possible the true space shuttle main engine cycle, however, requires the use of a much longer cycle, particularly in light of the fact that the creep/relaxation behavior in a very short cycle is much different from that of an extended cycle. Thus we turn to a comparison of the 500-second cycle results for the Robinson and power-law creep models.

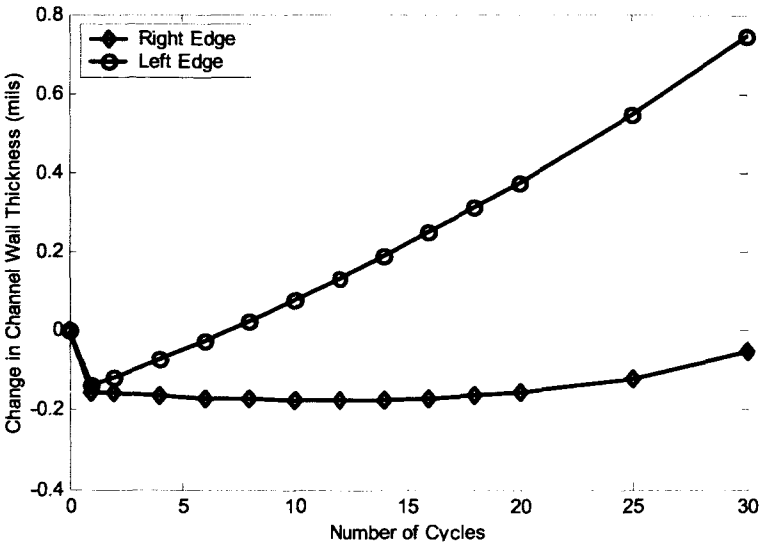

Figure 3.9. Predicted changes in cooling channel wall thickness at the left and right edges of the cooling channel for multiple 3.5-second cycle analysis of NARloy-Z liner the power-law creep model in the absence of applied pressures.

3.3 HOTCFGM Long Cycle Results

Employing the Robinson and the power-law creep models in conjunction with HOTCFGM to analyze a NARloy-Z thrust liner over a single 500-second cycle provides for a direct comparison of the two models over a timeframe on the order of the actual space shuttle main engine cycle. As in the multiple 3.5-second cycle case, the NARloy-Z power-law creep coefficients and exponents producing the response most similar to the Robinson model predicted response of NARloy-Z are selected. Figures 3.10 and 3.11 show the predicted deformations of the NARloy-Z thrust cell liner as a function of time for the Robinson and power-law creep models, respectively. The two sequences of deformations are practically indistinguishable, demonstrating that both models predict nearly the same deformation during a single 500-second cycle. Due to its efficiency, however, the power-law creep model required approximately only ¼ of the execution time needed by the Robinson model.

Additionally, these results demonstrate that conducting parametric studies with the intent of mitigating deformations after a single 500-second cycle is not feasible for these material parameters, given the virtual lack of predicted end-of-cycle deformation seen in Figures 3.10 and 3.11. Multiple long cycle results (not shown) have produced deformations similar to those observed after many short cycles. A single 500-second HOTCFGM analysis employing the power-law creep model and the level of mesh discretization described in Section 2 requires approximately 2 ½ to 3 days of execution time, thus making the use of multiple long cycles not feasible in the context of a parametric study which involves variation of many parameters. Utilization of the Robinson model for such analyses borders on intractability as execution times for each analysis would be on the order of 10 to 12 days. However, since the objectives of this study necessitate efficient predictions of deformations that can be reduced or eliminated through changes in geometry or the application of thermal barrier coating systems, the creep coefficients employed in the parametric studies of Section 5 were magnified by a factor of 10. By increasing the creep coefficient of each constituent material presented in Section 2 by a factor of 10 the creep rate is also increased by the same factor, and thus the creep strain observed in the same time period will also be increased by a factor of 10. Similarly, such increase in the creep coefficient also produces a more rapid

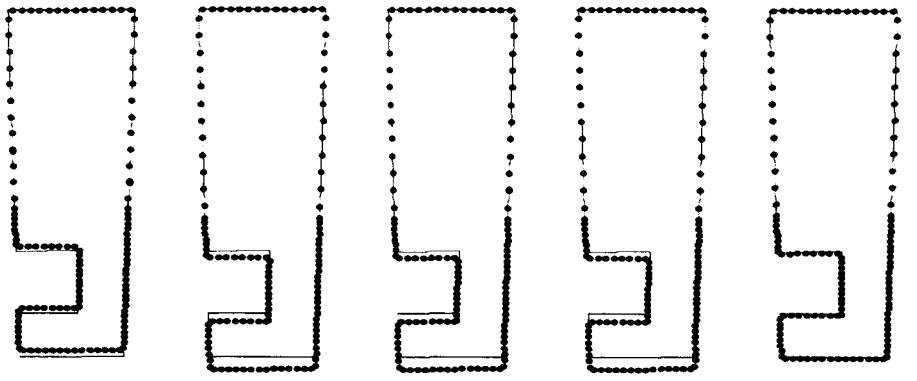

Figure 3.10. Predicted deformed shapes of NARloy-Z thrust cell liner cross sections at five times during the extended thermal cycle, t = 1.0, 100, 200, 400 and 500 seconds using Robinson's model. Solid lines show undeformed shapes. Dotted lines show deformed shapes with all deformations magnified 5 times.

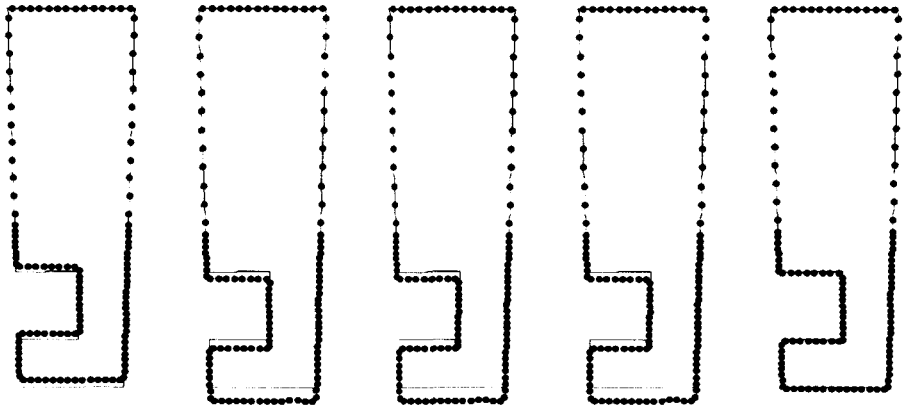

Figure 3.11. Predicted deformed shapes of NARloy-Z thrust cell liner cross sections at five times during the extended thermal cycle, t = 1.0, 100, 200, 400 and 500 seconds using the power-law creep model. Solid lines show undeformed shapes. Dotted lines show deformed shapes with all deformations magnified 5 times.

stress relaxation rate. The constant strain-rate stress-strain response, however, is unchanged as the straining rate employed in the curve fitting procedure was increased by 10 times in order to offset the increased creep coefficient and maintain consistent stress-strain response. Such modifications to the constituent materials' overall response are analogous to accelerated testing methods in which tests are conducted at temperatures beyond which material or structural response is sought with the intention of performing the test more rapidly (i.e. utilization of the time-temperature equivalence). Hence, the results presented in Section 5 have been generated using these higher creep rates in the context of an accelerated modeling procedure. As will be shown, this accelerated modeling procedure preserves the accuracy required to capture the relative effects while providing a level of computational efficiency consistent with design-related parametric studies.

4 Homogenization of Graded Coatings via GMC-3D

In this section, a method of determining the effective properties for the graded layers to be employed in the analysis of functionally graded coating systems is outlined and then utilized. The method, known as the Generalized Method of Cells (GMC), is employed to determine the effective response of the homogenized graded regions for use in the HOTCFGM analysis in Section 5.

4.1 GMC-3D: An Overview

GMC is a micromechanics model developed by Paley and Aboudi (1992) to predict the response of multiphase composites. The model evolved from the method of cells, Aboudi (1991), and in recent years a number of versions and modifications, a reformulation and a user-friendly-interface called MAC/GMC, Bednarcyk and Arnold (2002), developed by the NASA-Glenn Research Center and the Ohio Aerospace Institute have resulted. One such version of the method is called GMC-3D, which is used to model triply-periodic composites characterized by a basic building block which repeats itself in three dimensions, thereby resulting in a three-dimensional periodic microstructure. To mimic the internal microstructure of a triply-periodic material, the repeating unit cell (RUC) is discretized into $N_\alpha, N_\beta, N_\gamma$ subcells of dimensions $d_\alpha, h_\beta, l_\gamma$. A summary of the model formulation is provided below following Aboudi (1995).

The displacement field within each subcell $(\alpha\beta\gamma)$ is approximated by the first-order expansion

$$u_i^{(\alpha\beta\gamma)} = w_i^{(\alpha\beta\gamma)}(\mathbf{x}) + \bar{x}_1^{(\alpha)}\varphi_i^{(\alpha\beta\gamma)} + \bar{x}_2^{(\beta)}\chi_i^{(\alpha\beta\gamma)} + \bar{x}_3^{(\gamma)}\psi_i^{(\alpha\beta\gamma)} \qquad i = 1,2,3 \tag{4.1}$$

where $w_i^{(\alpha\beta\gamma)}(\mathbf{x})$ are the displacement components at the center of the subcell, and $\varphi_i^{(\alpha\beta\gamma)}$, $\chi_i^{(\alpha\beta\gamma)}$ and $\psi_i^{(\alpha\beta\gamma)}$ are the microvariables relating the displacement $u_i^{(\alpha\beta\gamma)}$ to the local coordinates $\bar{x}_1^{(\alpha)}$, $\bar{x}_2^{(\beta)}$, $\bar{x}_3^{(\gamma)}$. The strain components in each subcell are then given by the small strain tensor

$$\varepsilon_{ij}^{(\alpha\beta\gamma)} = \frac{1}{2}(\partial_i u_j^{(\alpha\beta\gamma)} + \partial_j u_i^{(\alpha\beta\gamma)}) \qquad i,j = 1,2,3 \tag{4.2}$$

where $\partial_1 = \partial/\partial\bar{x}_1^{(\alpha)}$, $\partial_2 = \partial/\partial\bar{x}_2^{(\beta)}$ and $\partial_3 = \partial/\partial\bar{x}_3^{(\gamma)}$.

The assumed linear displacement field ensures that the strains given by combining Eq. (4.1) and Eq. (4.2) are the average strain components in each subcell

$$\begin{aligned}
\bar{\varepsilon}_{11}^{(\alpha\beta\gamma)} &= \varphi_1^{(\alpha\beta\gamma)}, \\
\bar{\varepsilon}_{22}^{(\alpha\beta\gamma)} &= \chi_2^{(\alpha\beta\gamma)}, \\
\bar{\varepsilon}_{33}^{(\alpha\beta\gamma)} &= \psi_3^{(\alpha\beta\gamma)}, \\
2\bar{\varepsilon}_{23}^{(\alpha\beta\gamma)} &= \chi_3^{(\alpha\beta\gamma)} + \psi_2^{(\alpha\beta\gamma)}, \\
2\bar{\varepsilon}_{13}^{(\alpha\beta\gamma)} &= \psi_1^{(\alpha\beta\gamma)} + \varphi_3^{(\alpha\beta\gamma)}, \\
2\bar{\varepsilon}_{12}^{(\alpha\beta\gamma)} &= \chi_1^{(\alpha\beta\gamma)} + \varphi_2^{(\alpha\beta\gamma)}
\end{aligned} \tag{4.3}$$

The general constitutive equation for the material in $(\alpha\beta\gamma)$ subcell is then given in terms of the average stress, the elastic stiffness tensor, and the average total, inelastic and thermal strain quantities as follows,

$$\bar{\sigma}_{ij}^{(\alpha\beta\gamma)} = C_{ijkl}^{(\alpha\beta\gamma)}(\bar{\varepsilon}_{kl}^{(\alpha\beta\gamma)} - \bar{\varepsilon}_{kl}^{I(\alpha\beta\gamma)} - \bar{\varepsilon}_{kl}^{T(\alpha\beta\gamma)}) \tag{4.4}$$

where $\bar{\sigma}_{ij}^{(\alpha\beta\gamma)}$ is average subcell stress, $C_{ijkl}^{(\alpha\beta\gamma)}$ is the elastic stiffness tensor of the subcell material, $\bar{\varepsilon}_{kl}^{(\alpha\beta\gamma)}$ is the average total subcell strain, $\bar{\varepsilon}_{kl}^{I(\alpha\beta\gamma)}$ is the average inelastic subcell strain, and $\bar{\varepsilon}_{kl}^{T(\alpha\beta\gamma)}$ is the average thermal subcell strain given by $\bar{\varepsilon}_{kl}^{T(\alpha\beta\gamma)} = \alpha_{kl}^{(\alpha\beta\gamma)}\Delta T$. In this relation, $\alpha_{kl}^{(\alpha\beta\gamma)}$ is the coefficient of thermal expansion tensor and ΔT is the change in temperature relative to the reference temperature T_R.

Summing the weighted average stresses in each subcell and then dividing by the repeating unit cell volume gives the average stress in the composite.

$$\bar{\sigma}_{ij} = \frac{1}{dhl}\sum_{\alpha=1}^{N_\alpha}\sum_{\beta=1}^{N_\beta}\sum_{\gamma=1}^{N_\gamma} d_\alpha h_\beta l_\gamma \bar{\sigma}_{ij}^{(\alpha\beta\gamma)} \tag{4.5}$$

The next step is to relate the average subcell strains $\bar{\varepsilon}_{kl}^{(\alpha\beta\gamma)}$ appearing in Eq. (4.4) and thus Eq. (4.5) to the macroscopic or average strains $\bar{\varepsilon}_{ij}$ of the composite. To do this, the interfacial displacement continuity is first imposed in a surface-average sense followed by the application of periodicity conditions which ensure that the reference repeating unit cell is part of the entire triply-periodic array. This produces, after some lengthy algebraic manipulations, the following relations:

$$\sum_{\alpha=1}^{N_\alpha} d_\alpha \bar{\varepsilon}_{11}^{(\alpha\beta\gamma)} = d\bar{\varepsilon}_{11}, \qquad \beta = 1,\ldots,N_\beta, \quad \gamma = 1,\ldots,N_\gamma \tag{4.6}$$

$$\sum_{\beta=1}^{N_\beta} h_\beta \bar{\varepsilon}_{22}^{(\alpha\beta\gamma)} = h\bar{\varepsilon}_{22}, \qquad \alpha = 1,\ldots,N_\alpha, \quad \gamma = 1,\ldots,N_\gamma \tag{4.7}$$

$$\sum_{\gamma=1}^{N_\gamma} l_\gamma \bar{\varepsilon}_{33}^{(\alpha\beta\gamma)} = l\bar{\varepsilon}_{33}, \qquad \alpha = 1,\ldots,N_\alpha, \quad \beta = 1,\ldots,N_\beta \tag{4.8}$$

$$\sum_{\alpha=1}^{N_\alpha}\sum_{\beta=1}^{N_\beta} d_\alpha h_\beta \bar{\varepsilon}_{12}^{(\alpha\beta\gamma)} = dh\bar{\varepsilon}_{12}, \qquad \gamma = 1,\ldots,N_\gamma \tag{4.9}$$

$$\sum_{\beta=1}^{N_\beta}\sum_{\gamma=1}^{N_\gamma} h_\beta l_\gamma \bar{\varepsilon}_{23}^{(\alpha\beta\gamma)} = hl\bar{\varepsilon}_{23}, \qquad \alpha = 1,\ldots,N_\alpha \tag{4.10}$$

$$\sum_{\alpha=1}^{N_\alpha}\sum_{\gamma=1}^{N_\gamma} d_\alpha l_\gamma \bar{\varepsilon}_{13}^{(\alpha\beta\gamma)} = dl\bar{\varepsilon}_{13}, \qquad \beta = 1,\ldots,N_\beta \tag{4.11}$$

Eqs. (4.6)-(4.11) then form a rectangular system of equations which can be written in matrix form as follows

$$\mathbf{A}_G\boldsymbol{\varepsilon}_s = \mathbf{J}\bar{\boldsymbol{\varepsilon}} \tag{4.12}$$

The additional equations are obtained by imposing the interfacial continuity of tractions in a surface-average sense,

$$\bar{\sigma}_{11}^{(\alpha\beta\gamma)} = \bar{\sigma}_{11}^{(\hat{\alpha}\beta\gamma)} \qquad \alpha = 1,\ldots,N_\alpha - 1, \quad \beta = 1,\ldots,N_\beta, \quad \gamma = 1,\ldots,N_\gamma \tag{4.13}$$

$$\bar{\sigma}_{22}^{(\alpha\beta\gamma)} = \bar{\sigma}_{22}^{(\alpha\hat{\beta}\gamma)} \qquad \alpha = 1,\ldots,N_\alpha, \quad \beta = 1,\ldots,N_\beta - 1, \quad \gamma = 1,\ldots,N_\gamma \tag{4.14}$$

$$\bar{\sigma}_{33}^{(\alpha\beta\gamma)} = \bar{\sigma}_{33}^{(\alpha\beta\hat{\gamma})} \qquad \alpha = 1,\ldots,N_\alpha, \quad \beta = 1,\ldots,N_\beta, \quad \gamma = 1,\ldots,N_\gamma - 1 \tag{4.15}$$

$$\bar{\sigma}_{23}^{(\alpha\beta\gamma)} = \bar{\sigma}_{23}^{(\alpha\hat{\beta}\gamma)} \qquad \alpha = 1,\ldots,N_\alpha, \quad \beta = 1,\ldots,N_\beta - 1, \quad \gamma = 1,\ldots,N_\gamma \tag{4.16}$$

$$\bar{\sigma}_{32}^{(\alpha\beta\gamma)} = \bar{\sigma}_{32}^{(\alpha\beta\hat{\gamma})} \qquad \alpha = 1,\ldots,N_\alpha, \quad \beta = N_\beta, \quad \gamma = 1,\ldots,N_\gamma - 1 \tag{4.17}$$

$$\bar{\sigma}_{13}^{(\alpha\beta\gamma)} = \bar{\sigma}_{13}^{(\hat{\alpha}\beta\gamma)} \qquad \alpha = 1,\ldots,N_\alpha - 1, \quad \beta = 1,\ldots,N_\beta, \quad \gamma = 1,\ldots,N_\gamma \tag{4.18}$$

$$\bar{\sigma}_{31}^{(\alpha\beta\gamma)} = \bar{\sigma}_{31}^{(\alpha\beta\hat{\gamma})} \qquad \alpha = N_\alpha, \quad \beta = 1,\ldots,N_\beta, \quad \gamma = 1,\ldots,N_\gamma - 1 \tag{4.19}$$

$$\bar{\sigma}_{12}^{(\alpha\beta\gamma)} = \bar{\sigma}_{12}^{(\hat{\alpha}\beta\gamma)} \qquad \alpha = 1,\ldots,N_\alpha - 1, \quad \beta = 1,\ldots,N_\beta, \quad \gamma = 1,\ldots,N_\gamma \tag{4.20}$$

$$\bar{\sigma}_{21}^{(\alpha\beta\gamma)} = \bar{\sigma}_{21}^{(\alpha\hat{\beta}\gamma)} \qquad \alpha = N_\alpha, \quad \beta = 1,\ldots,N_\beta - 1, \quad \gamma = 1,\ldots,N_\gamma \tag{4.21}$$

Using Eq. (4.4), the above traction continuity equations are expressed in terms of the subcell strains, and then combined and written in matrix form as follows

$$\mathbf{A}_M(\boldsymbol{\varepsilon}_s - \boldsymbol{\varepsilon}_s^I - \boldsymbol{\varepsilon}_s^T) = \mathbf{0} \tag{4.22}$$

Combining the interfacial displacement and traction continuity equations, Eq (4.12) and (4.22), yields the following square system of equations

$$\tilde{\mathbf{A}}\boldsymbol{\varepsilon}_s - \tilde{\mathbf{D}}(\boldsymbol{\varepsilon}_s^I + \boldsymbol{\varepsilon}_s^T) = \mathbf{K}\bar{\boldsymbol{\varepsilon}} \tag{4.23}$$

where

$$\tilde{\mathbf{A}} = \begin{bmatrix} \mathbf{A}_M \\ \mathbf{A}_G \end{bmatrix}, \quad \tilde{\mathbf{D}} = \begin{bmatrix} \mathbf{A}_M \\ \mathbf{0} \end{bmatrix}, \quad \mathbf{K} = \begin{bmatrix} \mathbf{0} \\ \mathbf{J} \end{bmatrix}$$

Rearranging Eq. (4.23) to solve for the subcell strains $\boldsymbol{\varepsilon}_s$ yields

$$\boldsymbol{\varepsilon}_s = \mathbf{A}\bar{\boldsymbol{\varepsilon}} - \mathbf{D}(\boldsymbol{\varepsilon}_s^I + \boldsymbol{\varepsilon}_s^T) \tag{4.24}$$

Eq. (4.24) can be manipulated to yield the average strain in $(\alpha\beta\gamma)$ subcell

$$\bar{\boldsymbol{\varepsilon}}^{(\alpha\beta\gamma)} = \mathbf{A}^{(\alpha\beta\gamma)}\bar{\boldsymbol{\varepsilon}} + \mathbf{D}^{(\alpha\beta\gamma)}(\boldsymbol{\varepsilon}_s^I + \boldsymbol{\varepsilon}_s^T) \tag{4.25}$$

Substituting Eq. (4.25) into the general constitutive equation in Eq. (4.4) yields

$$\bar{\boldsymbol{\sigma}}^{(\alpha\beta\gamma)} = \mathbf{C}^{(\alpha\beta\gamma)}[\mathbf{A}^{(\alpha\beta\gamma)}\bar{\boldsymbol{\varepsilon}} + \mathbf{D}^{(\alpha\beta\gamma)}(\boldsymbol{\varepsilon}_s^I + \boldsymbol{\varepsilon}_s^T) - (\bar{\boldsymbol{\varepsilon}}^{I(\alpha\beta\gamma)} + \bar{\boldsymbol{\varepsilon}}^{T(\alpha\beta\gamma)})] \tag{4.26}$$

Finally, using the above equation in Eq. (4.5), the effective governing stress-stress relation for the triply-periodic composite can be written as

$$\bar{\boldsymbol{\sigma}} = \mathbf{B}^*(\bar{\boldsymbol{\varepsilon}} - \bar{\boldsymbol{\varepsilon}}^I - \bar{\boldsymbol{\varepsilon}}^T) \tag{4.27}$$

where $\mathbf{B}^*$ is the effective elastic stiffness tensor of the composite given by

$$\mathbf{B}^{*} = \frac{1}{dhl}\sum_{\alpha=1}^{N_\alpha}\sum_{\beta=1}^{N_\beta}\sum_{\gamma=1}^{N_\gamma} d_\alpha h_\beta l_\gamma \mathbf{C}^{(\alpha\beta\gamma)}\mathbf{A}^{(\alpha\beta\gamma)} \tag{4.28}$$

and the inelastic strain tensor of the composite is defined as

$$\bar{\boldsymbol{\varepsilon}}^{I} = \frac{-\mathbf{B}^{*-1}}{dhl}\sum_{\alpha=1}^{N_\alpha}\sum_{\beta=1}^{N_\beta}\sum_{\gamma=1}^{N_\gamma} d_\alpha h_\beta l_\gamma \mathbf{C}^{(\alpha\beta\gamma)}(\mathbf{D}^{(\alpha\beta\gamma)}\boldsymbol{\varepsilon}_s^{I} - \bar{\boldsymbol{\varepsilon}}^{I(\alpha\beta\gamma)}) \tag{4.29}$$

and the average thermal strain tensor as

$$\bar{\boldsymbol{\varepsilon}}^{T} = \frac{-\mathbf{B}^{*-1}}{dhl}\sum_{\alpha=1}^{N_\alpha}\sum_{\beta=1}^{N_\beta}\sum_{\gamma=1}^{N_\gamma} d_\alpha h_\beta l_\gamma \mathbf{C}^{(\alpha\beta\gamma)}(\mathbf{D}^{(\alpha\beta\gamma)}\boldsymbol{\varepsilon}_s^{T} - \bar{\boldsymbol{\varepsilon}}^{T(\alpha\beta\gamma)}) \tag{4.30}$$

4.2 Repeating Unit Cell Geometry

In this study, two distinct classes of GMC repeating unit cells are employed for varying volume fractions of the matrix and inclusion materials in the graded coatings. The first type of RUC represents a square inclusion within a matrix while the second RUC approximates a spherical inclusion within a matrix. With each type of RUC the aim is to determine the effective response of the four homogenized graded layers used in the HOTCFGM analysis of graded thrust cell liners in Section 5 (see Figure 2.2c). The four layers considered vary on the basis of NARloy-Z and NiCrAlY volume fractions, respectively. The layer nearest the coating, for example, consists of 80% NiCrAlY and 20% NARloy-Z. Likewise, the layer nearest the NARloy-Z substrate consists of 80% NARloy-Z and 20 NiCrAlY. Similarly, the two intermediate layers of the graded region consist of the corresponding 40%-60% ratio of the constituents. For clarity, all results reported herein list only the volume fraction of NiCrAlY in the specific composite. Additionally, the use of two distinct inclusion shapes provides a direct means of identifying the influence of inclusion shape on the effective response of NiCrAlY/NARloy-Z particulate composites, which may potentially be significant as discussed by Arnold et al. (1996).

4.2.1 Cubical Inclusion (2x2x2)

Figure 4.1 shows the RUC consisting of eight subcells (2x2x2) for the square inclusion case. The gray corner cell represents the inclusion while the matrix material surrounding the inclusion is represented by the seven dashed white boxes. The inclusion shown in Figure 4.1 occupies one eighth of the volume of the entire RUC, thus this inclusion has a volume fraction of 0.125. In order to compute the effective response of layers containing different volume fractions of the NiCrAlY and NARloy-Z phases, the overall dimensions of the RUC were adjusted accordingly, keeping the inclusion dimensions fixed. For instance, for the layer with the NiCrAlY volume fraction of 0.2, NiCrAlY was modeled as the inclusion phase while NARloy-Z was the matrix phase, conversely in the case when the NiCrAlY volume fraction was 0.8, NARloy-Z was considered the inclusion and NiCrAlY the matrix. The same approach was used to calculate the effective response of the layers containing NiCrAlY volume fractions of 0.4 and 0.6.

4.2.2 Spherical Inclusion (12x12x12)

The RUC illustrating the approximation of a spherical inclusion is shown in Figure 4.2. The inclusion shown in gray consists of just 280 of the total 1728 subcells (12x12x12) employed to model the entire RUC. As was the case with the square inclusion, the outer dimensions of the matrix were varied in order

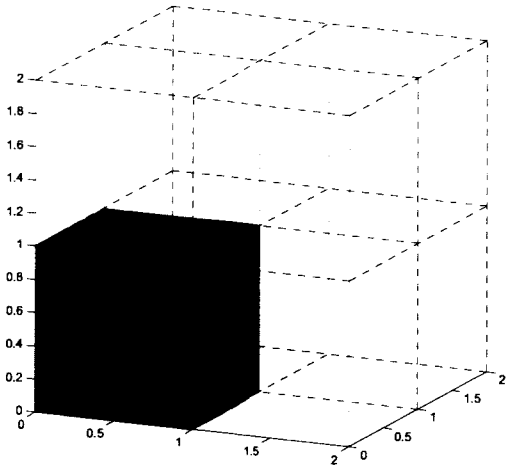

Figure 4.1. Repeating unit cell geometry for square inclusion.

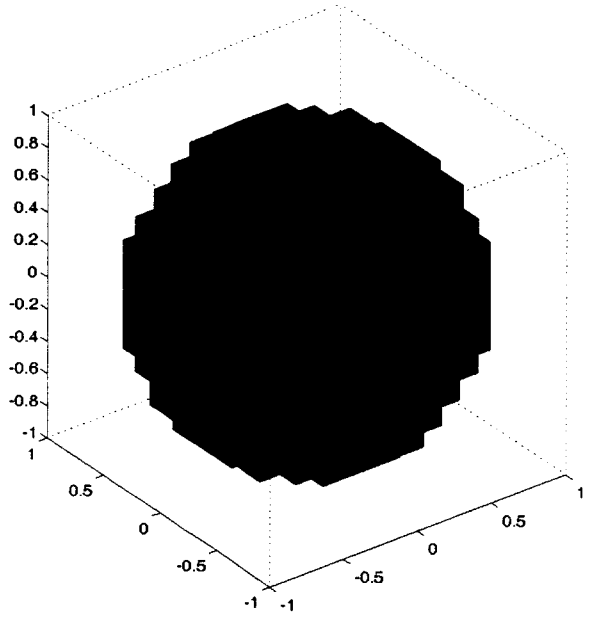

Figure 4.2. Repeating unit cell geometry for an inclusion approximating a sphere.

to achieve inclusion volume fractions of 0.2 and 0.4. Subsequently, NARloy-Z and NiCrAlY were each modeled as the inclusion for the respective volume fractions to produce the effective response for each of the four NiCrAlY/NARloy-Z composite layers.

4.3 Effective Homogenized Properties

4.3.1 Effective Thermoelastic Parameters

The effective thermoelastic properties predicted by GMC-3D for each of the homogenized layers and the two inclusion geometries are presented in this section. Table 4.1 shows a comparison of the temperature

independent properties of E, ν, κ, ρ and C_p by inclusion shape as a function of the volume fraction of NiCrAlY in the composite layer. Density and specific heat are not tensor quantities, and thus do not vary with inclusion shape. Subsequently, these effective properties were determined through rule-of-mixtures computations. The remaining thermoelastic properties taken to be independent of temperature, however, are tensor quantities which can be calculated using the GMC-3D equations of the preceding section from the properties of the individual constituents.

Table 4.1. Temperature independent properties of the four homogenized layers based on the volume fraction of NiCrAlY.

v_f	E (*GPa*)		ν		κ ($W/m \cdot K$)		ρ (kg/m^3)	C_p ($J/g \cdot K$)
	Cube	Sphere	Cube	Sphere	Cube	Sphere		
0.2	148.9	148.9	0.327	0.327	231.5	207.6	8400	409
0.4	150.9	150.8	0.314	0.314	165.0	125.4	8100	438
0.6	152.7	152.6	0.300	0.300	29.1	34.12	7700	467
0.8	154.4	154.3	0.285	0.285	18.0	18.12	7300	496

Table 4.2. Thermal expansion coefficients of the four homogenized layers at different NiCrAlY volume fractions and temperatures.

α (10^{-6}/°C)								
Temp (°C)	$v_f = 0.2$		$v_f = 0.4$		$v_f = 0.6$		$v_f = 0.8$	
	Cube	Sphere	Cube	Sphere	Cube	Sphere	Cube	Sphere
-245 → 21	16.75	16.74	15.63	15.62	14.48	14.45	13.27	13.27
260	16.84	16.84	15.82	15.81	14.77	14.74	13.66	13.63
538 → 700	17.01	17.01	16.16	16.15	15.28	15.26	14.37	14.34
800	17.05	17.04	16.24	16.23	15.40	15.38	14.52	14.50
900	17.10	17.08	16.32	16.30	15.52	15.50	14.66	14.66

With the exception of the thermal conductivity, κ, the predicted properties listed in Table 4.1 indicate that the effective properties vary only slightly with inclusion shape for the employed constituents. E and ν (see Section 2.4.2), for instance, are virtually identical for the NARloy-Z/NiCrAlY particulate composite with cubical and spherical inclusions. It should be noted, however, that with greater contrast between constituent values of E and ν, greater differences in the effective properties would be expected based on the employed inclusion shape. In the case of the thermal conductivities, however, the individual constituents have markedly different values of κ. Similarly, the full utility of GMC-3D, and micromechanics models in general, is best demonstrated in composites consisting of dissimilar

constituents since in the case of nearly identical constituents GMC-3D and simple averaging techniques yield approximately the same effective properties.

Table 4.2 presents the effective coefficient of thermal expansion (CTE) at a given volume fraction of NiCrAlY and temperature, where the CTE remains constant from -245 °C to 21 °C and 538 °C to 700 °C, for each type of inclusion. Virtually no difference in the effective properties predicted for the two inclusion shapes is observed. This is consistent with the relatively similar thermal expansion coefficients for NARloy-Z and NiCrAlY.

4.3.2 Effective Power-Law Creep Parameters

The effective power-law creep parameters of the NiCrAlY/NARloy-Z composite layers were determined by applying various constant stress levels (i.e. creep test) within GMC to each of the repeating unit cell representations of these layers while continuously monitoring the effective macro-scale strain. The resultant creep curves were then fitted to the power-law creep form, yielding the effective creep coefficients and exponents. Tables 4.3-4.5 show the predicted power-law creep parameters of the employed NiCrAlY/NARloy-Z composites. Several noteworthy trends are observed in these tables. First, as seen in the previous results for temperature independent thermoelastic properties and the CTEs, little variation is observed due to inclusion shape when determining the effective power-law creep parameters of similar constituents. The constituents employed to predict the effective inelastic parameters shown in Table 4.3 each have a power-law creep exponent of $n = 1.20$, likewise each effective $\bar{n}$ is also 1.20, suggesting that n is transmissible from the micro-level to the macro-level in this case. That is, the constituent phases each follow Eq. (2.27), while the effective response of the composite is given by

$$\overline{F}(\bar{\sigma}_e, T) = \overline{A}(T)\bar{\sigma}_e^{\bar{n}(T)} \tag{4.31}$$

When the constituents exhibit dissimilar creep exponents, however, the effective creep exponents are shown to vary with volume fraction of NiCrAlY (see Table 4.4 and Table 4.5), but the effective power-law creep form of Eq. (4.31) is retained. Once more, greater variation in constituent properties results in greater variation in the predicted effective properties of the NiCrAlY/NARloy-Z composites for both inclusion shapes.

Table 4.3. Power-law creep parameters for the NiCrAlY/NARloy-Z composite by volume fraction of NiCrAlY, inclusion shape and temperature when $n = 1.2$ for NiCrAlY and NARloy-Z.

A (10^{-7} MPa^{-n}/s)								
Temp (°C)	$v_f = 0.2$		$v_f = 0.4$		$v_f = 0.6$		$v_f = 0.8$	
	Cube	Sphere	Cube	Sphere	Cube	Sphere	Cube	Sphere
-245 → 21	2.005	2.032	1.502	1.555	1.152	1.205	0.951	0.968
260	2.369	2.410	1.672	1.749	1.209	1.286	0.976	0.999
538 → 700	3.288	3.370	2.059	2.199	1.310	1.448	1.018	1.057
800	3.405	3.478	2.555	2.386	1.529	1.659	1.210	1.248
900	4.033	4.061	3.351	3.409	2.829	2.888	2.466	2.486
n	1.20		1.20		1.20		1.20	

Table 4.4. Power-law creep parameters for the NiCrAlY/NARloy-Z composite by volume fraction of NiCrAlY, inclusion shape and temperature when $n = 2.25$ for NiCrAlY and $n = 2.75$ for NARloy-Z.

A (10^{-10} MPa^{-n}/s)								
Temp (°C)	$v_f = 0.2$		$v_f = 0.4$		$v_f = 0.6$		$v_f = 0.8$	
	Cube	Sphere	Cube	Sphere	Cube	Sphere	Cube	Sphere
-245 → 21	0.542	0.528	0.941	0.910	0.968	0.928	1.117	1.069
260	0.820	0.798	1.247	1.203	1.111	1.071	1.191	1.142
538 → 700	1.906	1.871	2.227	2.185	1.453	1.401	1.357	1.287
800	1.930	1.930	2.530	2.491	1.906	1.854	1.877	1.806
900	2.392	2.357	4.482	4.397	5.320	5.183	6.607	6.434
n	2.70		2.50		2.40		2.30	

Table 4.5. Power-law creep parameters for the NiCrAlY/NARloy-Z composite by volume fraction of NiCrAlY, inclusion shape and temperature when $n = 2.25$ for NiCrAlY and $n = 4.00$ for NARloy-Z.

A (10^{-12} MPa^{-n}/s)								
Temp (°C)	$v_f = 0.2$		$v_f = 0.4$		$v_f = 0.6$		$v_f = 0.8$	
	Cube	Sphere	Cube	Sphere	Cube	Sphere	Cube	Sphere
-245 → 21	0.274	0.296	4.462	5.577	42.86	51.14	54.61	59.08
260	0.481	0.522	5.941	8.089	47.50	60.84	57.72	63.63
538 → 700	1.460	1.703	11.09	18.13	58.01	80.35	64.00	71.94
800	1.543	1.758	13.45	20.67	78.83	108.7	91.87	102.1
900	2.101	2.225	31.68	34.99	270.0	288.4	365.8	371.1
n	3.65		3.00		2.50		2.40	

The second important trend is that as the inclusion occupies a larger portion of the RUC (i.e. 40% NARloy-Z or NiCrAlY), more variation is noted in the predicted power-law creep parameters resulting from the two inclusion shapes, particularly in cases where the constituent power-law creep parameters have greater contrast. This trend can be observed graphically in Figure 4.3 which shows a comparison of the response predicted by two sets of effective properties based on the cubical and spherical inclusion shapes for two different volume fractions of NiCrAlY. In modeling the composite containing a NiCrAlY volume fraction of 0.6, a NARloy-Z inclusion phase occupies 40% of the RUC, whereas in the representation of the composite containing a NiCrAlY volume fraction of 0.2, a NiCrAlY inclusion occupies only 20% of the RUC. The predicted responses for these two cases are shown on the right and left sides of Figure 4.3, respectively, and clearly demonstrate the trend.

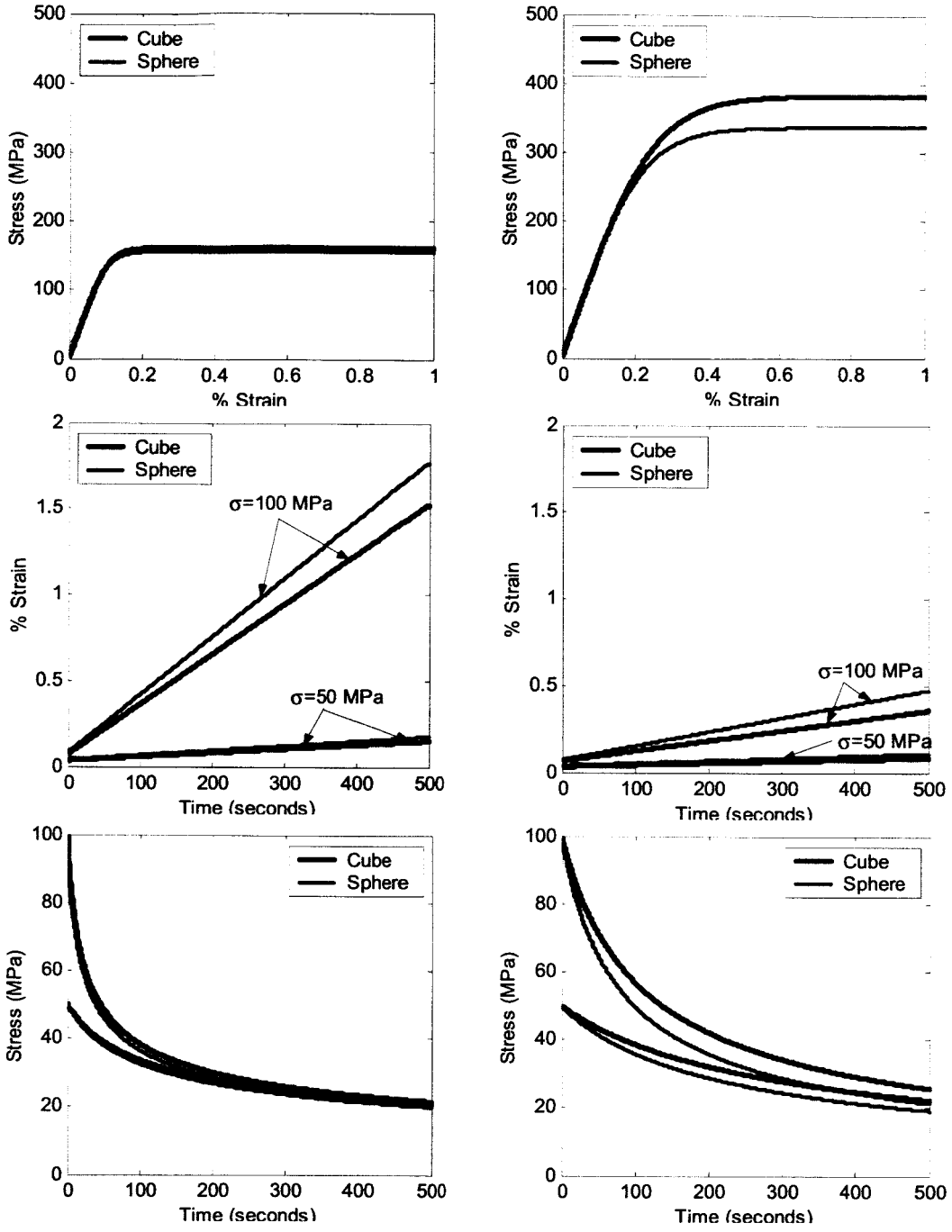

Temp = 700 °C, $v_f = 0.2$

Temp = 700 °C, $v_f = 0.6$

Figure 4.3. Comparison of constant strain-rate stress-strain response (top figures), creep response (middle figures), and relaxation response (bottom figures) for two sample sets of effective properties based on cubical and spherical inclusion shapes.

5 Parametric Studies

In this section, each of the RLV thrust cell liner configurations described in Section 2 is analyzed using the HOTCFGM approach in order to isolate the effects of specific parameters on thrust cell liner deformation and stress fields. Isolating and identifying the parameters responsible for the characteristic deformations observed by Quentmeyer and others is the first step towards the goal of achieving improved thrust cell liner performance and durability. Specifically, geometry and material effects are studied, and in particular the effects of cooling channel wall thickness, copper closeout material, coating presence and thickness, as well as grading. The effective properties of the particulate NARloy-Z/NiCrAlY composite determined in Section 4 are employed in the parametric study of the effect of grading in order to contrast the homogenization-based approach with that based on the actual microstructural details. Additionally, the effect of creep coefficients and exponents is investigated within the context of the aforementioned studies. As described in Section 3.3 an accelerated modeling procedure is employed in which the creep coefficients are multiplied by a factor of 10, thereby increasing the creep rate by the same amount.

5.1 Effect of Cooling Channel Wall Thickness

As outlined in Section 2, the cooling channel wall thickness of a NARloy-Z thrust cell liner can be varied to provide an understanding of the effect of solely this parameter on thermal profiles, stress fields, and ultimately deformations. In this section, NARloy-Z thrust cell liners employing a cooling channel wall thickness of 10 mils, 35 mils and 50 mils, respectively, are analyzed and compared.

Thermal results for each wall thickness are presented first. Figure 5.1 illustrates the variation of the temperature fields with time within the entire NARloy-Z thrust cell liner cross section for each of the different wall thickness cases mentioned above. The second row in Figure 5.1 illustrates the evolution of the temperature field within the cross-section of the same NARloy-Z configuration as that investigated by Arya and Arnold at five times during the outset of the thermal cycle, t = 1.5, 2.0, 2.5, 5.0 and 10.0 seconds. The first two times corresponds to the middle and end of the ramping period, in which the temperature is increased to the maximum value, while the final three times are in the early stages of the hold period. The transient thermal effects are clearly apparent, with the temperatures initially rising very rapidly during and shortly after the ramping period before reaching a steady state early in the hot phase of the cycle at approximately 5.0 seconds. This steady state temperature distribution compares favorably with that obtained by Arya and Arnold for their extended cycle.

The first and third rows of Figure 5.1 clearly demonstrate the impact of the cooling channel location on the overall temperature field. In the case of the 50-mil wall thickness, for example, a greater portion of the cross section is exposed to the extreme temperatures than is the case for the 10-mil wall thickness where the extreme temperatures are focused in a much smaller region. In the region immediately surrounding the cooling channel, however, the radial temperature gradients are very similar with time despite the varying configurations, as the geometric configuration does not appear to have an effect on transient response. This observation is further demonstrated in Figure 5.2 which shows a comparison of the temperatures predicted after a steady state is achieved as a function of radial position along the left and right radial boundaries of the cross section for each wall thickness. The circumferential gradient observed at the inner radius of the cooling channel wall does, however, vary substantially with cooling channel wall thickness. In the case of the thin cooling channel wall, for example, this gradient is much more severe than in the case of the thick cooling channel wall. This indicates that decreasing cooling channel wall thickness promotes more intense circumferential thermal gradients at the inner radius of the thrust cell liner, likely promoting deformations in the same region. Figure 5.3 shows a comparison of the steady-state temperatures predicted along the inner radius of the thrust cell liner for each wall thickness, quantitatively demonstrating the extent of circumferential gradient.

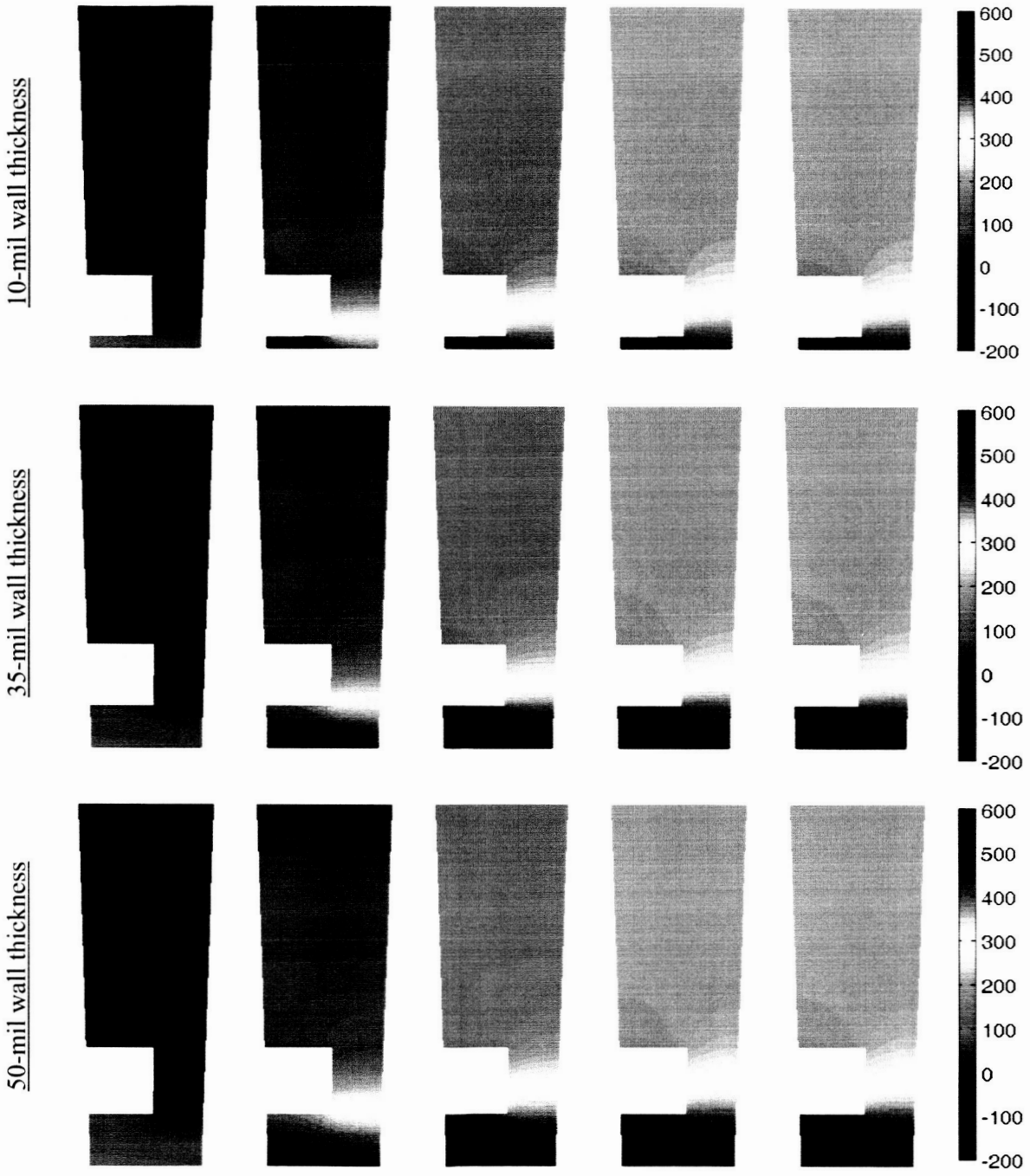

Figure 5.1. Temperature evolution (^{0}C) within NARloy-Z cross-sectional liners at five times during the thermal cycle, t = 1.5, 2.0, 2.5, 5.0 and 10.0 seconds for the three distinct wall thickness cases.

Thermal gradients, however, are not the only concern when varying the cooling channel wall thickness of NARloy-Z thrust cell liners. The power required for cooling the structure as well as the maximum temperatures the structure is exposed to must also be considered. Figure 5.4 presents the heat flux into the cooling channel for each configuration as a function of time. Because the cooling channel is

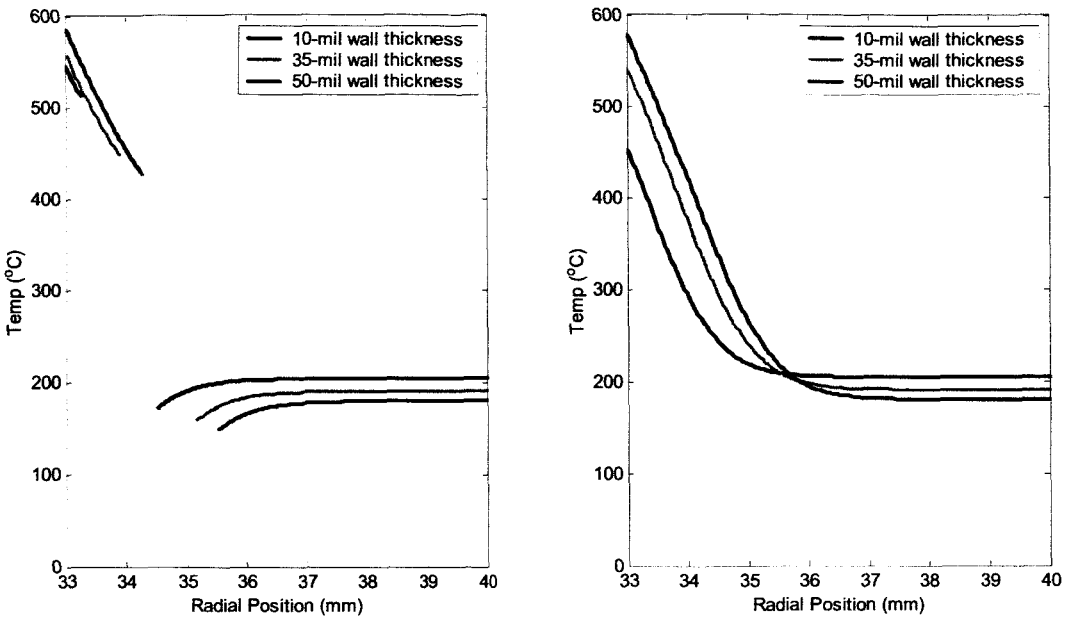

Figure 5.2. Steady-state temperature distributions along the left and right radial edges of the cross section for 10, 35 and 50-mil wall thickness NARloy-Z thrust cell liners.

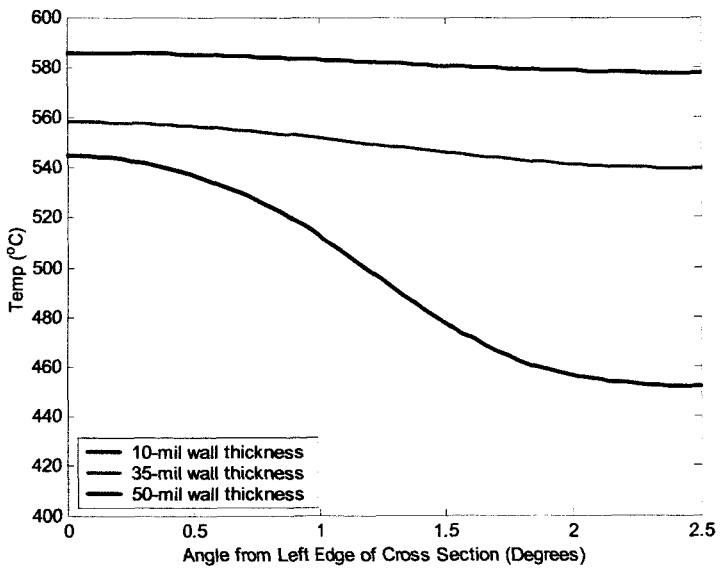

Figure 5.3. Steady-state temperature distributions along the inner radius of 10, 35 and 50-mil wall thickness NARloy-Z thrust cell liners.

located closer to the combustion chamber, the magnitude of the flux that passes through to the cooling channel wall into the cooling channel increases. Such an increase in flux can increase or decrease engine efficiency depending on the specific type of engine cycle employed in the overall system. An expander cycle engine, for example, benefits from increased flux as this additional energy helps drive turbo pumps

Ellis (2003). Conversely, a full flow stage combustion cycle engine actually loses efficiency when more flux is transmitted to the cooling channel as less power is necessary to drive the flow of coolant in the cooling channel in order to maintain the same cooling temperature, Ellis (2003). Consequently, the fluxes presented must be interpreted with respect to the specific engine cycle employed in conjunction with the analyzed thrust cell liner and are, therefore, presented as a tool for the engine designer.

In Figure 5.4, the 50-mil cooling channel wall thickness configuration is shown to transfer the smallest magnitude of flux of the three configurations. However, re-examination of Figure 5.3 reveals that the temperatures at the inner radius of the thrust cell liner are also the largest for this configuration, thus illustrating the competition/connection between power considerations and structural temperature exposure. In order to maintain the same temperatures at the inner radius of the thrust cell liner for the 50-mil cooling channel wall thickness case as in the 35-mil cooling channel wall thickness case, for example, additional cooling power would be required. Depending on the thrust cell liner material, maintaining a specific maximum temperature is a particular concern due to the detrimental effects of oxidation and blanching discussed in Section 1. For NARloy-Z, however, the temperatures shown are not significant enough to cause a change in mechanism likely to promote severe deterioration of the thrust cell liner wall Ellis (2003). For other materials, such as GRcop-84, these concerns do become much more important.

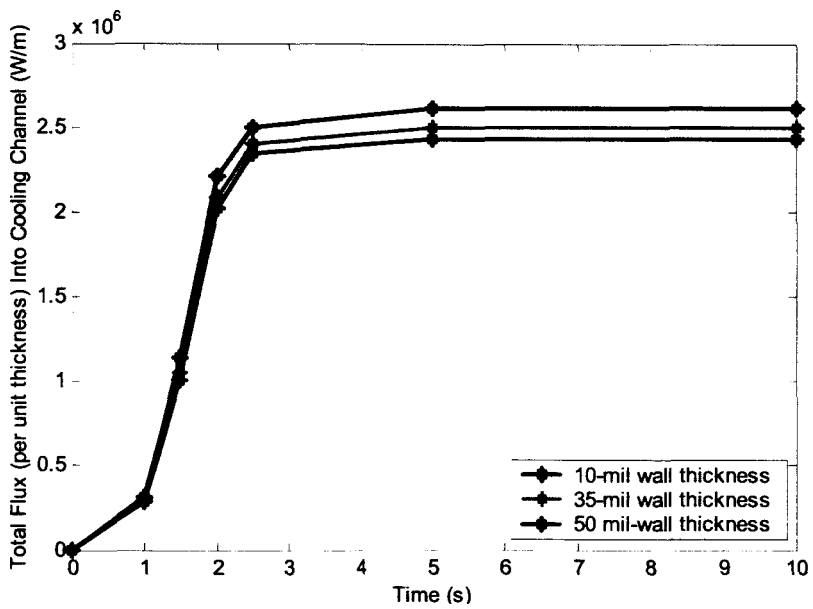

Figure 5.4. Total flux into the cooling channel of 10, 35 and 50-mil wall thickness NARloy-Z thrust cell liners as a function of time.

Although the circumferential thermal gradients observed in the thermal profiles suggest that the 10-mil cooling channel wall thickness configuration could adversely affect the deformation of the cooling channel wall, a closer look at the model predicted deformations is necessary. Likewise, the absence of circumferential thermal gradients in the case of the 50-mil cooling channel wall thickness suggests that this configuration is most likely to minimize deformation of the cooling channel. In the following sections, deformed shapes are presented and discussed according to small, intermediate and large creep exponents employed in the power-law creep model for NARloy-Z.

5.1.1 Small Creep Exponent (n = 1.2)

Turning to the predicted deformed shapes, it is possible to observe the direct effect of geometric configuration on liner durability. Figure 5.5 illustrates the evolution of deformation at the cross sectional boundaries for each configuration of the NARloy-Z thrust cell liner during the cycle at t = 1.0, 100, 200, 400 and 500 seconds. For each case, there is an initial radial contraction of the liner's cross section due to the cooling which occurs in the cooling channel prior to the initial ramping of the temperature. However, by the time steady-state thermal response is achieved some bowing out in the cooling channel wall becomes apparent. This bowing out continues to grow throughout the hot phase of the cycle and, in the case of the liner with a 10-mil wall thickness, results in extremely large deformation by the time 200 seconds are reached. This clearly shows that an uncoated thrust cell liner of this geometry and material is not feasible for a material exhibiting such a high creep rate under these loading conditions. In the same application, however, the material creep rate 1/10 of that employed in this analysis (based on the creep coefficient of Section 2) would not exhibit deformations of such a magnitude that failure could be predicted, thus demonstrating the utility of increasing the creep rate for use in an accelerated modeling procedure. This type of failure, by bowing out and thinning of the cooling channel wall, has been observed experimentally and demonstrated to a lesser extent by the results of Arya and Arnold under cyclic loading involving much shorter cycles. These results illustrate that the HOTCFGM accelerated modeling procedure, in conjunction with the efficient power-law creep model, has achieved the desired blend of accuracy and efficiency sought at the outset of this investigation.

In the case of the 35-mil and 50-mil wall thickness liners, the bowing out that does occur is not nearly as dramatic as in the 10-mil wall thickness case and never reaches a magnitude at which a similar structural failure is predicted. At the completion of the cycle, each of these liners is predicted to remain structurally intact. Nevertheless, the thinning of the wall at the circumferential centerline of cooling channel as well as the bowing out across the cooling channel wall that may ultimately lead to structural failure under cyclic loading is clearly evident.

The results shown in Figure 5.5 confirm the expected outcome that increasing the wall thickness reduces the amount of bowing out seen in the cooling channel wall. This further supports the conclusion reached by Arya and Arnold that the "dog-house" failure mode is a result of biasing pressure differential across the cooling channel wall. As the cooling channel wall thickness is reduced, less material is available to support the pressure in the cooling channel, and as this material becomes more compliant with temperature it can no longer resist the internal pressure and is forced outward until failure occurs due to creep effects. The failure predicted in the 10- mil wall thickness case and the bowing out and thinning exhibited in the 35-mil and 50-mil wall thickness cases present a strong argument for the use of a coating to limit the temperatures seen in the structure of the cooling channel wall. Limiting these temperatures will also reduce creep effects as was shown in the material characterization section of Section 2.

5.1.2 Intermediate Creep Exponent (n = 2.75)

As discussed in Section 2, in the case of the intermediate creep exponent and corresponding creep coefficient, smaller creep rate is observed relative to the small exponent case, thus less deformation is expected. The results presented in Figure 5.6 support this, as the predicted deformations for each of the three wall thickness configurations are dramatically reduced compared to the analyses based on the small creep exponent. In fact, the predicted failure previously seen in the 10-mil cooling channel wall thickness configuration is averted in the intermediate creep exponent analysis. Similarly, little end-of-cycle deformation is observed in both the 35-mil and 50-mil cooling channel wall thickness configurations, and the previously observed bowing and thinning of the cooling channel wall is completely eliminated when this pair of creep parameters are used in a single cycle analysis. Though virtually indistinguishable, the 50-mil wall thickness configuration does once again exhibit the smallest end-of-cycle deformation, which

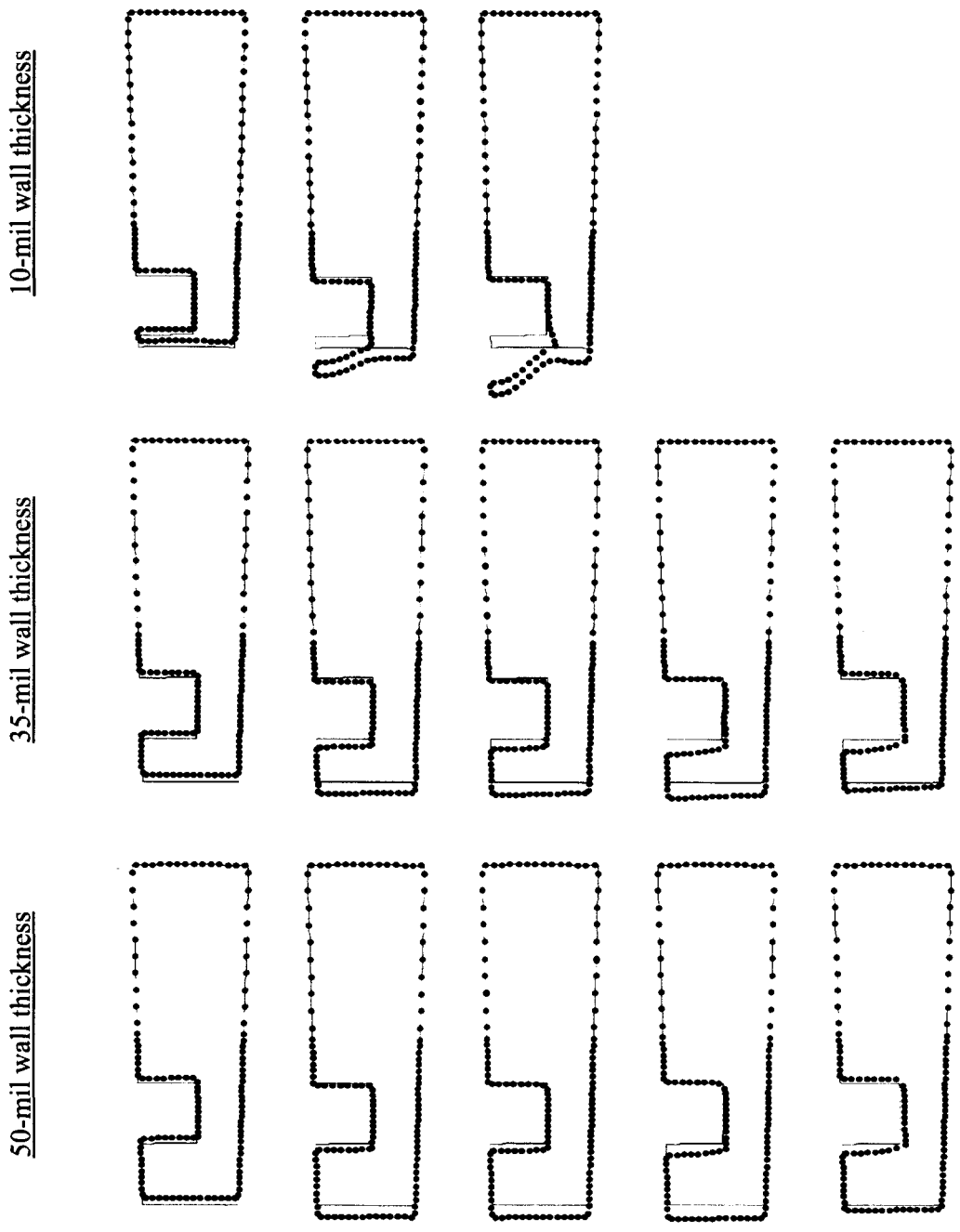

Figure 5.5. Cross-sectional deformation of NARloy-Z thrust cell liner for small creep exponents at five times during the thermal cycle, t = 1.0, 100, 200, 400 and 500 seconds. Solid lines show undeformed shapes. Dotted lines show deformed shapes with all deformations magnified 5 times.

suggests that the 50-mil cooling channel wall thickness may be the unequaled design choice in terms of limiting the characteristic "dog-house" type failure modes. The concerns of engine designers discussed in Section 5.1 would also have to be taken into account before such broad conclusion is drawn, but solely in

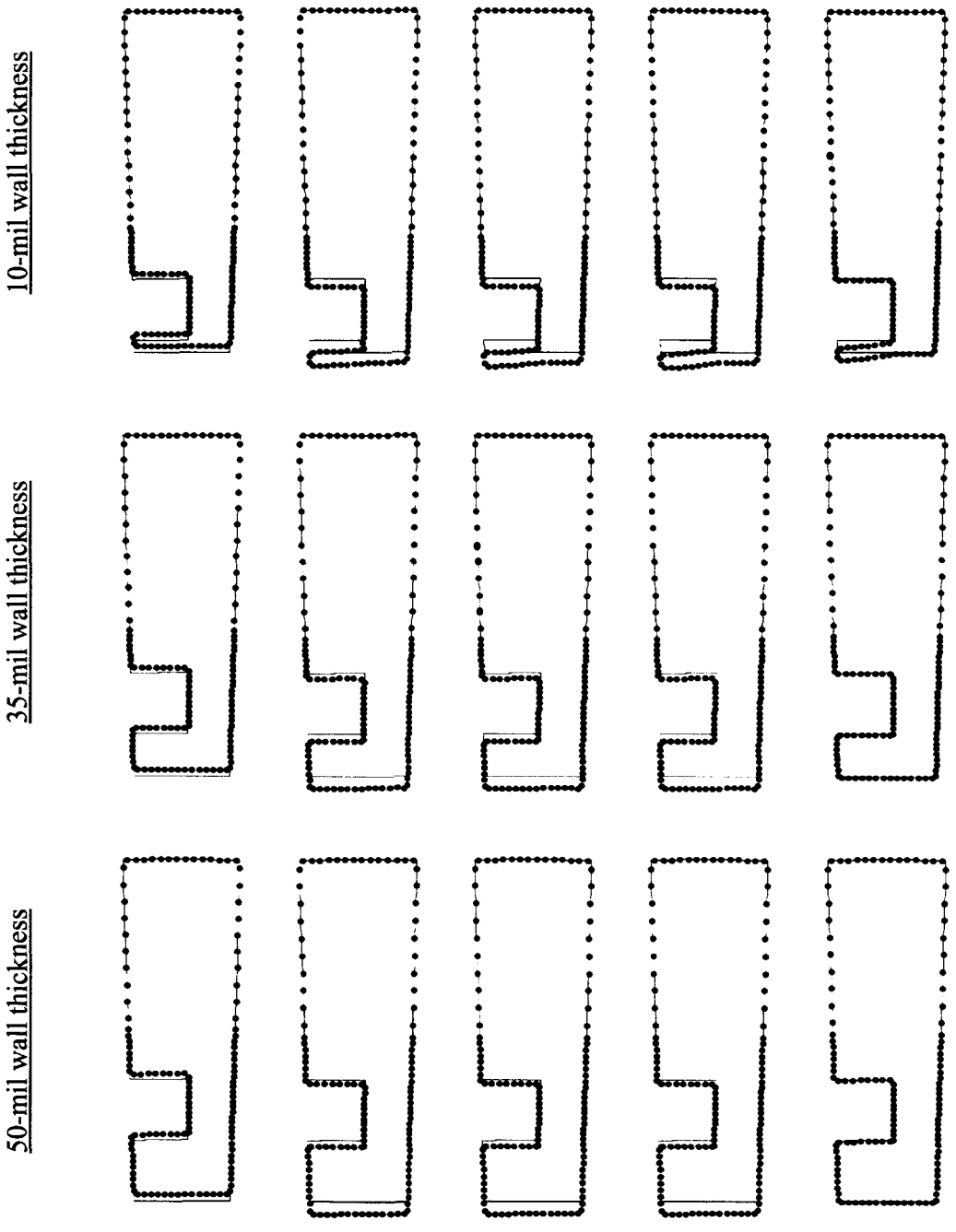

Figure 5.6. Cross-sectional deformation of NARloy-Z thrust cell liner for intermediate creep exponents at five times during the thermal cycle, t = 1.0, 100, 200, 400 and 500 seconds. Solid lines show undeformed shapes. Dotted lines show deformed shapes with all deformations magnified 5 times.

the context of the observed deformations leading to the above-mentioned failure modes increasing the wall thickness has a mitigating effect. The mitigating effect is seen to have diminishing returns as the creep rate is reduced compared to the previous case in which the small creep exponent was employed.

5.1.3 Large Creep Exponent (n = 4.0)

In Section 2, the combination of large creep exponent and correspondingly small creep coefficient was shown to produce the smallest creep rate of the various matched pairs of these parameters. This pair was also noted to produce creep and relaxation results most similar to the corresponding results obtained from the Robinson's model for the NARloy-Z alloy. In this section, as in the previous section, less creep-induced deformation is therefore expected in the structural analysis of the same cross sections relative to the analyses employing smaller creep exponents but higher creep rates. Once again the hypothesis holds as Figure 5.7 shows the predicted deformations for the 10-mil wall thickness case, while the 35-mil and 50-mil wall thickness cases mirror the results shown in Figure 5.6. The deformations observed in Figure 5.7 are not considerably different from those shown for the corresponding case in Figure 5.6, but again are dramatically reduced in comparison to the deformations given in Figure 5.5 based on the analyses employing the small creep exponent. For the 35-mil and 50-mil wall thickness cases, end-of-cycle deformations are virtually eliminated when the large creep exponent is used in the analysis.

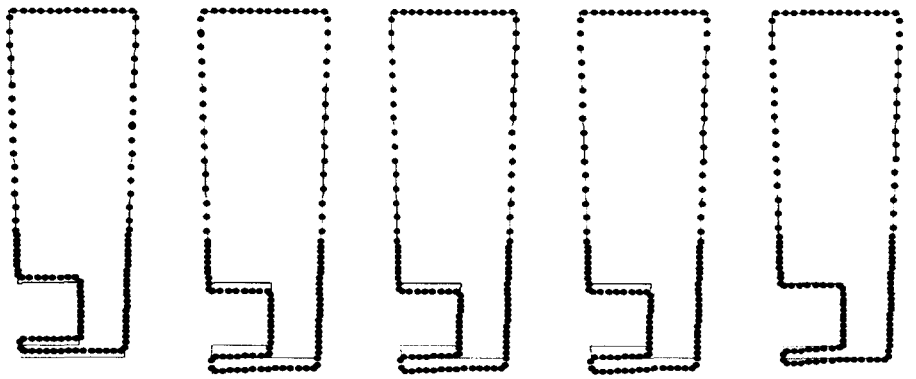

Figure 5.7. Cross-sectional deformation of 10-mil wall thickness NARloy-Z thrust cell liner for the large creep exponent at five times during the thermal cycle, t = 1.0, 100, 200, 400 and 500 seconds. Solid lines show undeformed shapes. Dotted lines show deformed shapes with all deformations magnified 5 times.

5.2 Effect of Adding Copper to Cross Section

Although the analysis of NARloy-Z thrust cell liners provides valuable insight into the parameters that may affect deformation of in-service thrust cell liners, present-day thrust cell liners are fabricated using a combination of NARloy-Z and electro-deposited copper (see Figure 2.2). In this study, however, OFHC copper was used in place of electro-deposited copper as discussed in Section 2. Figure 5.8 presents the variation of temperature fields with time within the three Cu/NARloy-Z thrust cell liner configurations with different cooling channel wall thickness studied previously in the NARloy-Z cases. The thermal analysis reveals very little change in the temperature profiles of the Cu/NARloy-Z configurations as compared to the temperature profiles of the pure NARloy-Z configurations shown in Figure 5.1. As an example, the maximum temperature occurring near the cooling channel wall in the 35-mil wall thickness case increases from 464 °C at the beginning of the hot phase to 541 °C at the end of the hot phase, a change of just 2 °C and 1 °C, respectively, from the corresponding NARloy-Z case. Despite the higher thermal conductivity of copper relative to NARloy-Z (see Table 2.3) there is little noticeable difference when comparing the two sets of thermal profiles. This is due in part to the absence of appreciable thermal gradients in the region where NARloy-Z is replaced by copper. In the absence of thermal gradients necessary to drive conductive heat flow, little overall temperature change is possible. This illustrates that

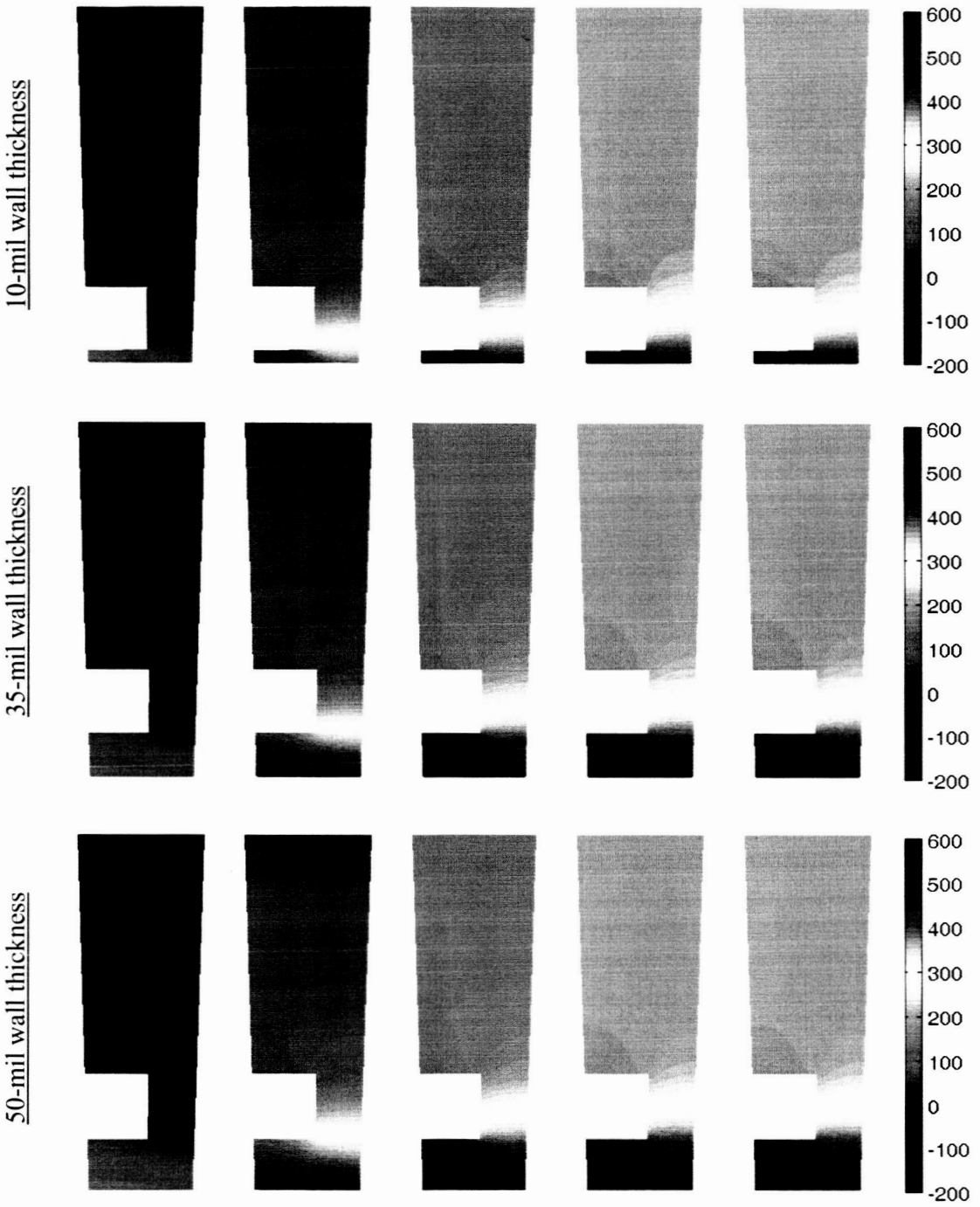

Figure 5.8. Temperature evolution (^{0}C) within Cu/NARloy-Z cross-sectional liners at five times during the thermal cycle, t = 1.5, 2.0, 2.5, 5.0 and 10.0 seconds for the three distinct wall thickness cases.

these two thrust cell liner configurations exhibit virtually the same thermal response, indicating that any difference in the mechanical response must be attributed to the different material properties of the individual constituents.

The following sections detail the mechanical response of the Cu/NARloy-Z thrust cell liners for each of the three cooling channel wall thicknesses as well as the small, intermediate and large creep exponents. Having noted the nearly identical thermal response of the Cu/NARloy-Z thrust cell liners compared to the NARloy-Z thrust liners, similar results should be expected. That is, increasing wall thickness is likely to mitigate bowing out and thinning of the cooling channel wall just as less deformation can be expected when the creep exponent is increased and the corresponding creep coefficient decreased, thereby resulting in a decreased creep rate.

5.2.1 Small Creep Exponents (n = 1.2)

Figure 5.9 presents the evolution of deformation at the cross-sectional boundaries corresponding to each thrust cell liner cooling channel wall thickness studied for the small creep exponent. The results shown in each row represent deformed Cu/NARloy-Z liners at five times during the thermal cycle, t = 1.0, 100, 200, 400 and 500 seconds. In the 10-mil wall thickness case, the results are similar to those obtained in the analysis of the NARloy-Z cross-section although the outward bowing is somewhat less dramatic. In contrast to the analyzed cross section composed solely of NARloy-Z, in the 35-mil and 50-mil cooling channel wall thickness cases the liner actually contracts at the end of the thermal cycle. Since the thermal profiles have been shown to be nearly identical, the deformation shown here can be directly attributed to the more compliant and less creep-resistant response of copper compared to NARloy-Z. This is particularly true given that copper is under compression caused by the pressure exerted in cooling channel and the constraint of the steel jacket at the outer radius of the thrust cell liner. The dissimilarities between OFHC copper and NARloy-Z become particularly important at elevated temperatures and although 200 °C is not an extreme temperature, substantial creep is observed for the employed set of parameters even at relatively low stress levels (see Figures 2.16 and 2.17).

In addition to the contraction of the Cu/NARloy-Z cross sections not seen in the NARloy-Z cases, there is also a greater extent of cooling channel enlargement predicted in the Cu/NARloy cases. This is particularly clear at the rear (outermost radial position) of the cooling channel in the 35-mil and 50-mil cooling channel wall thickness cases. Such enlargement at the rear of the cooling channel is not likely to result in failure of these Cu/NARloy-Z liners. However, evidence does exist to show that the addition of copper to the cross section may potentially have an adverse effect on thrust cell liner durability. In particular, Figure 5.10 presents a comparison of end-of-cycle cooling channel wall thickness at the centers of each of the 8 subcells employed along the cooling channel starting from the left boundary of the cross section to the right edge of the cooling channel wall for the NARloy-Z and Cu/NARloy-Z cases. This figure clearly shows that the cooling channel wall thickness is reduced to a greater extent in the case of the Cu/NARloy-Z cross section. Despite such evidence, the ease with which copper can be electro-deposited during the fabrication process is, however, advantageous. Thus the use of copper cannot be immediately ruled out.

Further explanation of the contrasting deformation results of NARloy-Z and Cu/NARloy-Z thrust cell liners is presented in Figure 5.11. This figure shows the evolution of inelastic radial strain within each cross-sectional liner configuration with the 35-mil cooling channel wall thickness at four times during the thermal cycle, t = 100, 200, 400 and 500 seconds. For each configuration, the inelastic radial strains are shown to exist in regions where large radial deformations are observed in the deformed shapes, particularly in the region immediately surrounding the cooling channel, illustrating a connection between deformations in the radial direction and the accumulation of inelastic radial strains. Specifically, more inelastic radial strain is observed in the neck-like region to the right of the cooling channel for the NARloy-Z configuration, thus explaining the outward radial expansion of the cross section relative to the Cu/NARloy-Z configuration. Furthermore, largely negative inelastic strains exist at the rear of the cooling channel in the Cu/NARloy-Z case, whereas the NARloy-Z case shows virtually no inelastic strain in this region. Meanwhile, smaller magnitudes of inelastic radial strains are observed in the outer cooling

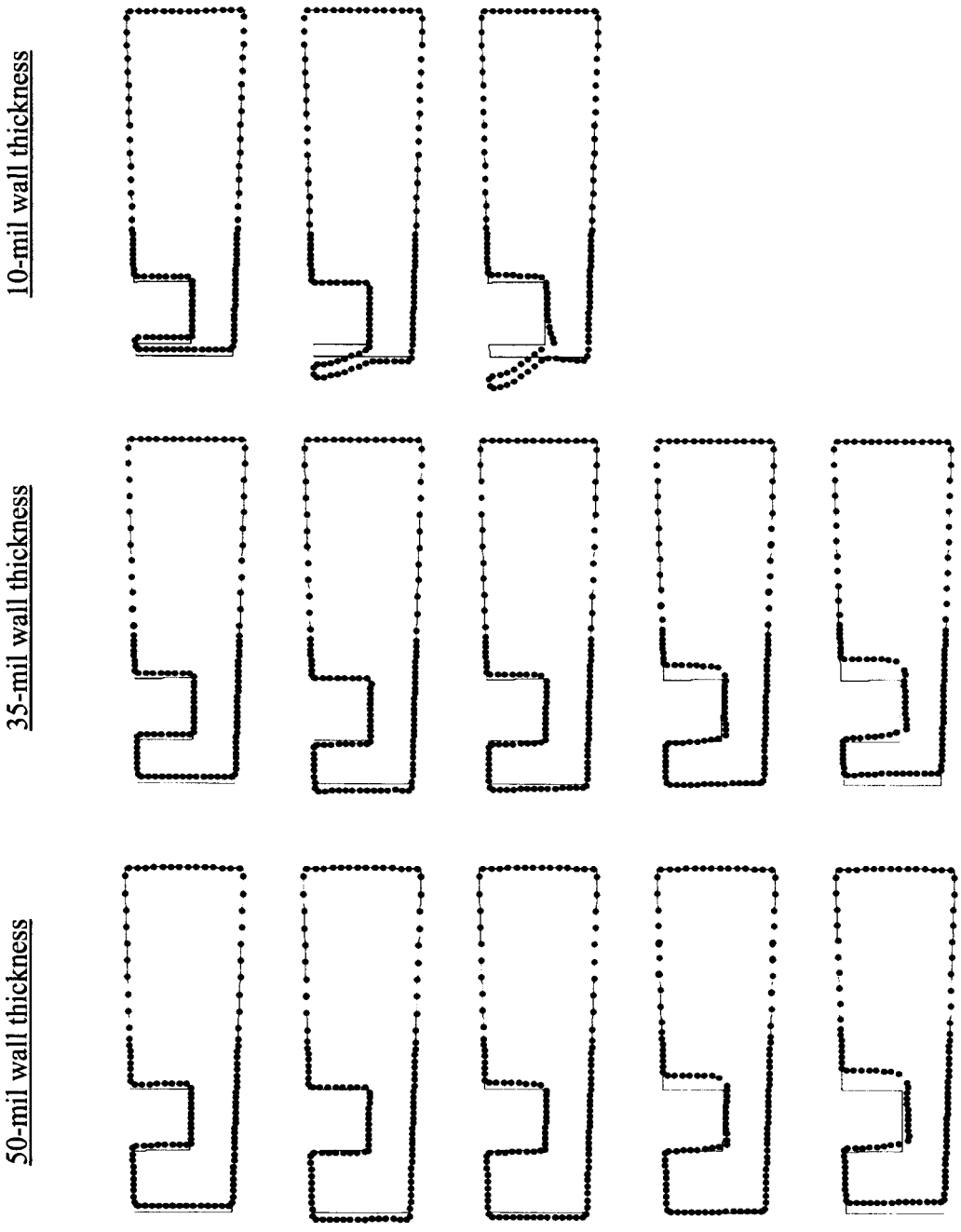

Figure 5.9. Cross-sectional deformation of Cu/NARloy-Z thrust cell liner for small creep exponents at five times during the thermal cycle, t = 1.0, 100, 200, 400 and 500 seconds. Solid lines show undeformed shapes. Dotted lines show deformed shapes with all deformations magnified 5 times.

channel wall of the NARloy-Z cross section compared to the Cu/NARloy-Z cross section, hence the greater thinning of the cooling channel wall in the Cu/NARloy-Z case.

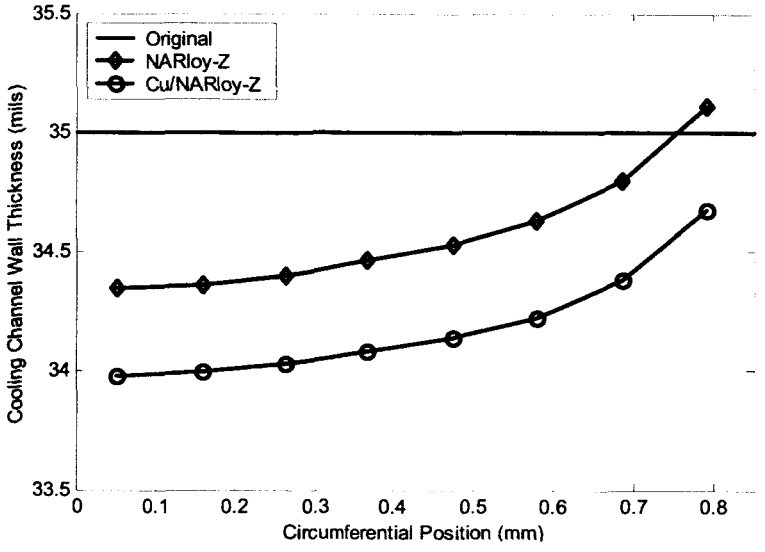

Figure 5.10. Comparison of end-of-cycle cooling channel wall thickness as a function of circumferential position for NARloy-Z and Cu/NARloy-Z cross sections initially employing a 35-mil wall thickness.

5.2.2 Intermediate (n =2.75/3.0) and Large (n=4.0/4.5) Creep Exponents

As was the case in the NARloy-Z analyses, no appreciable deformation is observed after one thermal cycle when the intermediate and large creep exponents are employed in the analysis of 35-mil and 50-mil cooling channel wall thickness geometries, thus these deformed shapes are not shown. As shown in Figure 5.12, appreciable deformations are, however, predicted in the case of the 10-mil cooling channel wall thickness case and the intermediate creep exponent. In contrast to the analysis employing the small creep exponent, the deformations are not of the same magnitude that could lead to structural failure of the cooling channel wall within one thermal cycle. Similar results are observed compared to the analysis of the 10-mil wall thickness NARloy-Z cross sections.

5.3 Effects of Coating Presence and Coating Thickness

Having seen the predicted deformations that can result at severe temperatures, in this section we seek to analyze the effects of adding a protective thermal barrier coating to the previously considered Cu/NARloy-Z cross section. Low-thermal conductivity (see Table 2.3) NiCrAlY coatings of 3 and 6 mils are considered as a means of investigating the effects of coating thickness as well. Additionally, only the 35-mil cooling channel wall thickness configuration and low creep exponents with corresponding creep coefficients previously demonstrated to result in appreciable predicted end-of-cycle deformations are presented herein.

The addition of the NiCrAlY coating results in a considerably different thermal profile in comparison to that observed in the Cu/NARloy-Z configuration. Figure 5.13 shows detailed views of the Cu/NARloy-Z temperature profiles discussed previously, plotted on a new scale, as well as detailed views of the temperature profiles for the 3-mil NiCrAlY coating and the 6-mil NiCrAlY coating. The detailed views are plotted across the entire circumferential width of the cross section and radially from the inner radius of the thrust cell liner to a radius of 37 mm, facilitating much better comparison of temperatures in the coating region. The NiCrAlY coatings, due to their low thermal conductivity relative to NARloy-Z,

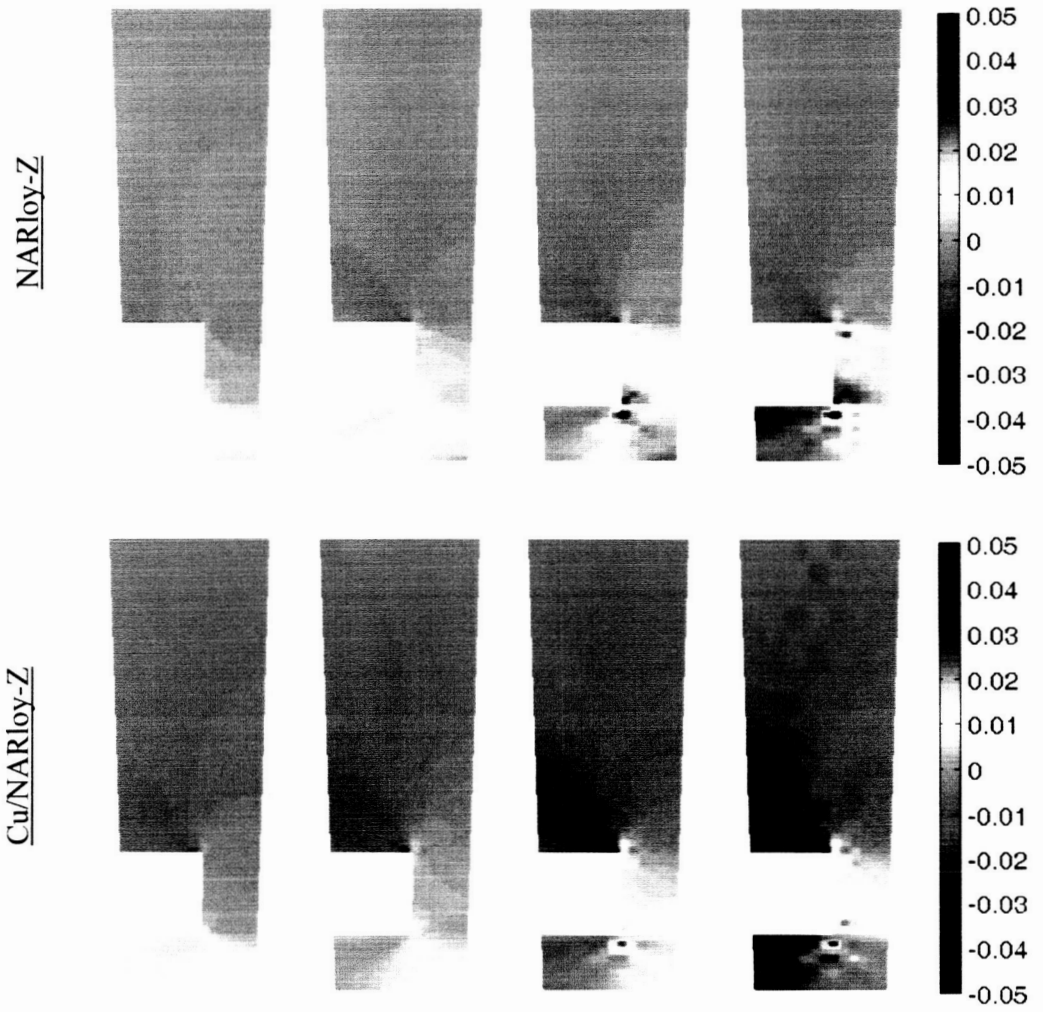

Figure 5.11. Evolution of inelastic radial strain (%) within 35-mil wall thickness NARloy-Z and Cu/NARloy-Z cross sectional liners at four times during the thermal cycle, t = 100, 200, 400 and 500 seconds.

act as thermal barrier coatings within which the temperature field and its gradient attain very large values shown in Figure 5.14. The temperature field within the coating is thus significantly higher than in the inner radius region of the preceding Cu/NARloy-Z configuration. Figure 5.14 also shows that the large temperature gradient across the coating results in reduced temperatures throughout the remaining region of the Cu/NARloy-Z/NiCrAlY configurations. Figure 5.15 demonstrates that the thicker coating acts as a large barrier to heat flow, resulting in an even greater temperature gradient across the coating as well as a greater reduction in temperatures in the NARloy-Z region of this liner configuration. Comparison of the maximum temperatures in the NARloy-Z region of the cross sections provides a direct indication of the true influence of the thermal barrier coatings. In the uncoated Cu/NARloy-Z thrust cell liner, for example, the maximum temperature in the NARloy-Z region is 557 °C, whereas for the cases employing NiCrAlY coatings of 3 and 6 mils the corresponding maximum temperatures in the NARloy-Z region are 482 °C and 421 °C, respectively. Clearly the thicker coating has greater thermal protection capabilities as

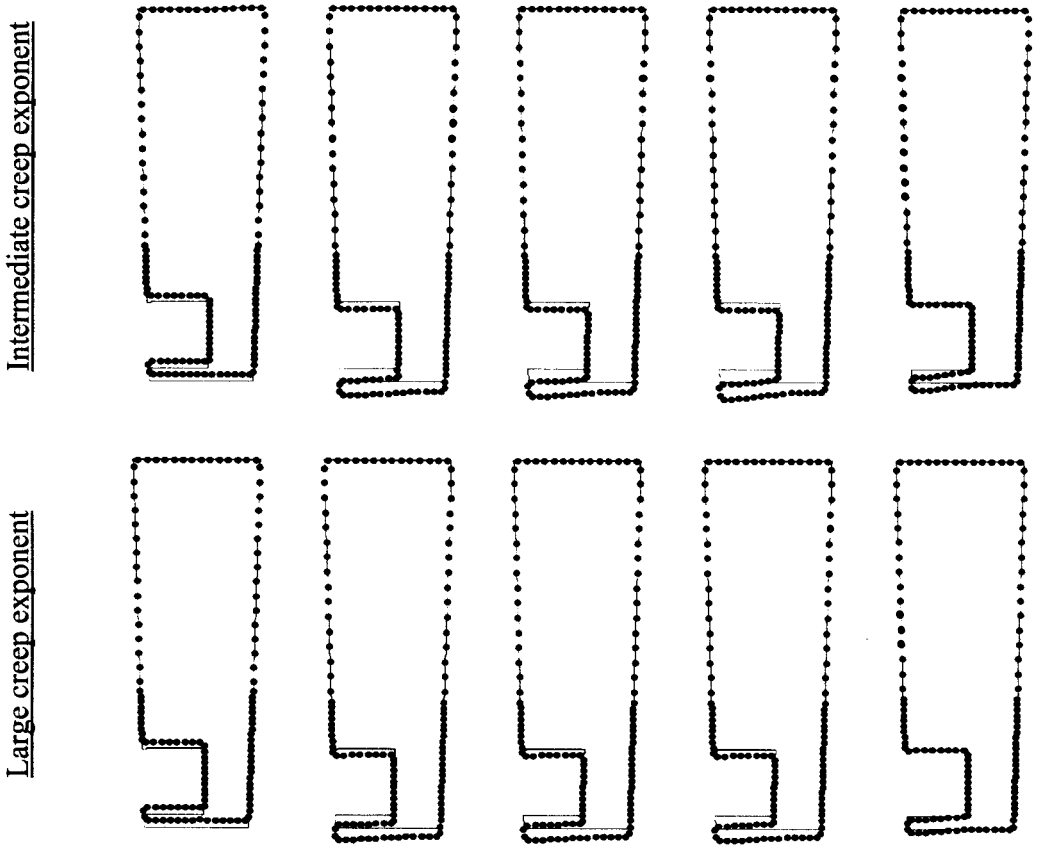

Figure 5.12. Cross-sectional deformation of Cu/NARloy-Z thrust cell liner for intermediate and large creep exponents at five times during the thermal cycle, t = 1.0, 100, 200, 400 and 500 seconds. Solid lines show undeformed shapes. Dotted lines show deformed shapes with all deformations magnified 5 times.

it produces a larger temperature reduction in the NARloy-Z region. The maximum temperature in the NARloy-Z region of the 6-mil NiCrAlY coating case is reduced by 136 °C compared to the uncoated Cu/NARloy-Z case. Such a dramatic reduction in temperature exposure is also likely to limit creep-induced deformation, therefore eliminating the previously observed "dog-house" type deformation mode.

Deformations corresponding to the three sets of temperature fields for the small creep exponent case are shown in Figure 5.16. Relative to the Cu/NARloy-Z configuration shown in the first row, the extent of thinning of the cooling channel wall is reduced for the cases shown in rows two and three in which a coating is employed. This result is shown much more clearly in Figure 5.17, which presents the predicted cooling channel wall thickness of each configuration as a function of circumferential position. The two figures are a clear demonstration of the promise associated with thermal barrier coatings as the coatings serve to protect the structural NARloy-Z alloy from temperature magnitudes observed in the uncoated thrust cell liner, thereby limiting thinning of the cooling channel wall. In addition to the deformation behavior noted in the cooling channel wall, deformation is also observed at the rear of the cooling channel. Though not critical in terms of failure, this deformation does persist and is perhaps even

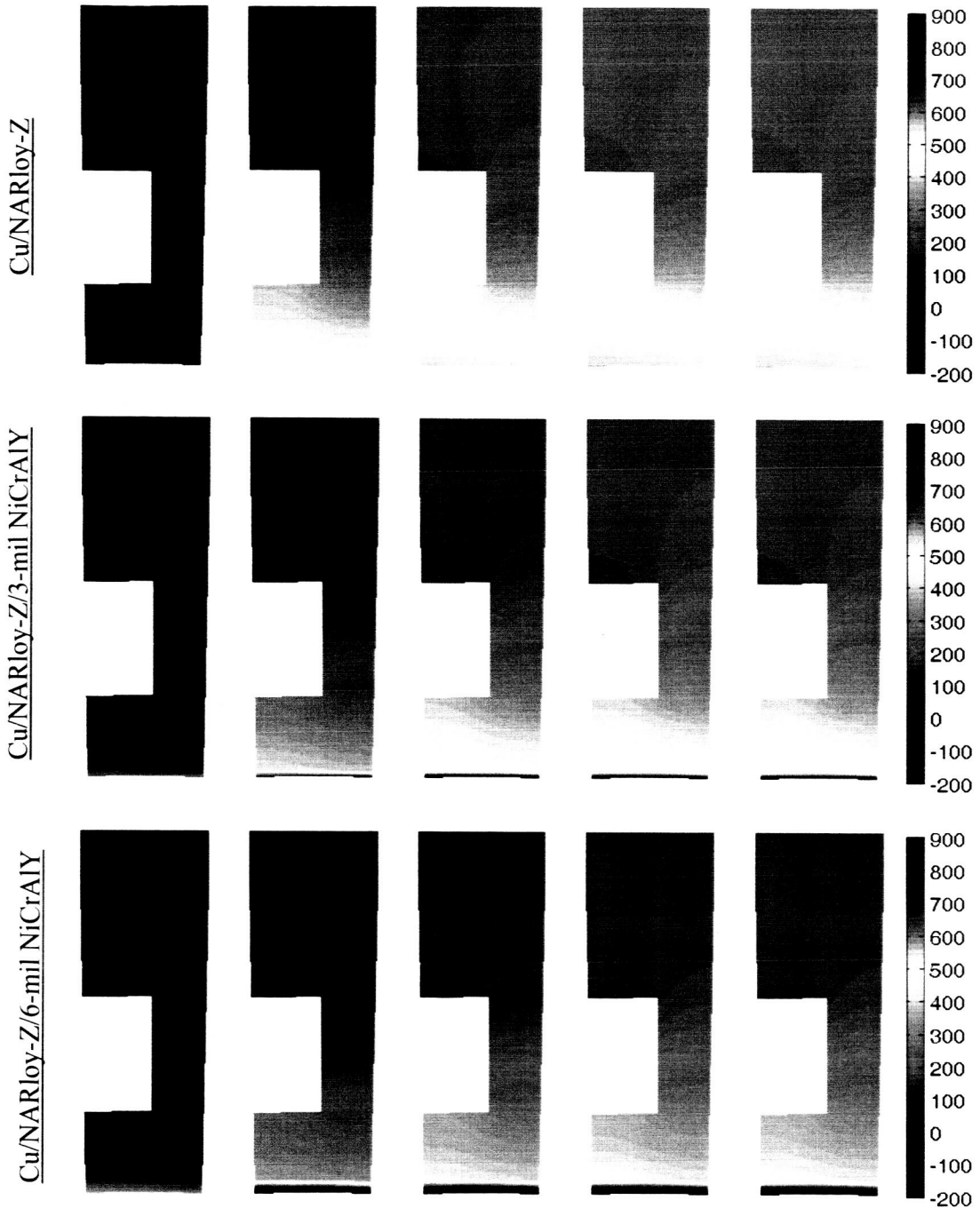

Figure 5.13. Detailed view of temperature evolution (^{0}C) within Cu/NARloy-Z cross-sectional liner, Cu/NARloy-Z/NiCrAlY cross-sectional liner with 3-mil coating and Cu/NARloy-Z/NiCrAlY cross-sectional liner with 6-mil coating at five times during the thermal cycle, t = 1.5, 2.0, 2.5, 5.0 and 10.0 seconds.

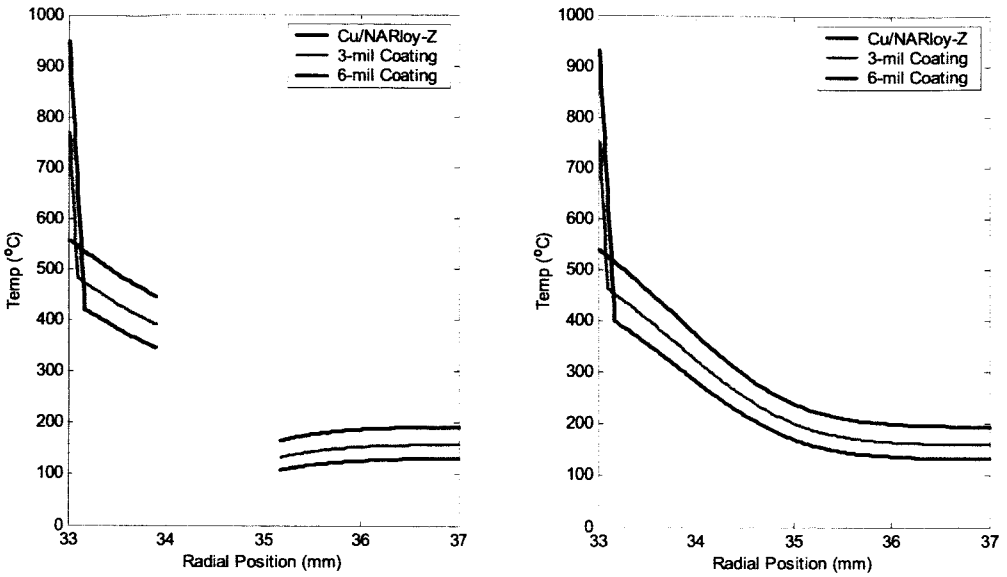

Figure 5.14. Steady-state temperature distributions along the left and right radial edges of the cross section for Cu/NARloy-Z, Cu/NARloy-Z/NiCrAlY (3-mil coating) and Cu/NARloy-Z/NiCrAlY (6-mil coating) thrust cell liners.

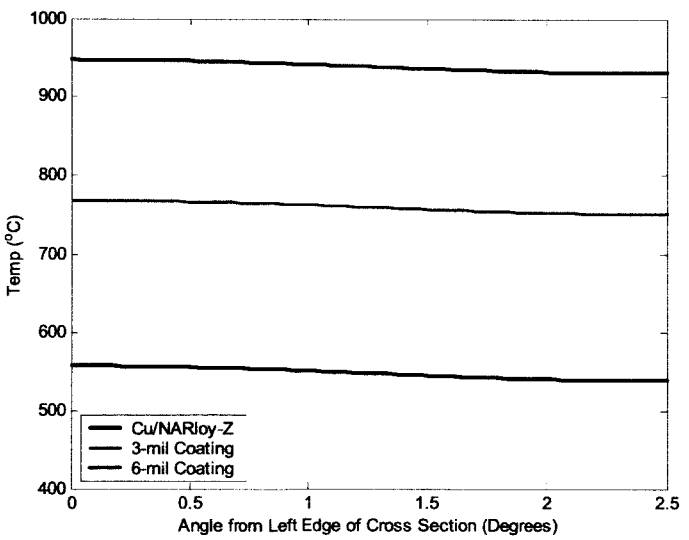

Figure 5.15. Steady-state temperature distributions along the inner radius of the cross section for Cu/NARloy-Z, Cu/NARloy-Z/NiCrAlY (3-mil coating) and Cu/NARloy-Z/NiCrAlY (6-mil coating) thrust cell liners.

magnified in the presence of the NiCrAlY coating. Deformation in this region may, however, be particular concern to engine designers as enlargements of the cooling channel could result in varying flow characteristics of the pressurized coolant.

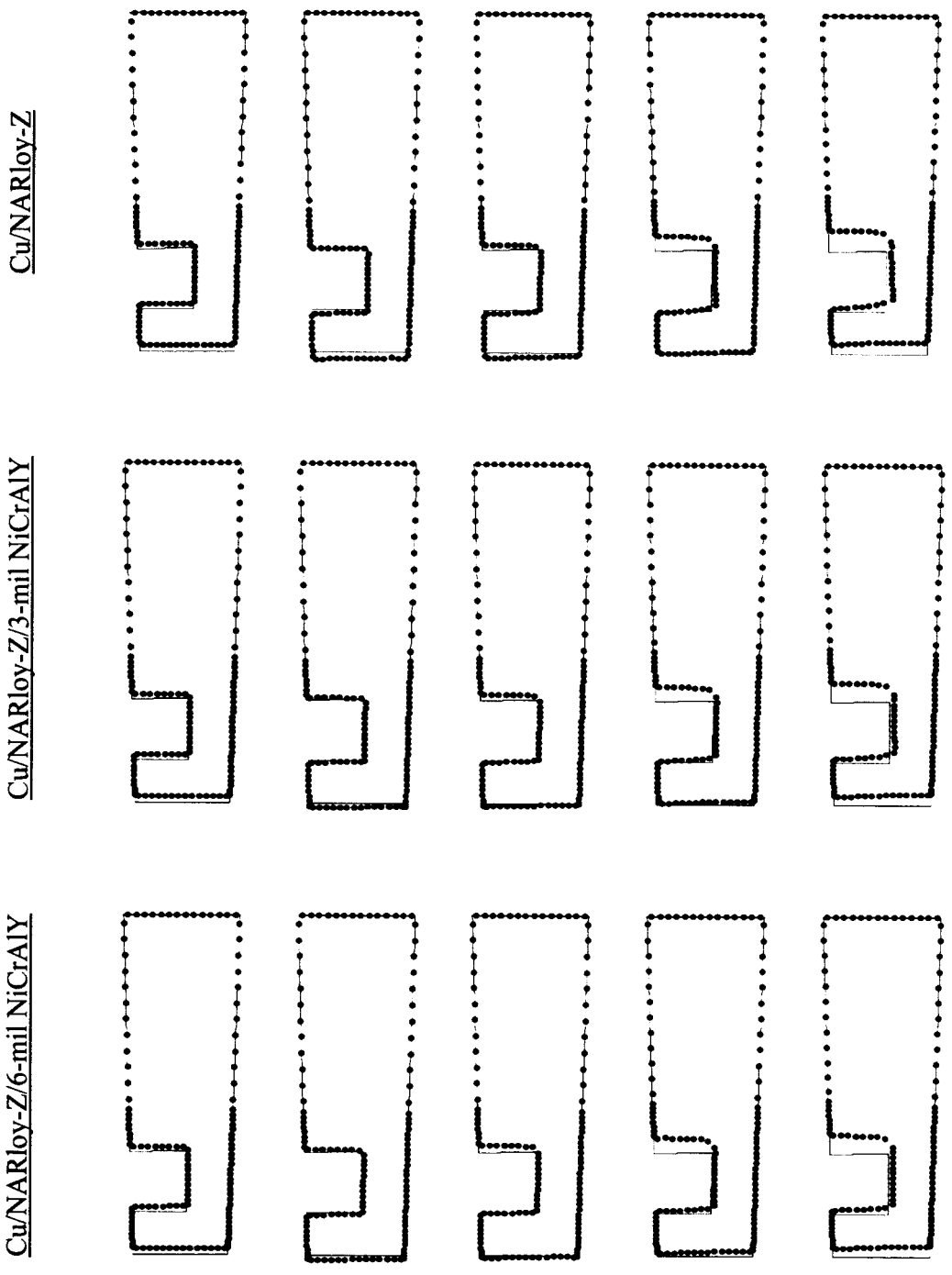

Figure 5.16. Cross-sectional deformation of thrust cell liners for small creep exponents at five times during the thermal cycle, t = 1.0, 100, 200, 400, 500 seconds. Solid lines show undeformed shapes. Dotted lines show deformed shapes with all deformations magnified 5 times.

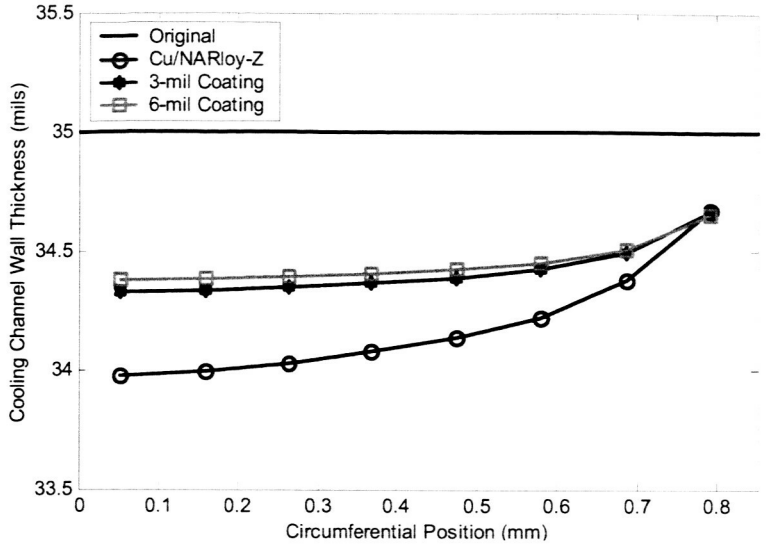

Figure 5.17. Predicted cooling channel wall thickness as a function of circumferential position for analyses of Cu/NARloy-Z liner; Cu/NARloy-Z/NiCrAlY liner with 3-mil coating and Cu/NARloy-Z/NiCrAlY liner with 6-mil coating, all employing small creep exponent.

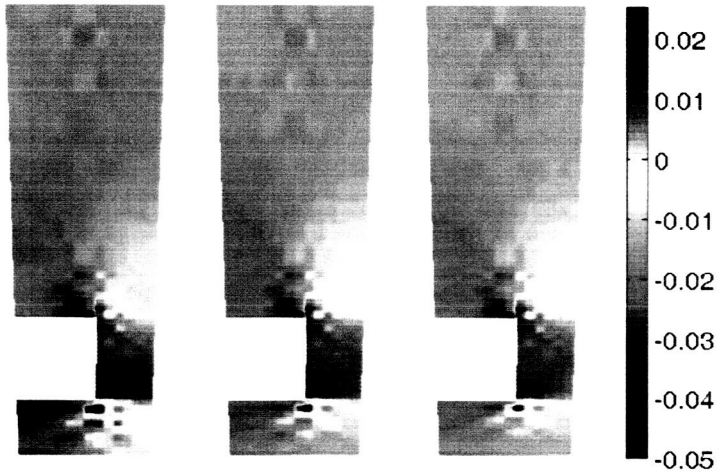

Figure 5.18. Comparison of the end-of-cycle inelastic radial strains within the three liner cross sections: Cu/NARloy-Z (left), Cu/NARloy-Z/NiCrAlY with 3-mil coating (center) and Cu/NARloy-Z/NiCrAlY with 6-mil coating (right).

Figure 5.18 compares the end-of-cycle inelastic radial strain fields for each of the three configurations discussed in the context of temperature and deformation fields. The inelastic radial strains for the two cases in which a NiCrAlY coating has been employed further illustrate the impact of the thermal barrier coatings. The magnitudes of the inelastic radial strains are significantly reduced compared to those observed in the Cu/NARloy- Z, particularly in the region of the cooling channel wall.

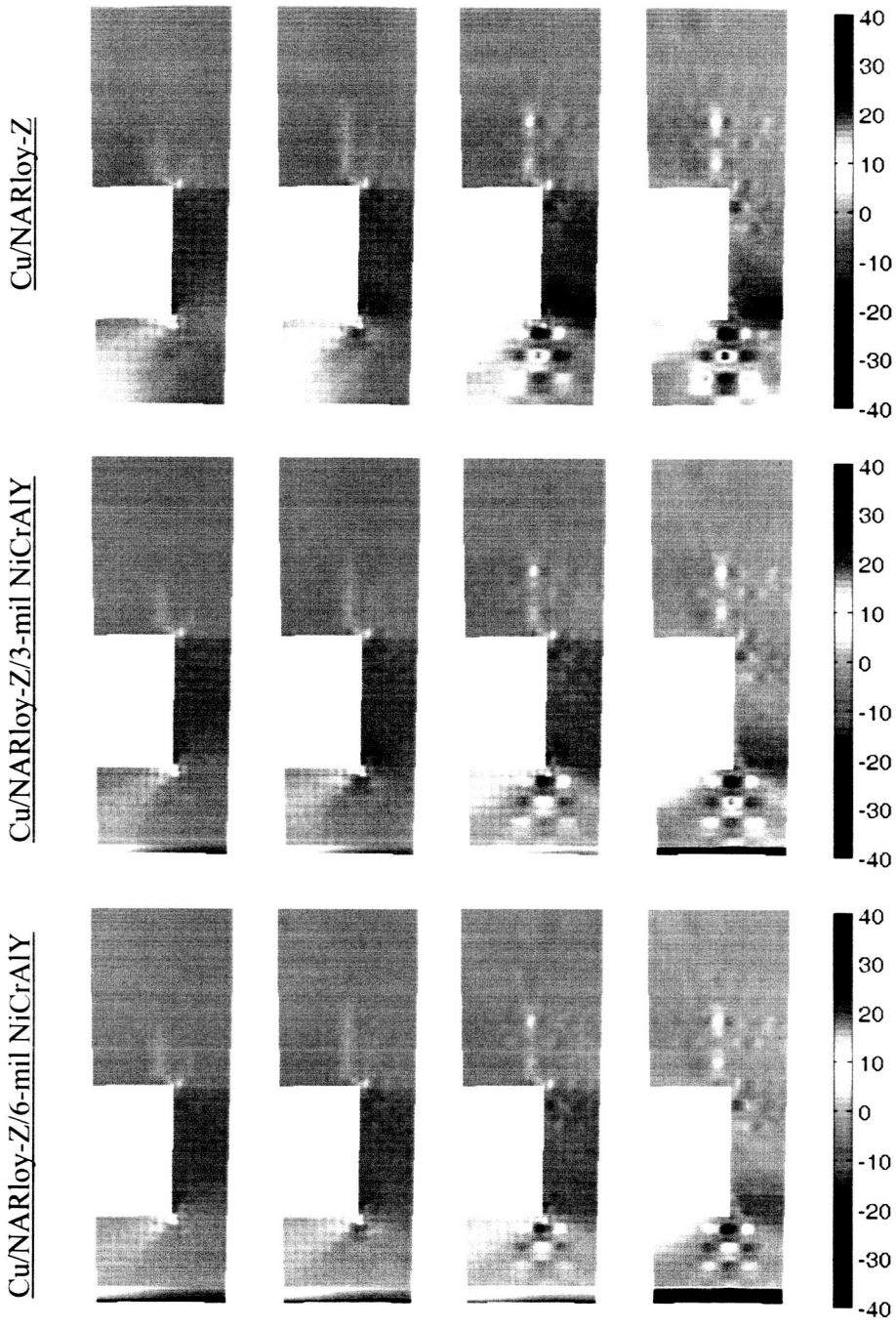

Figure 5.19. Circumferential stress evolution within the three liner cross sections at four times during the thermal cycle: t = 100, 200, 400 and 500 seconds (colorbar in MPa).

Keeping in mind the thermo-mechanical property mismatch between NiCrAlY and NARloy-Z, and the severe thermal gradient discussed previously, the potential problem of coating degradation/failure also necessitates a closer examination of the stress distributions throughout the cross section of the coating and the immediate vicinity. These stresses also add an additional complication when the thermal

cycle transitions from the hold period through a forced cool down phase. As this happens, the stress state can be quickly reversed from highly tensile to highly compressive or visa-versa at many points. Despite the fact that the 6-mil NiCrAlY coating case has been shown to produce the most desirable results in terms of deformations, a further analysis of the stresses induced by the severe gradient observed in a coating of this thickness may eliminate this coating thickness as a feasible option.

Figure 5.19 shows a detailed view (across the entire circumferential width of the cross section and radially from the inner radius of the thrust cell liner to a radius of 37 mm) of the evolution of the circumferential stresses in the Cu/NARloy-Z configuration as well as the two configurations in which coatings are employed. This figure clearly shows the impact the coating has on the circumferential stress component, particularly at the inner radius of the thrust cell liner and within the cooling channel wall. In the uncoated thrust cell liner, for example, the largest magnitude of circumferential stress appears in the cooling channel wall at the end of the cycle. Applying a coating, however, is shown to reduce the magnitude of these stresses in the cooling channel wall while amplifying these stresses within the coating along the inner radius of the thrust cell liner cross section. We note that the "checkerboard" effect observed in these contours, particularly the case of the uncoated liner, could be minimized or smoothed out through further mesh refinement. The radial stress component for these three configurations (not shown) is virtually unaffected by the application of the thermal barrier coatings. Taken together, the radial and circumferential stress components are of significant magnitude that they could induce failure in the presence of porosities or other impurities.

5.4 Effect of Grading

5.4.1 Homogenization-Based Analysis

Thermal profiles for the graded cases employing homogenized layers based on the effective properties determined in conjunction with the cubical inclusions of Section 4 are presented in Figure 5.20. The case employing a 6-mil NiCrAlY coating with a sharp interface to the NARloy-Z substrate material contains the same volume of NiCrAlY as the case employing the 3-mil NiCrAlY coating applied in conjunction with the graded region (see Figure 2.2). The same is true for the 3-mil NiCrAlY coating without grading and the 1.5-mil NiCrAlY coating employed in conjunction with the homogenized graded region, thus these cases provide a direct demonstration of the impact this type of grading has on temperature fields. The results show that, for the same volume of NiCrAlY, the application of grading has effectively reduced the severe radial thermal gradient previously observed in the context of the ungraded coating systems shown in Figure 5.13. It has also reduced the predicted maximum temperatures at the inner radius of the thrust cell liner.

The cross sectional radial thermal gradients for the graded and ungraded coating systems are shown in Figure 5.21, while the predicted temperatures along the inner radius of each thrust cell liner configuration are shown in Figure 5.22. In the case of the thicker NiCrAlY coating, the reduction of temperature at the inner radius of the thrust cell liner is particularly noticeable. When no grading is employed with a 6-mil NiCrAlY coating, the predicted maximum temperature is approximately 950 °C, whereas in the case where the NiCrAlY is redistributed by grading the maximum temperature is approximately 875 °C, thus the application of grading has resulted in a reduction of the maximum exposure temperature by approximately 75 °C. Conversely, the maximum temperature experienced in the NARloy-Z region of each thrust cell liner configuration increases in the presence of homogenized grading. In the case of the 6-mil NiCrAlY coating, the maximum temperature in the NARloy-Z region was noted in Section 5.3 as 421 °C. Redistributing the NiCrAlY material and homogenizing the graded layers, however, results in maximum NARloy-Z exposure temperatures of 435 °C for the respective volume of NiCrAlY. Similar results are also observed for the thinner coating cases with a smaller decrease in the temperature at the inner radius and thus a slightly more substantial increase in maximum

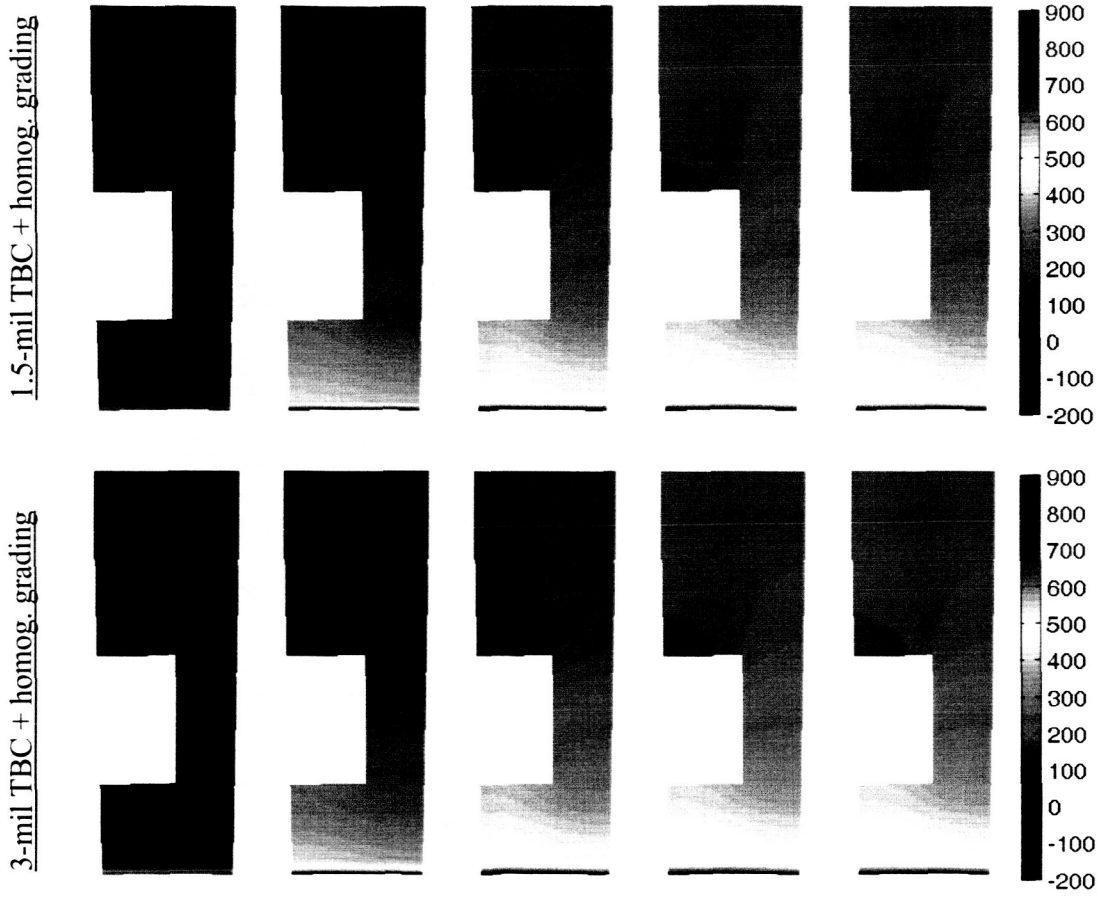

Figure 5.20. Detailed view of temperature evolution (^{0}C) within the cross sections of Cu/NARloy-Z/NiCrAlY (1.5 mils + homogenized grading) and Cu/NARloy-Z/NiCrAlY (3 mils + homogenized grading) liners at five times during the thermal cycle, t = 1.5, 2.0, 2.5, 5.0 and 10.0 seconds.

NARloy-Z exposure temperature. Such increases in temperature within the NARloy-Z region of the thrust cell liner may potentially result in slightly increased deformation by creep, thereby promoting the "dog-house" type deformation mode.

Figure 5.23, however, shows that such changes in temperature do not result in substantially more severe deformation fields after one cycle. The end-of-cycle deformed shapes presented for the two different coating thicknesses for both ungraded and graded coating systems do not show obvious differences between the four configurations. Small differences, however, are noted in Figure 5.24, which shows the predicted cooling channel wall thickness as a function of circumferential position for each of the four analyses. Comparing ungraded and graded coating systems separately on the basis of coating thickness indicates that increasing the coating thickness does not necessarily result in less thinning of the cooling channel wall as demonstrated in Section 5.3. Comparing ungraded and graded coating systems against one another on the basis of the volume of NiCrAlY employed in the cross section shows that cooling channel wall thinning is not only a function of the volume of NiCrAlY employed, but also the manner in which it is employed since for the same volume of NiCrAlY the results differ slightly in the case of the thicker graded and ungraded coatings.

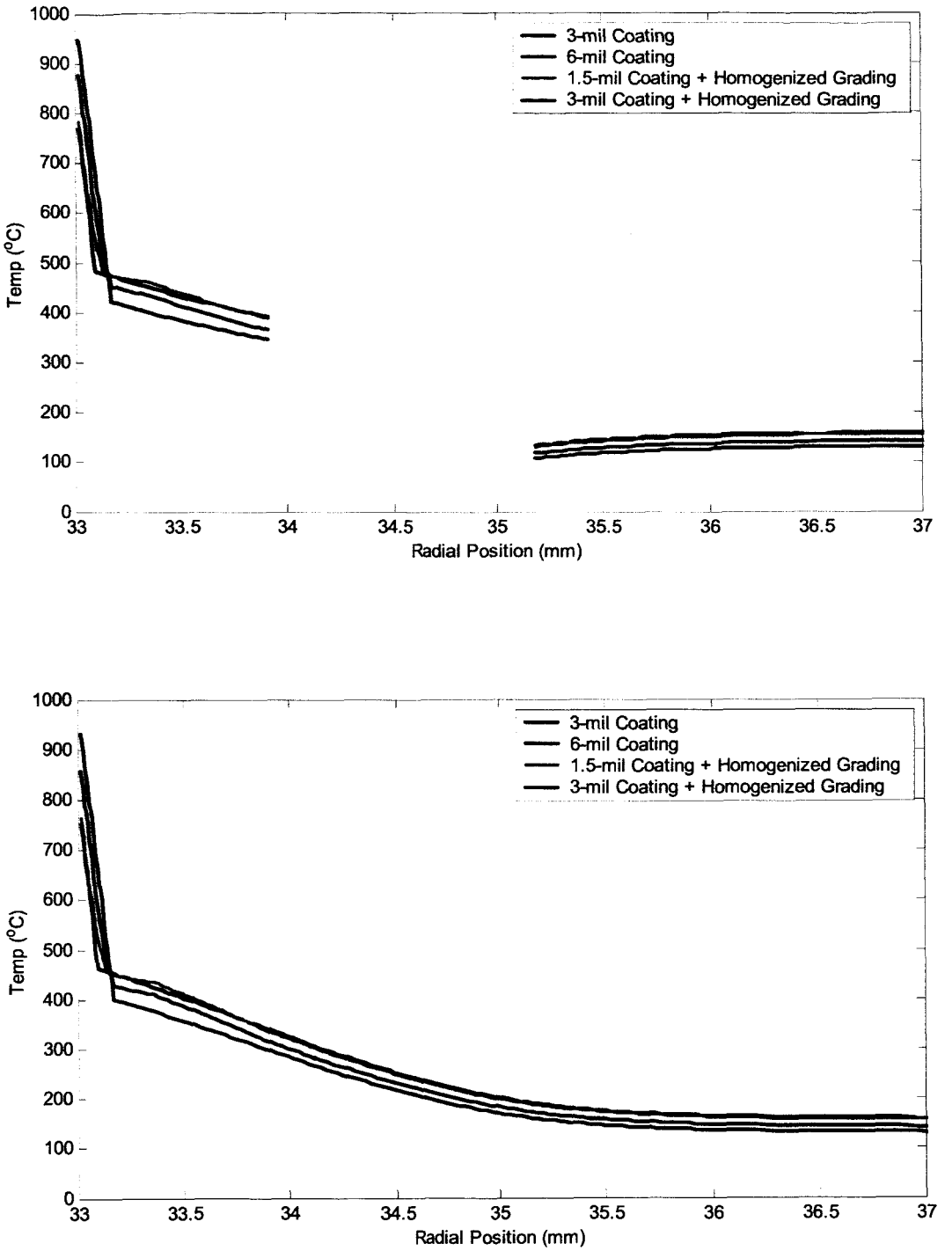

Figure 5.21. Comparison of steady-state temperature distributions along the left (top) and right (bottom) radial edges of the cross section for graded and ungraded thrust cell liner configurations employing thermal barrier coatings.

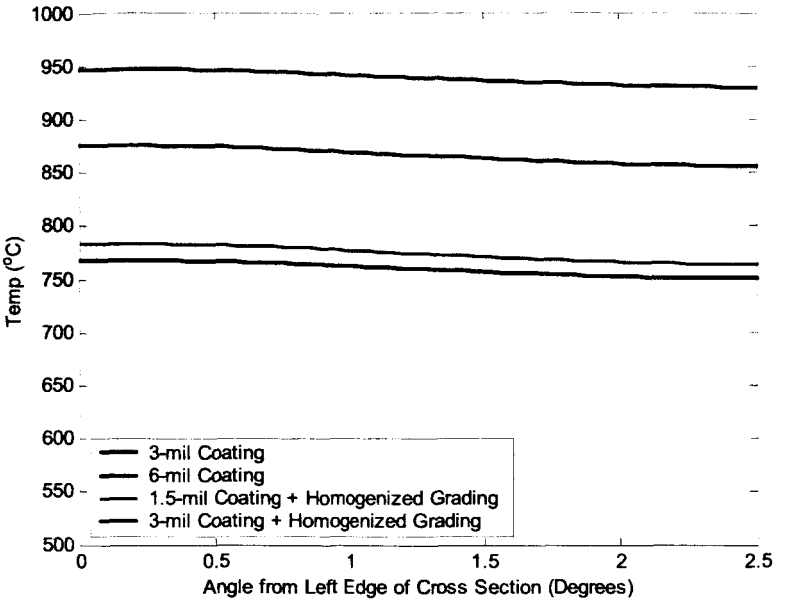

Figure 5.22. Comparison of steady-state temperature distributions along the inner radius of the cross section for graded and ungraded thrust cell liner configurations employing thermal barrier coatings.

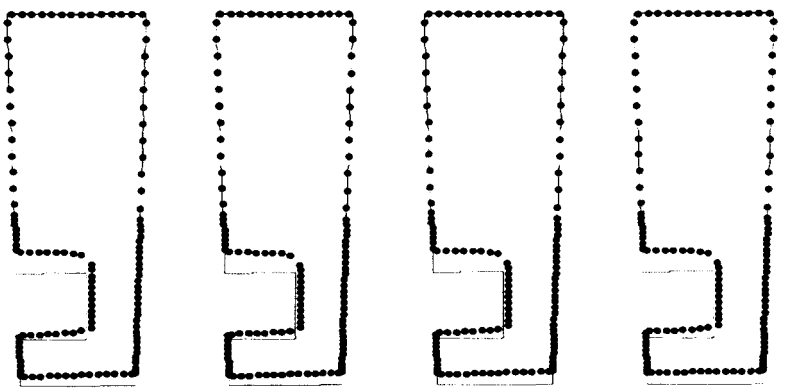

Figure 5.23. Cross-sectional deformation of (left to right) Cu/NARloy-Z/NiCrAlY (3 mils); Cu/NARloy-Z/NiCrAlY (6 mils); Cu/NARloy-Z/NiCrAlY (1.5 mils + homogenized grading) and Cu/NARloy-Z/NiCrAlY (3 mils + homogenized grading) thrust cell liners at end of the thermal cycle. Solid lines show undeformed shapes. Dotted lines show deformed shapes with all deformations magnified 5 times.

Figure 5.25 is presented to demonstrate the impact of homogenized grading on the circumferential stress fields shown earlier in Figure 5.19 for the ungraded cases. Comparing the two figures, little change is noted in the overall stress field. The application of homogenized grading does reduce the area within which maximum stresses occur, as a smoothing effect is seen between the stresses in the coating and the stresses in the substrate in the graded case. This effect, however, is not substantial enough to conclude that grading may improve thrust cell liner performance or durability. Radial stresses

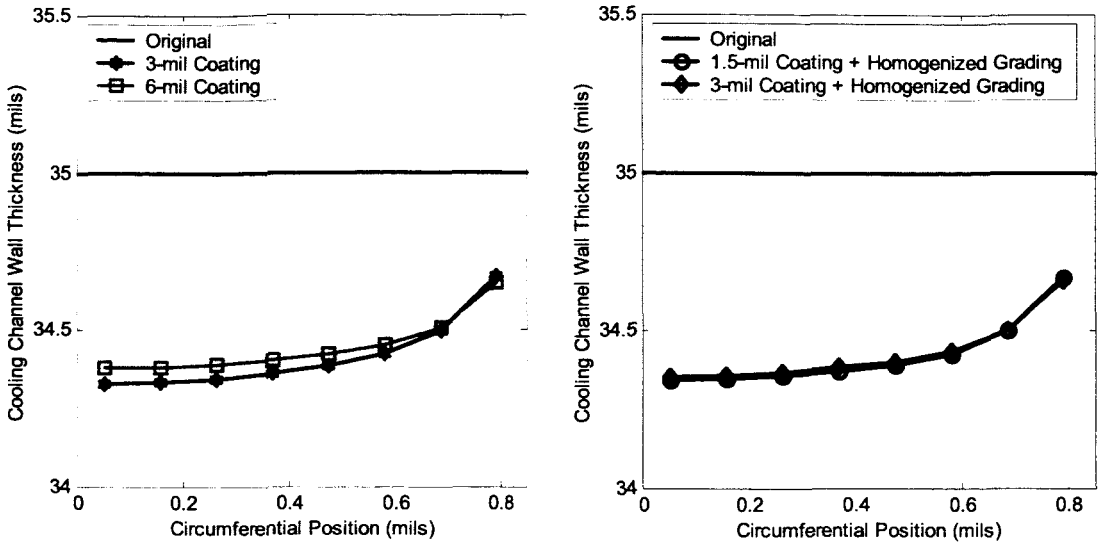

Figure 5.24. Predicted cooling channel wall thickness as a function of circumferential position for analyses of Cu/NARloy-Z/NiCrAlY liner with 3-mil coating and Cu/NARloy-Z/NiCrAlY liner with 6-mil coating (left) and Cu/NARloy-Z/NiCrAlY liner with 1.5-mil coating + homogenized grading and Cu/NARloy-Z/NiCrAlY liner with 3-mil coating + homogenized grading (right).

and inelastic radial strains for the graded and ungraded thrust cell liners cases are essentially identical, and therefore are not shown.

5.4.2 Actual Microstructure-Based Analysis

Thermal profiles for the graded cases employing actual microstructural details (see Figure 2.2) are presented in Figure 5.26. As in the case of homogenized grading, the case employing a 6-mil NiCrAlY coating with a sharp interface to the NARloy-Z substrate material contains the same volume of NiCrAlY as the case employing the 3-mil NiCrAlY coating applied in conjunction with the discretely graded region. Likewise, the 3-mil NiCrAlY coating without grading and the 1.5-mil NiCrAlY coating employed in conjunction with the discretely graded region contain the same volume of NiCrAlY.

Modeling actual microstructural details using HOTCFGM, as opposed to employing the effective properties predicted by GMC-3D, is shown to result in slightly different temperature fields. Most notably, the results presented in Figure 5.26 do not exhibit the same smoothness associated with the results presented earlier for the homogenized grading in Figure 5.20. The smoothness observed in Figure 5.20 arises from the application of homogenization which effectively eliminated the local variation of thermoelastic properties within a given graded layer. In contrast, the application of discrete grading fully accounts for such local variation within the context of the macro-scale analysis, thus the local variation in the temperature field.

The cross-sectional radial thermal gradients for the coating systems with homogenized and actual microstructural details are shown in Figure 5.27, while the predicted temperatures along the inner radius of each configuration are shown in Figure 5.28. In each respective case, the actual microstructure produces a slightly increased average exposure temperature of NiCrAlY and a reduced exposure temperature for NARloy-Z. The actual microstructure-based analysis, however, also captures the local

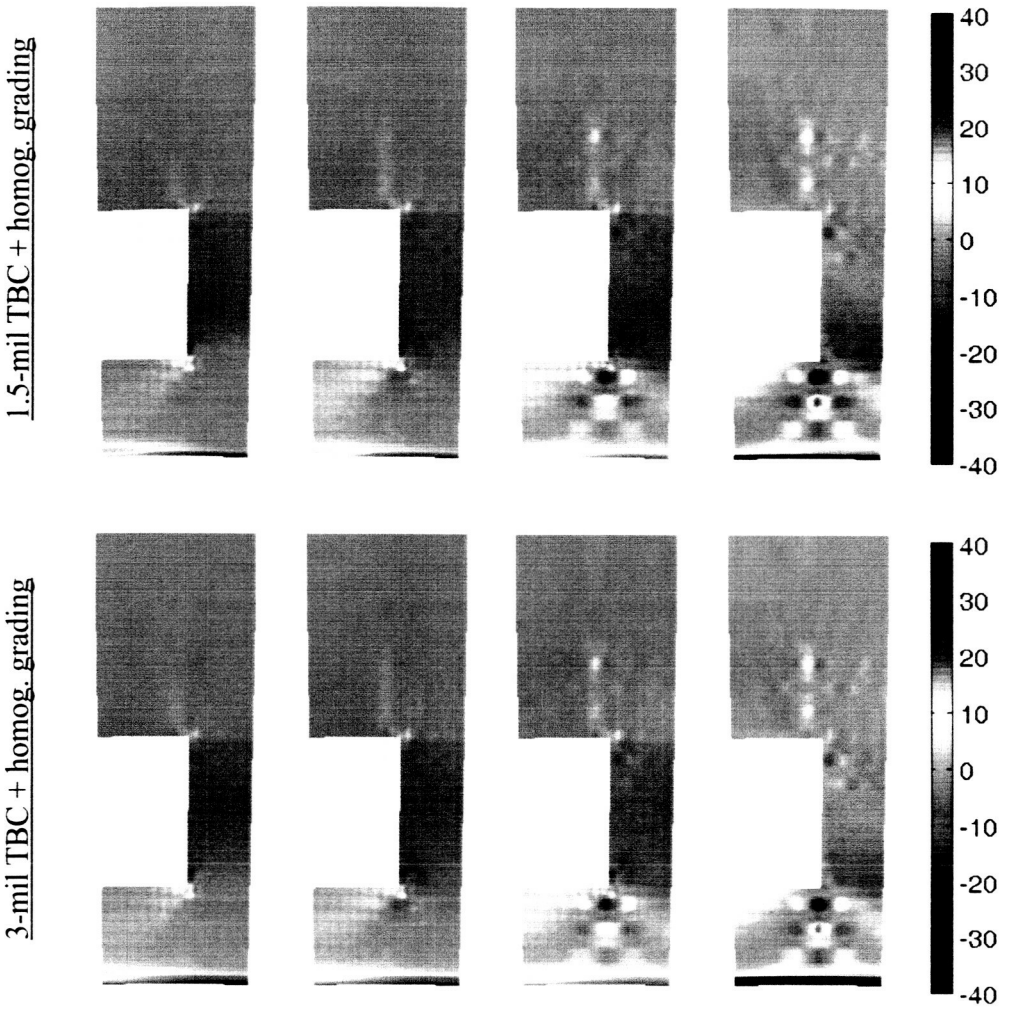

Figure 5.25. Detailed view of the evolution of circumferential stress within cross sectional liners of Cu/NARloy-Z/NiCrAlY with 1.5-mil coating and homogenized grading and Cu/NARloy-Z/NiCrAlY with 3-mil coating and homogenized grading at four times during the thermal cycle, t = 100, 200, 400 and 500 seconds. Scale in MPa.

maxima and minima within the temperature field. The differences in the two analyses demonstrate the shortcomings associated with the homogenized analysis of functionally graded materials, which cannot simultaneously predict accurate local and global fields or account for interactions between distinct phases.

Figure 5.29 illustrates the effect of local hot spots, captured by the analysis based on the actual microstructural details, on the predicted thinning of the cooling channel wall. Much more irregular variation of the cooling channel wall thickness is predicted as a function of circumferential position when discrete inclusions are employed in the analysis, as the increased local temperatures around the inclusions result in localized, irregular deformations not observed in the homogenized approach. Two factors are attributed to the increased deformation. First, as temperatures increase more creep-induced deformation

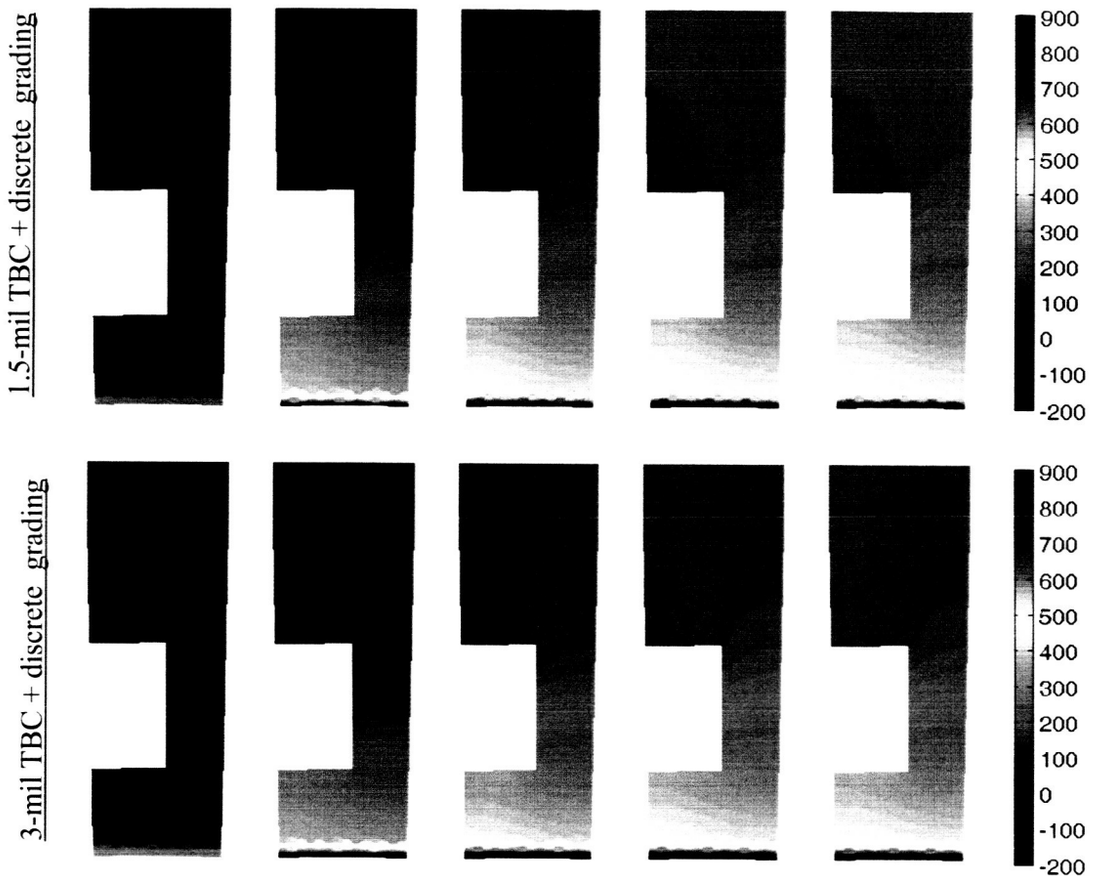

Figure 5.26. Detailed view of temperature evolution (^{0}C) within Cu/NARloy-Z/NiCrAlY (1.5 mils + discrete grading) cross-sectional liner and Cu/NARloy-Z/NiCrAlY (3 mils + discrete grading) cross-sectional liner at five times during the thermal cycle, t = 1.5, 2.0, 2.5, 5.0 and 10.0 seconds.

is expected. Second, the increased temperatures combined with the large coefficient of thermal expansion mismatch between NARloy-Z and NiCrAlY phases result in large interfacial stresses, thereby increasing the effective stress and further contributing to the creep-induced deformation. These effects are evident in Figure 5.30, which provides a comparison of the inelastic radial strains predicted by the homogenization-based and actual microstructure-based approaches. As observed in this figure, greater local inelastic strains occur in the region near the inclusions in the analysis based on the actual microstructure. These results do not point to a clear advantage of functional grading over a homogenous NiCrAlY TBC, although reducing the size of the inclusions (modeled as approximately 40 μm in the radial direction, 100 μm in the circumferential direction and 250 μm in the thickness direction) would influence the effects of particle-particle as well as particle-surface interaction. In summary, these results demonstrate that employing homogenization to analyze the graded region can lead to misleading results.

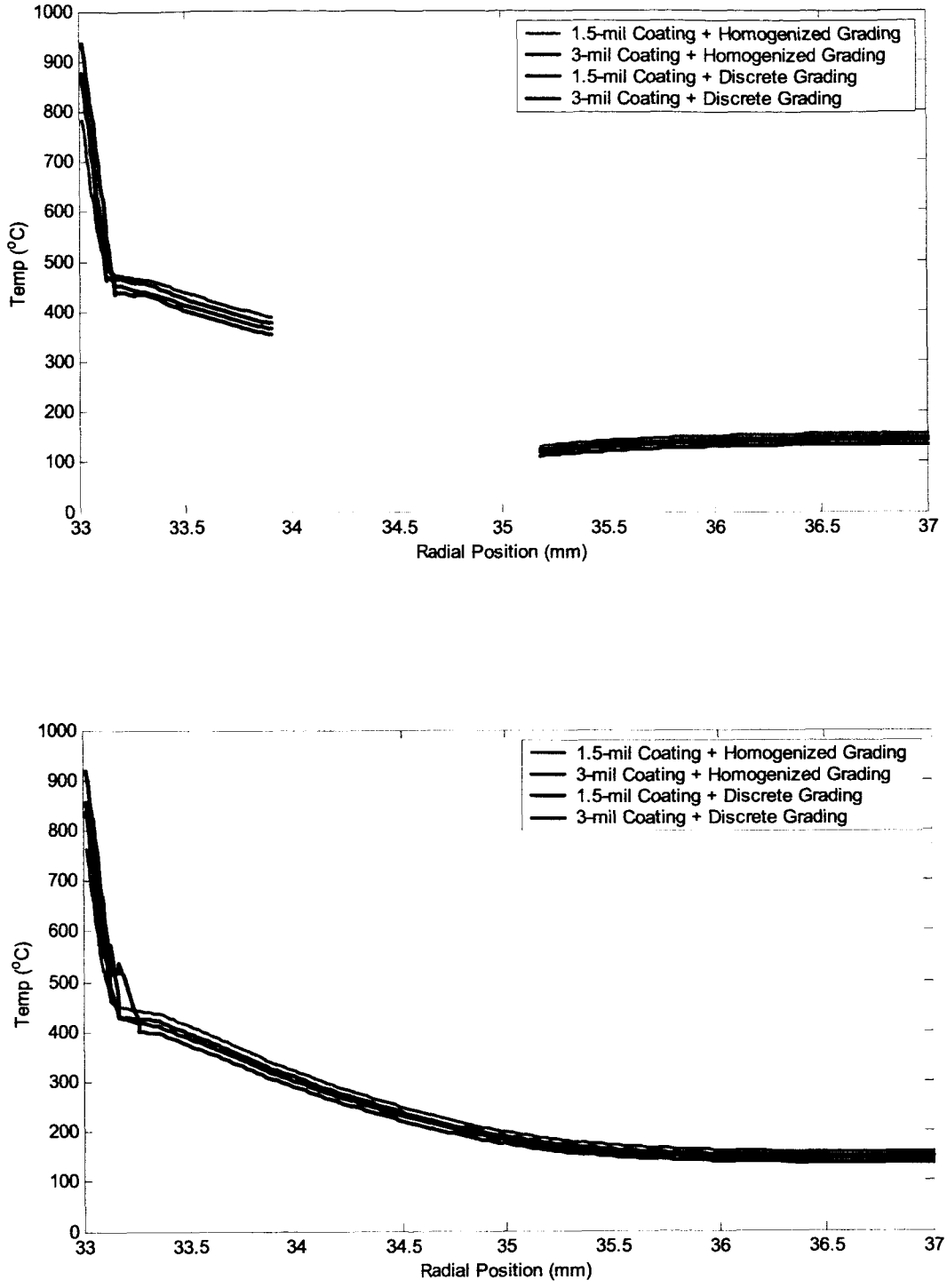

Figure 5.27. Steady-state temperature distributions along the left (top) and right (bottom) radial edges of the cross section for graded thrust cell liners configurations analyzed employing the homogenized and discrete grading approaches.

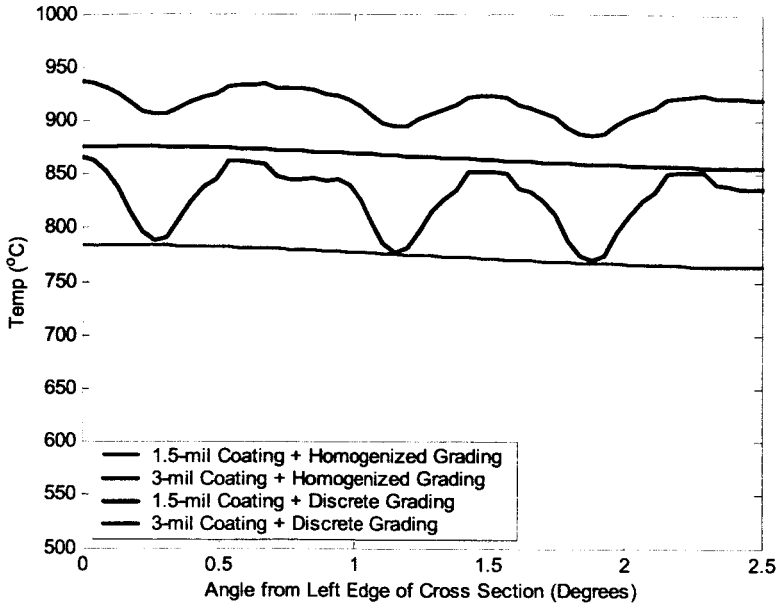

Figure 5.28. Steady-state temperature distributions along the inner radius of the cross section for graded thrust cell liners configurations analyzed employing the homogenized and discrete grading approaches.

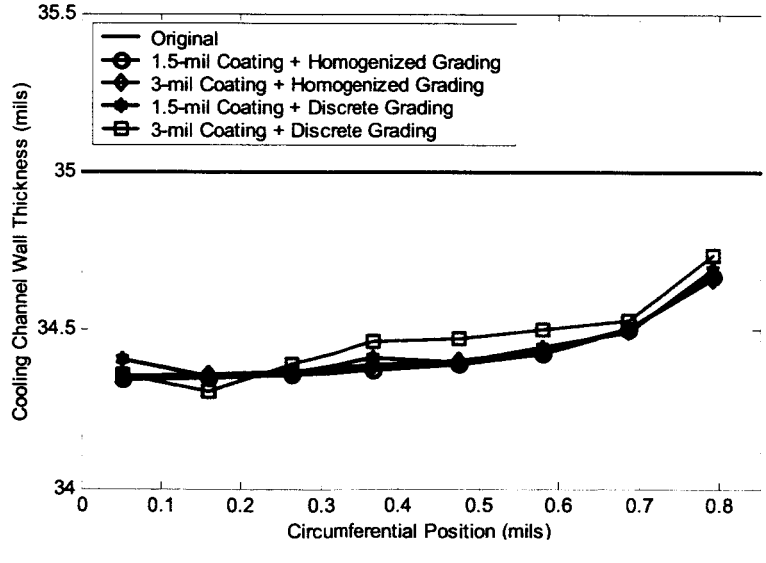

Figure 5.29. Predicted cooling channel wall thickness as a function of circumferential position for graded thrust cell liners configurations analyzed employing the homogenized and discrete grading approaches.

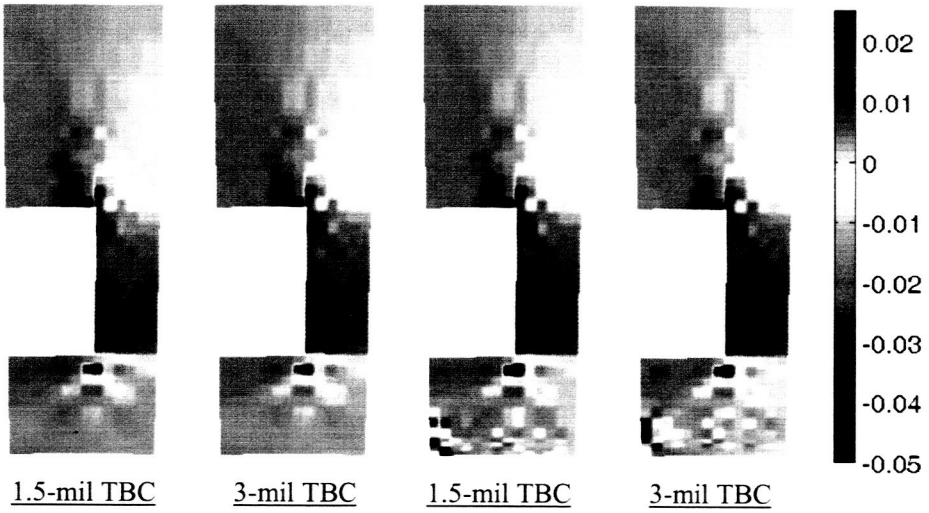

Figure 5.30. Comparison of end-of-cycle radial inelastic strains for graded thrust cell liners configurations analyzed using the homogenized (left pair) and discrete (right pair) grading approaches.

6 Summary, Conclusions and Future Work

An extensive study of the factors affecting RLV thrust cell liner performance has been successfully conducted using the cylindrical version of the higher order theory for functionally graded composites. A number of significant results have been attained in this work. These results are listed below in Section 6.1 and the conclusions drawn from them are discussed in Section 6.2.

6.1 Summary of Results

- HOTCFGM predictions based on the Robinson model were generally in agreement with the predictions presented by previous investigators based on the finite-element method. The coarse mesh employed by the previous investigators, however, casts doubt on the convergence of these results and makes a detailed comparison of results difficult. Additionally, the Robinson model was shown to be very computationally expensive.
- Deformed shapes predicted by HOTCFGM based on the Robinson and power-law creep models were compared to each other and to the results obtained by previous investigators in the context of multiple short-cycle loading history. This comparison revealed some differences between the two material models. Specifically, the Robinson model results were shown to predict bulging of the cooling channel wall, but failed to predict thinning of the cooling channel wall at the circumferential centerline of the cooling channel. The power-law creep model, on the other hand, predicted the experimentally observed bulging and thinning of the cooling channel wall, while also providing much improved computational efficiency.
- The conclusion of previous investigators that the characteristic deformation, that is bulging and thinning of the cooling channel wall, of NARloy-Z thrust cell liners is driven, at least in part, by the biasing pressure differential across the cooling channel wall has been investigated. This investigation was conducted in the context of a HOTCFGM analysis employing the power-law creep model and the multiple short cycle analysis. In the absence of an applied pressure differential across opposite parallel faces of the cooling channel wall, significantly less bulging and thinning of the cooling

channel wall was predicted. Furthermore, the predicted deformations were similar in nature to those obtained from the HOTCFGM analysis based on the Robinson model in the presence of the pressure differential.

- HOTCFGM predictions based on the Robinson and power-law creep models were also compared on the basis of a single long cycle consistent with the in-service Space Shuttle Main Engine cycle. In this case, neither the Robinson nor the power-law creep material model predicted appreciable deformation when the creep model parameters most closely describing the experimentally observed inelastic behavior of NARloy-Z were employed. Adjusting the creep parameters for the power-law creep model based analysis in the spirit of an accelerated modeling procedure that preserved efficiency while capturing failure-related deformations, however, did result in appreciable end-of-cycle deformation for the single extended cycle case. Furthermore, these deformations were shown to be comparable with those achieved after multiple short and extended cycles employing the NARloy-Z creep parameters derived from experimental creep data.
- The effect of the cooling channel wall thickness of RLV thrust cell liners was studied relative to bulging and thinning of the cooling channel wall. Thinner cooling channel walls promote bulging and thinning of the cooling channel wall; while thicker cooling channel walls mitigate these detrimental deformations.
- The effects of replacing NARloy-Z with an OFHC copper closeout material in the region behind the cooling channel of the thrust cell liner were isolated and studied. The addition of OFHC copper material was shown to result in greater opening of the cooling channel, as well as accelerated thinning of the cooling channel wall relative to the NARloy-Z thrust cell liner.
- The application of thermal barrier coatings of varying thickness has been investigated as a potential means to mitigate or prevent experimentally observed characteristic deformations of uncoated RLV thrust cell liners. Applying a thermal barrier coating at the inner radius of the thrust cell liner resulted in dramatic changes in temperature fields relative to the uncoated thrust cell liner cases, thereby limiting creep/relaxation within the NARloy-Z structure, particularly in the region of the cooling channel wall. Furthermore, the thickness of the thermal barrier coating was shown to directly influence temperature and deformation fields within the RLV thrust cell liner.
- Functional grading has been employed and analyzed in two forms: homogenized and discrete. Limited-to-no-improvement in RLV thrust cell liner performance was achieved by the application of homogenized grading. Analysis of the actual microstructural details by the discrete approach, however, revealed that the homogenized approach yielded inaccurate results, as locally induced temperature and deformation effects were not accounted for in the homogenized analysis.

6.2 Conclusions

Comparison of the HOTCFGM results generated using the Robinson and power-law creep models has demonstrated that, based on the available material parameters, the power-law creep model more precisely predicts the experimentally observed deformation leading to the "dog-house" failure mode under multiple short-cycle loading, while also providing a significant increase in computational efficiency. Moreover, multiple short-cycle predictions based on the power-law creep model have clearly demonstrated that the pressure differential between the cooling channel and the combustion chamber is a principal factor responsible for cooling channel wall thinning and bulging. Additional comparison of HOTCFGM results based on the Robinson and power-law creep models in the context of a single long cycle has demonstrated that the two material models predict virtually identical deformations. Increasing the power-law creep model coefficients produces appreciable deformations after just one long cycle that would normally be obtained after multiple cycles. This sets the stage for the development of an accelerated modeling procedure to further characterize "dog-house" deformation modes in RLV thrust cell liners.

Thickness of the cooling channel wall has also been shown to be an important factor that influences RLV thrust cell liner deformations, with thicker cooling channel walls more likely to inhibit deformation. This further supports the hypothesis that bulging is caused by the cooling channel/combustion chamber pressure differential.

Analyses of RLV thrust cell liners employing thermal barrier coatings have shown that their influence on temperature and deformation fields was dependent on coating thickness. For the two coating thicknesses considered, however, the 6-mil coating thickness has demonstrated the most desirable temperature and deformation fields. Furthermore, functional grading of metallic substrate and coating materials has not demonstrated improvement in terms of overall thrust cell liner performance, which suggested that for functional grading of the considered constituents the costs of grading likely outweigh the benefits. Additionally, the application of grading is potentially detrimental due to likely roughening of the thrust cell liner wall in the combustion channel as a result of local deformations around relatively coarse inclusions. The homogenized approach to analyzing the graded coatings has also been shown to be incapable of capturing these localized effects, thus producing misleading results.

Finally, this study has demonstrated that the mechanism responsible for deformation leading to "dog-house" failure modes is driven by pressure, creep/relaxation and geometric effects. Since creep and relaxation are strong functions of temperature, it is also concluded that the mechanism is temperature-driven as well, and thus thermal barrier coatings are a potential solution. Previous investigators have also arrived at this conclusion. This work, however, has demonstrated a procedure in which the power-law creep model with adjusted parameters can be used, in the context of a single cycle consistent with the SSME cycle, as a basis for accelerated durability characterization of RLV systems with wide range of coatings and coating systems aimed at mitigating the "dog-house" type failure.

6.3 Future Work

The power-law creep model employed in the present study ignores the influence of primary creep and focuses solely on secondary creep. However, primary or transient creep may potentially play a significant role in short-term creep and relaxation response. As an extension to this study, an investigation of precisely how the primary creep affects short-term creep and relaxation response should be conducted.

The present results also motivate the development of an efficient and accurate accelerated modeling method. Although it was shown that deformations similar to those normally seen after many cycles could be predicted after just one long cycle by adjusting power-law creep parameters, no correlation was made between the two results. Determining whether such a correlation exists should be the goal of future work in this area. The development of an understanding and ability to account for the influence of strain reversals not present in a single long cycle case with modified parameters would be the focus of such work. Identifying such correlation could permit accurate life predictions for proposed RLV thrust cell liners with minimal computational expense.

Acknowledgments

This research was conducted under funding through the NASA Glenn Grant NAG3-2359. The NASA technical monitor for this project was Dr. Steven M. Arnold whose support for the undertaken investigation the authors gratefully acknowledge. The numerical results presented in this report were generated using a computer code developed by Dr. Jacob Aboudi of the Tel-Aviv University in the course of a previous NASA-funded investigation, and subsequently modified by incorporating an implicit integration algorithm and the Robinson unified viscoplasticity model. The authors acknowledge his assistance in resolving some of the numerical convergence problems encountered in this investigation.

References

Aboudi, J. (1991). Mechanics of Composite Materials–A Unified Micromechanical Approach. Elsevier.

Aboudi, J., Pindera, M.-J. and Arnold S. M. (1999). Higher-Order Theory for Functionally Graded Materials, *Composites Part B: Engineering,* Vol. 30B, No. 8, pp. 777-832.

Armstrong, W. H. and Brogren, E. W. (1975). Thrust Chamber Life Prediction Volume II – Plug Nozzle Centerbody and Cylinder Life Analysis, NASA CR 134822.

Armstrong, W. H. and Brogren, E. W. (1976). 3-Dimesional Thrust Chamber Life Prediction, NASA CR 134979.

Armstrong, W. H. (1979). Structural Analysis of Cylindrical Thrust Chambers, NASA CR 159522.

Arnold, S. M., Pindera, M-J., and Wilt, T. E. (1996). Influence of Fiber Architecture on the Inelastic Response of Metal Matrix Composites, *International Journal of Plasticity*, Vol. 12, No. 4, pp.507-545.

Arnold, S. M., Bednarcyk, B. A. and Aboudi, J. (2001). Thermo-Elastic Analysis of Internally Cooled Structures Using a Higher Order Theory, NASA TM 2001-210702.

Arya, V. K. and Arnold, S. M. (1991). Viscoplastic Analysis of an Experimental Cylindrical Thrust Chamber Liner, NASA TM 103287.

Bansal, Y. and Pindera, M-J. (2002). Efficient Reformulation of the Higher-Order Theory for Functionally Graded Materials, NASA CR 2002-211909.

Bednarcyk, B. A. and Arnold, S. M. (2002). MAC/GMC 4.0 User's Manual, NASA TM 2002-212077.

Brandt, R., Pawlowski, L. and Neuer, G. (1986). Specific Heat and Thermal Conductivity of Plasma Sprayed Yttria-Stabilized Zirconia and NiAl, NiCr, NiCrAl, NiCrAlY, NiCoCrAlY coatings, *High Temperatures-High Pressures*, Vol. 18, No. 1, pp 65-77.

Brindley, W. J (1997). Properties of Plasma-Sprayed Bond Coats, *Journal of Thermal Spray Technology*, Vol. 6, No. 1, pp. 85-90.

Brindley, W. J. and Whittenberger, J. D. (1993). Stress Relaxation of Low-Pressure Plasma Sprayed NiCrAlY Alloys, *Materials Science and Engineering A*, Vol. 163, No. 1, pp. 33-41.

Chiang, K. T., Krotz, P. D. and Yuen, J. L. (1995). Blanching Resistant Cu-Cr Coating by Vacuum Plasma Spray, *Surface and Coatings Technology*, Vol. 76-77, Part I, pp. 14-19.

Deevi, S. C. and Sikka, V. K. (1996). Nickel and Iron Aluminides: and Overview on Properties, Processing, and Applications, *Intermetallics*, Vol. 4, No. 5, pp. 357-375.

Ellis, D. L. and Yun. H. M. (1999). Cu-8 Cr-4 Nb Alloy for Reusable Launch Vehicle Combustion Chamber Liners, Insights in R & T Presentation, April 13, 1999.

Ellis, D. L. (2003). Personal Communication.

Esposito, J. J. and Zabora, R. F. (1975). Thrust Chamber Life Prediction Volume I – Mechanical and Physical Properties of High Performance Rocket Nozzle Materials, NASA CR 134806.

Hannum, N. P. and Price Jr., H. G. (1981). Some Effects of Thermal-Cycle-Induced Deformation in Rocket Thrust Chambers, NASA TP 1834.

Haynes, J. A., Ferber, M. K. and Porter, W. D. (2000). Thermal Cycling Behavior of Plasma-Sprayed Thermal Barrier Coatings with Various MCrAlX Bond Coats, *Journal of Thermal Spray Technology*, Vol. 9, No. 1, pp. 38-48.

Illschner, B. and Cherradi, N. (1994). Proceedings of the 3rd International Symposium on Structural and Functional Gradient Materials, *Presses Polytechniques et Universitaires Romandes.*

Jankovsky, R. S., Arya, V. K., Kararoff, J. M. and Halford, G. R. (1995). Structurally Compliant Rocket Engine Combustion Chamber – Experimental and Analytical Validation, *Journal of Spacecraft and Rockets*, Vol. 32, No. 4, pp. 645-652.

Jenkins, W. D. and Digges, T. G. (1951). Creep of Annealed and Cold-Drawn High-Purity Copper, *NBS Journal of Research*, Vol. 47, pp. 272-287.

Lewis, J. R. (1970). Creep Behavior of NARloy-Z, Rockwell International, Rocketdyne Division, Canoga Park, CA, Report MA-SSE-70-902.

Miller, R. A. and Lowell, C. E. (1982). Failure Mechanisms of Thermal Barrier Coatings Exposed to Elevated Temperatures, *Thin Solid Films,* Vol. 95, pp. 265-273.

Miller, R. A. (1997). Thermal Barrier Coatings for Aircraft Engines: History and Directions, *Journal of Thermal Spray Technology*, Vol. 6, No. 1, pp. 35-42.

Morgan, D., Franklin, J., Kobayashi, A. and Nguyentat, T. (1988). Investigation of Copper Alloy Combustion Chamber Degradation by Blanching, *Advanced Earth-to-Orbit Propulsion Technology Conf.*, Vol. 2, p. 506.

Murphy, M., Anderson, R. E., Rousar, D. C. and Van Kleeck, J. A. (1986). Effect of Oxygen/Hydrogen Combustion Chamber Environment on Copper Alloys, *Advanced Earth-to-Orbit Propulsion Technology Conf.*, Vol. 2, p. 580.

Needleman, A. and Suresh, S. (1996). Mechanics and Physics of Layered and Graded Materials, *Journal of the Mechanics and Physics of Solids*, Vol. 44, No. 5, pp. 647-821.

Nesbitt, J. A. and Brindley, W. J. (1989). Heat Transfer to Throat Tubes in a Square-Chambered Rocket Engine at the NASA Lewis Research Center, NASA TM 102336.

Nesbitt, J. A. (1989). Thermal Modeling of Various Thermal Barrier Coatings in a High Flux Rocket Engine, NASA TM 102418.

Paley, M. and Aboudi, J., (1992). Micromechanical Analysis of Composite Structures by the Generalized Method of Cells, *Mechanics and Materials* Vol. 14, No. 2, pp. 127-139.

Pindera, M-J., Arnold, S. M., Aboudi, J. and Hui, D. (1994). Use of Composite Functionally Graded Materials, *Composites Engineering*, Vol. 4, No. 1, pp. 1-145.

Pindera, M-J., Aboudi, J. and Arnold, S. M. (1995). Limitations of the Uncoupled, RVE-Based Micromechanical Approach in the Analysis of Functionally Graded Composites, *Mechanics of Materials*, Vol. 20, No. 1, pp. 77-94.

Pindera, M-J., Aboudi, J., Arnold, S. M. and Jones, W. F. (1995). Use of Composites in Multi-Phased and Functionally Graded Materials, *Composites Engineering*, Vol. 5, No. 7, pp. 743-974.

Pindera, M-J., Aboudi, J., Glaeser, J. and Arnold, S. M. (1997). Use of Composites in Multi-Phased and Functionally Graded Materials, *Composites Part B: Engineering*, Vol. 28B, No. 1/2, pp. 1-175.

Pindera, M-J. and Aboudi, J. (1998). HOTCFGM-1D: A Coupled Higher-Order Theory for Cylindrical Structural Components with Through-Thickness Functionally Graded Microstructures, NASA CR 207927.

Pindera, M-J. and Aboudi, J. (2000). HOTCFGM-2D: A Coupled Higher-Order Theory for Cylindrical Structural Components with Bi-Directionally Graded Microstructures, NASA CR 2000-210350.

Pindera, M-J., Aboudi, J, and Arnold, S. M. (2000). The Effect of Interface Roughness and Oxide Film Thickness on the Inelastic Response of Thermal Barrier Coatings to Thermal Cycling, *Materials Science & Engineering A*, Vol. 28A, No. 4, pp. 158-175.

Pindera, M-J., Aboudi, J, and Arnold, S. M. (2002). Analysis of Spallation Mechanism in Thermal Barrier Coatings with Graded Bond Coats Using the Higher-Order Theory for FGMs, *Engineering Fracture Mechanics*, Vol. 69, No. 14/16, pp 1587-1606.

Quentmeyer, R. J. (1977). Experimental Fatigue Life Investigation of Cylindrical Thrust Chambers, NASA TM X-73665.

Quentmeyer, R. J., Kapser, H. J. and Kazaroff, J. M. (1978). Investigation of the Effect of Ceramic Coatings on Rocket Thrust Chamber Life, NASA TM 78892.

Robinson, D. N. and Swindeman, R. W. (1982). Unified Creep-Plasticity Constitutive Equations for 2 Cr-1Mo Steel at Elevated Temperature, ORNL/TM-8444.

Shiota, I. and Miyamoto, Y. (1996). Proceedings of the 4th International Symposium on Functionally Graded Materials, *Functionally Graded Materials*, Elsevier.

Suresh, S. and Mortensen A. (1998). Fundamentals of Functionally Graded Material, 2nd Edition, Cambridge University Press.

Williams, T. O. and Pindera, M-J. (1994). Multiple Concentric Cylinder Model (MCCM) User's Guide, NASA CR 195299.

Zhong, Y. and Pindera, M-J. (2002). User-friendly and Efficient Reformulation of the Higher-Order Theory for Functionally Graded Materials: Thermal Case, NASA CR 2002-211910.